University of California
Santa Barbara

Koopman spectral analysis and study of mixing in incompressible flows

A dissertation submitted in partial satisfaction
of the requirements for the degree

Doctor of Philosophy
in
Mechanical Engineering

by

Hassan Arbabi

Committee in charge:

Professor Igor Mezić, Chair
Professor Brad Paden
Professor L. Gary Leal
Professor Otger Campas

December 2017

The Dissertation of Hassan Arbabi is approved.

Professor Brad Paden

Professor L. Gary Leal

Professor Otger Campas

Professor Igor Mezić, Committee Chair

December 2017

Koopman spectral analysis and study of mixing in incompressible flows

by

Hassan Arbabi

To Sedigheh, for her infinite patience,

and to Mohammad, for his steady faith.

Acknowledgements

First and foremost, I like to thank my advisor Igor Mezić. He has been a great source of inspiration for my research, and I felt privileged to be working with him and getting his scientific advice during the last four and a half years. He has also given me support and encouragement whenever I needed it, and our frequent discussions on science, books and politics was a big factor in making my PhD experience so enjoyable.

I am grateful to Brad Paden, Otger Camapas and Gary Leal, for agreeing to serve on my doctoral committee, and for giving me comments and suggestions that significantly improved the writing and presentation of this dissertation.

I owe much of my education at UCSB to my lab mates Michael, Ryan, Sophie, Nithin, Milan, Cory, Marko, Alan and Emir. It was a blessing to work with those talented people in the same lab, and I learned immeasurably from them about math, healthy eating habits, and fantasy sport leagues. I wish them luck and hope our paths cross again.

Living in Santa Barbara has left me with a lot of blissful memories. I owe them to my dear friends Momo, Mehran & Fatemeh, Maryam, Zhinus, Payam, Mohammad, Kaveh & Salva, 2xFar, Sina, Shahab and Michael. I cannot express here how much they contributed to my life, I just say that my biggest fear of graduation is that I probably won't be seeing them as much in the future.

Finally, I want to thank my family who have given me their unique brand of love and unwavering support. I am specially grateful to my mom for being so patient with me, and my dad for believing in me even when I doubt myself. I dedicate this thesis to them with love and gratitude.

Curriculum Vitæ

Hassan Arbabi

Education

2017	Ph.D. in Mechanical Engineering, University of California, Santa Barbara.
2012	M.Sc. in Mechanical Engineering, University of Tehran, Iran.
2009	B.Sc. in Mechanical Engineering, University of Tehran, Iran.

Publications

- Arbabi, H., & Mezić, I. (2017). "*Ergodic Theory, Dynamic Mode Decomposition, and Computation of Spectral Properties of the Koopman Operator*" SIAM Journal on Applied Dynamical Systems, 16(4), 2096-2126.
- Arbabi, H., & Mezć, I. (2017). "*Study of dynamics in unsteady flows using Koopman mode decomposition*", to appear in Physical Review Fluids, arXiv preprint:1704.00813.
- Arbabi, H., & Mezić, I. (2017). "*Spectral analysis and mixing in bounded flows* ", in preparation.

Awards

- 3rd Madrid Turbulence Workshop Fellowship, Universidad Politcnica de Madrid, 2017.
- Holbrook Foundation Fellowship, Institute for Energy Efficiency, UC Santa Barbara, 2014-2015.
- Graduate Program Fellowship, University of Tehran, 2009.
- Faculty of Engineering Prize, University of Tehran, 2007.

Abstract

Koopman spectral analysis and study of mixing in incompressible flows

by

Hassan Arbabi

The main theme of this thesis is application of recently developed tools in dynamical systems theory in the study of incompressible fluid flows. These applications fall into two general categories: the first one is study of the flow evolution as an infinite-dimensional dynamical system and it is related to classical topics like flow stability and transition. The second area is the study of flow kinematics where tools of dynamical systems are used to study the trajectory of particles immersed within the flow, and includes topics like mixing enhancement, and prediction of pollution movement in the ocean or atmosphere.

In studying flow dynamics, we utilize the *Koopman operator framework* for data-driven study of dynamical systems (introduced in chapter 1). The increasing popularity of this framework is due to a versatile combination of rigorous theory and data analysis algorithms which allows extraction of dynamic information from almost any type of data from a dynamical system. In chapter 2, we use the spectral properties of the Koopman operator, computed from data, to interpret the flow dynamics: we use the Koopman spectra to determine the attractor geometry, the Koopman eigenfunctions to map the state space linear coordinates, and the Koopman modes to characterize the unsteady motion in the flow domain.

We also discuss the numerical computation of the Koopman spectral properties. As of now, this computation is mostly done through a class of numerical algorithms known as *Dynamic Mode Decomposition (DMD)*. In chapter 3, we prove the convergence of a class of DMD algorithms, called *Hankel-DMD*, for systems with ergodic attractors. Our proofs

are based on the fact that projections in the space of functions can be approximated via vector projections in DMD by the virtue of Birkhoff's ergodic theorem. This new result also provides insight on dynamics of chaotic systems with continuous spectrum and computation of Koopman eigenvalues for dissipative systems. We compare the performance of Hankel-DMD to the signal processing techniques used for fluid flows in chapter 2.

One of the important questions in the study of flow kinematics is how to characterize the mixing in flows with aperiodic time dependence. This question has given rise to a variety of methodologies that strive to describe the mixing in a given aperiodic flow by detecting the coherent structures or other objects of special interest. In chapter 4, we study this problem from a different perspective, namely, we consider how the mixing portrait is changed while the temporal regime of a bounded flow - the lid-driven cavity flow - changes from steady to aperiodic. We use the Koopman spectral properties of the flow (studied in chapter 2) and the so-called *hypergraphs* to isolate and characterize the effect of different elements from the flow dynamics on the mixing. For example, we will see how the interaction between vorticity distribution in the mean flow and non-zero Koopman frequencies determines the regions of slow mixing.

In chapter 5, we report on application of hypergraphs combined with high-frequency radar data in the study of surface mixing in Santa Barbara channel (i.e. the patch of Pacific Ocean between Santa Barbara coastline and Channel Islands) with special focus on prediction of oil slick movements in the aftermath of 2015 Refugio oil spill.

Contents

Chapter 1

Introduction

1.1 Classical theory of dynamical systems

A dynamical system, in the abstract sense, consists of two elements: a set of *states* through which we can describe the evolution of the system in time, and a *rule* for that evolution. Although this viewpoint toward dynamical system is very general and may be applied to almost any system that evolves with time, often the fruitful and conclusive results are achievable when we pose some mathematical structure on the dynamical system, for example, we often assume the set of states form a linear space with nice geometric properties and the rule of evolution has some order of regularity on that space. The prominent examples of such dynamical systems are amply found in physics, where we use differential equations to describe the evolution of physical variables. In this thesis, we specially focus on dynamical systems that can be represented as

$$\dot{x} = f(x), \tag{1.1}$$

where x is the state, contained in the state space $S \subset \mathbb{R}^n$, and $f : S \to \mathbb{R}^n$ is a vector field on the state space. Occasionally, we will specify some regularity conditions for f. We also consider dynamical systems given by the discrete-time map

$$x^{t+1} = T(x^t), \quad t \in \mathbb{Z} \tag{1.2}$$

where x belongs to the state space $S \subset \mathbb{R}^n$, $T : S \to S$ is the dynamic *map* and t is the discrete time index. Just like the continuous-time system in (1.1), we may need to make some extra assumptions on T in the following chapters. The discrete time representation of dynamical system does not often show up in physical systems, but we can use it to represent continuous-time systems, for example, through discrete-time sampling. This representation also has the benefit of being more practical because the data collected from dynamical systems come in the form of discrete time samples.

The study of the dynamical systems in (1.1) and (1.2) was dominated by the geometric viewpoint in much of the last century. In this viewpoint, originally due to Henri Poincaré, the qualitative properties of the solution curves in the state space are studied using geometric tools and the emphasis is put on the subsets of the state space that play a big role in the asymptotic behavior of the trajectories. We briefly describe some concepts of this theory that we will use in the following chapters, but a more comprehensive exposition of these notions can be found in [1, 2].

Assuming that the solution to (1.1) exists, we define the *flow map* $F^t : S \to S$ to be the map that takes the initial state to the state at time $t \in \mathbb{R}$, i.e.,

$$F^t(x_0) = x_0 + \int_{x_0, t'=0}^{t} f(x(t'))dt'. \tag{1.3}$$

The flow map satisfies the semi-group property, i.e., for every $s, t \geq 0$,

$$\begin{aligned} F^t \circ F^s(x_0) &= F^s(x_0) + \int_{F^s(x_0), t'=0}^{t} f(x(t'))dt', \\ &= \int_{x_0, t'=0}^{F^s(x_0), s} f(x(t'))dt' + \int_{F^s(x_0), t'=0}^{t} f(x(t'))dt', \\ &= \int_{x_0, t'=0}^{t+s} f(x(t'))dt', \\ &= F^{t+s}(x_0). \end{aligned} \tag{1.4}$$

where $\circ$ is the composition operator.

Some of the important geometric objects in the state space of continuous-time dynamical systems are as follows:

Fixed point: Any point x in the state space such that $f(x) = 0$ (or $F^t(x) = x$). The fixed points correspond to the equilibria of physical systems. An important notion with regard to fixed points is the stability, that is wether the trajectories starting in some neighborhood of a fixed point stay in its neighborhood over time.

Limit cycle: Limit cycles are (isolated) closed curves in the state space which correspond to the time-periodic solutions of (1.1). The generalized version of limit cycles are tori (cartesian products of circles) which are associated with quasi-periodic motion.

Invariant sets: An invariant set B in the state space satisfies $F^t(B) \subset B$ for all t, i.e., the trajectories starting in B remain in B. The invariant sets are important because we can separate the study of the dynamics on them from the rest of the state space, and they include important objects such as fixed points, limit cycles, attractors and invariant manifolds.

Attractors: An attractor is an attracting set with a dense orbit. An attracting set is an invariant set to which many initial conditions converge. A dense orbit is a trajectory that comes arbitrarily close to any point on the attracting set. For example, union of two

(stable) periodic orbits is an attracting set but not an attractor because the trajectories on one periodic orbit can not come arbitrarily close to the other periodic orbit. Examples of attractors are stable fixed points, stable limit cycles and tori, and also stable chaotic sets like the famous butterfly-shaped set in the chaotic Lorenz system.

Attractors are the objects that determine the asymptotic (that is post-transient or long-term) dynamics of dissipative dynamical systems. In fact, the mere notion of dissipativity (we can think of it as shrinkage in the state space) is enough to guarantee the existence of an attractor in many systems [3]. In some cases, the state space contains more than one attractor, and the attractors divide the state space into different basins; any point in the basin of attraction for attractor A will converge to A.

Bifurcation: Bifurcation analysis is the study of changes in the qualitative behavior of all the trajectories due to the changes in vector field f or the map T. For example, if we add some forcing term to the vector field f a stable fixed point might turn unstable or a limit cycle might appear out of the blue. Another example is the evolution of incompressible flows given by Navier-Stokes equations: increasing the Reynolds number may fundamentally change the flow solution from steady to unsteady, or from periodic to chaotic.

Here is the traditional approach to study a dynamical system: We first discover or construct a model for the system in the form of (1.1) or (1.2). Sometimes, if we are very lucky, we can come up with analytical (or approximation) solutions and use them to analyze the dynamics, by which, we usually mean finding the attractors, invariant manifolds, imminent bifurcations and so on. But most of the times we have to use numerical computations and then extract information by looking at a collection of trajectories in the state space.

This approach has contributed the most to our knowledge of dynamical and physical systems around us, but it is falling short in treating the high-dimensional systems that

lie in the current forefront of science and technology. A set of classic examples, which regularly arises in physics, is the systems that are governed by PDEs. In those cases, the state space is infinite-dimensional and the numerical models that we use may have up to billions of degrees of freedom. Some examples of more recent interest include climate system of the earth, smart cars and buildings, power networks, and biological systems with many interacting components like neural networks. The first problem with the traditional approach is that simulating the evolution of trajectories for these systems is extremely challenging due to the large size of the problem. Moreover, unlike the 2- or 3-dimensional system, the geometric objects in the state space are difficult to realize and verify. The second problem is the uncertainty in the models or even the sheer lack of a model for simulation or analysis. As a result, the field of dynamical analysis, along with many other disciplines, has started shifting toward a less model-based and more data-driven perspective. This shift is not only motivated by the need to overcome the above problems, but it is also fueled by the increasing amount of data produced by today's powerful computational resources and experimental apparatus. In the next section, we introduce the Koopman operator theory, which is a promising framework for integration of data analysis into our mathematical knowledge of dynamical systems.

1.2 A data-driven viewpoint toward dynamical systems through the Koopman operator theory

In the context of dynamical systems, we interpret the data as knowledge of some variable that is related to the state of the system. A natural way to put this into the mathematical form is to assume that data is knowledge of variables which are functions of the state. We call these functions *observables* of the system. Let's consider an exam-

ple. The unforced motion of an incompressible inviscid fluid inside a box constitutes a dynamical system; one way to realize the state space is to think of it as the set of all smooth velocity fields on the flow domain that satisfy the incompressibility condition. The velocity field changes with time according to a rule of evolution which is the Euler equation. Some examples of observables on this system are pressure/vorticity at a given point in the flow domain, velocity at set of points and the total kinetic energy of the flow. In all these examples, the knowledge of the state, i.e., the velocity field, uniquely determines the value of the observable. We see that this definition allows us to think of the data from most of the flow experiments and simulations as values of observables. We also note that there are some type of data that don't fit the above definition as an observable of the system. For example, the position of Lagrangian tracers are not observables of the above system, since they cannot be determined by mere knowledge of the instantaneous velocity field. In this case, we can alter our dynamical system to include that observable as well: we define a second dynamical system to describe the tracer dynamics (the flow domain is the state space, and the rule of evolution is the time-dependent velocity field). The coupling of these two dynamical systems would explain all of the above observables. We observe that choosing the observables on a system requires a careful consideration of the underlying processes that affects those observables.

In light of the above discussion, we can formulate the data-driven analysis of dynamical systems as follows: Given the knowledge of an observable in form of time series generated by experiment or simulation, what can we say about the evolution of the state? The Koopman operator theory provides a mathematical framework for data-driven analysis of dynamical systems by describing the precise relationship between the evolution of observables and the evolution of state.

Consider the continuous-time dynamical system given in (1.2). We define $g : S \to \mathbb{R}$ to be a real-valued observable on this dynamical system. The collection of all such

observables forms a linear vector space. The Koopman operator, denoted by U, is a linear transformation on this vector space, given by

$$Ug(x) = g \circ T(x), \tag{1.5}$$

where $\circ$ denotes the composition operation. The linearity of Koopman operator follows from the linearity of the composition operation, i.e.,

$$U[g_1 + g_2](x) = [g_1 + g_2] \circ T(x) = g_1 \circ T(x) + g_2 \circ T(x) = Ug_1(x) + Ug_2(x). \tag{1.6}$$

For continuous-time dynamical systems, we can define a one-parameter semi-group of Koopman operators, denoted by $\{U^t\}_{t\geq 0}$, where each element of this semi-group is given by

$$U^t g(x) = g \circ F^t(x), \tag{1.7}$$

where $F^t(x)$ is the flow map defined in (1.3). The linearity of U^t follows in the same way as the discrete-time case. The semi-group property of $\{U^t\}_{t\geq 0}$ follows from the semi-group property of the flow map for autonomous dynamical systems given in (1.4),

$$U^t U^s g(x) = U^t g \circ F^s(x) = g \circ F^t \circ F^s(x) = g \circ F^{t+s}(x) = U^{t+s} g(x). \tag{1.8}$$

An schematic representation of the Koopman operator is shown in figure 1.2. We can think of this viewpoint as a *lifting* of the dynamics from the state space to the space of observables. The advantage of this lifting is that it provides a linear rule of evolution - given by Koopman operator - while the disadvantage is that the space of observables is infinite-dimensional. In the next section, we discuss the spectral theory of the Koopman

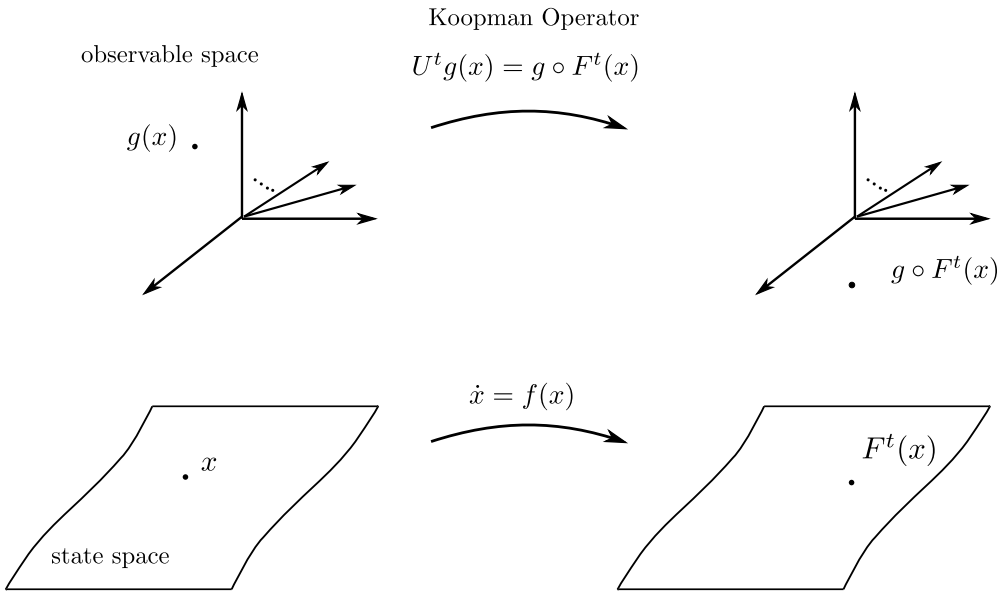

Figure 1.1: Koopman viewpoint lifts the dynamics from state space to the observable space, where the dynamics is linear but infinite dimensional.

operator which leads to linear expansions for data generated by nonlinear dynamical systems. A more detailed account of spectral analysis can be found in chapter 2.

1.3 Koopman linear expansion

A somewhat naive but useful way of thinking about linear operators is to imagine them as infinite-dimensional matrices. Then, just like matrices, it is always useful to look at the their eigenvalues and eigenvectors since they give a better understanding of how a matrix acts on a vector space. Let $\phi_j : \mathbb{R}^n \to \mathbb{C}$ be a complex-valued observable of the dynamical system in (1.1) and λ_j a complex number. We call the couple (ϕ_j, λ_j)

an eigenfunction-eigenvalue pair of the Koopman operator if they satisfy

$$U^t \phi_j = e^{\lambda_j t} \phi_j. \tag{1.9}$$

An interesting property of the Koopman eigenfunctions, that we will use later, is that if (ϕ_i, λ_i) and (ϕ_j, λ_j) are eigenfunction-eigenvalue pairs, so is $(\phi_i \cdot \phi_j, \lambda_i + \lambda_j)$, that is

$$U^t(\phi_i \cdot \phi_j) = (\phi_i \cdot \phi_j) \circ F^t = (\phi_i \circ F^t) \cdot (\phi_j \circ F^t) = U^t \phi_i \cdot U^t \phi_j = e^{(\lambda_i + \lambda_j)t} \phi_i \cdot \phi_j \ . \tag{1.10}$$

Let us assume for now that all the observables of the dynamical system lie in the linear span of Koopman eigenfunctions, that is, for an arbitrary observable like g, we have

$$g(x) = \sum_{k=0}^{\infty} g_k \phi_k(x), \tag{1.11}$$

where g_j's are scalar coefficients. Then we can describe the evolution of g in time as

$$U^t g(x) = \sum_{k=0}^{\infty} g_k e^{\lambda_k t} \phi_k(x), \tag{1.12}$$

which says that the evolution of g has a linear expansion in terms of Koopman eigenfunctions. If we fix the initial state $x = x_0$, we see that the signal generated by measuring g over a trajectory, which is given by $U^t g(x_0) = g \circ F^t(x_0)$ is sum of (infinite number of) sinusoids and exponentials. This might sound a bit odd for nonlinear systems since sinusoids and exponentials are usually generated by linear systems.

It turns out that Koopman linear expansion in (1.12) holds for a large class of nonlinear systems, including the ones that have hyperbolic fixed points, limit cycles and tori. For these systems the spectrum of the Koopman operator consists of only eigenvalues

and their associated eigenfunctions span the space of observables. Now we consider some of these systems in more detail. We borrow these examples from [4] where more details on the regularity of the system and related proofs can be found.

1.3.1 Examples of nonlinear systems with linear Koopman expansion:

1. Limit cycling is a nonlinear property in the sense that there is no linear system ($x = Ax$) that can generate a limit cycle (i.e. isolated periodic orbit). If a limit cycle has time period T, then the signal generated by measuring $g(x)$ while x is moving around the limit cycle is going to be T-periodic. From Fourier analysis, we have

$$g(x(t)) = \sum_{k=0}^{\infty} g_j e^{ik(2\pi/T)t}.$$

   where g_j's are the Fourier coefficients. We can construct the eigenfunctions by letting $\phi_k(x(t)) = e^{ik(2\pi/T)t}$, and eigenvalues by $\lambda_k = ik(2\pi/T)$. It is easy to check that (ϕ_k, λ_k) satisfy (1.9), and the above equation is the Koopman linear expansion of g.

2. Consider a nonlinear system with a hyperbolic fixed point, that is, the linearization around the fixed points yields a matrix whose eigenvalues don't lie on the imaginary axis. There are a few well-known results in dynamical systems theory, such as Hartman-Grobman theorem [2], which state that the nonlinear system is conjugate to a linear system of the same dimension in a neighborhood of the fixed point. To be more precise, they say that there is an invertible coordinate transformation $y = h(x)$ such that the dynamics on y-coordinate is given by $\dot{y} = Ay$ (with the

solution $y(t) = e^{At}y(0)$) and such that

$$F^t(x) = h^{-1}\big(e^{At}h(x)\big)$$

i.e., to solve the nonlinear system, we can lift it to y-coordinate, and solve the linear system, and then transform it back to the x-coordinates. We first show the Koopman linear expansion for linear systems, and then use the conjugacy to derive the expansion for the nonlinear system.

Let $\{v_j\}_{j=1}^n$ and $\{\lambda_j\}_{j=1}^n$ denote the eigenvectors and eigenvalues of A. The Koopman eigenfunctions for the linear system are simply the eigen-coordinates , that is

$$\tilde{\phi}_j(y) =< y, w_j >,$$

where w_j's are normalized eigenvectors of A^*. To see this note that

$$\begin{aligned} U^t\tilde{\phi}_j(y) =< U^t y, w_j >=< e^{At}y, w_j >=< y, e^{A^*t}w_j > \\ =< y, e^{\lambda_j^* t}w_j >= e^{\lambda_j t} < y, w_j >= e^{\lambda_j t}\tilde{\phi}_j(y). \end{aligned}$$

It is easy to show that $\phi_j(x) = \tilde{\phi}_j\big(h(x)\big)$ are eigenfunctions of the Koopman operator for the nonlinear system. Other Koopman eigenfunctions can be easily constructed using the algebraic structure noted in (1.10).

To find the Koopman expansion for the nonlinear system it is easier to further transform y into a decoupled linear system. If the matrix A is diagonalizable and V is the matrix of its eigenvectors, then the state variables of the diagonal system

are, not surprisingly, the Koopman eigenfunctions,

$$\begin{aligned} z = [z_1, z_2, \ldots, z_n]^T = V^{-1}y = [\tilde{\phi}_1(y), \tilde{\phi}_2(y), \ldots, \tilde{\phi}_n(y)]^T \\ = [\phi_1(x), \phi_2(x), \ldots, \phi_n(x)]^T. \end{aligned}$$

Now consider an observable of the nonlinear dynamical system $g(x) = g\big(h^{-1}(y)\big) = g\big(h^{-1}(Vz)\big) = \tilde{g}(z)$ where $\tilde{g}$ is real analytic in z (and therefore y as well). The Taylor expansion for of this observable in variable z reads

$$\begin{aligned} g(x) = \tilde{g}(z) &= \sum_{\{k_1,\ldots,k_n\}\in\mathbb{N}^n} \alpha_{k_1,\ldots,k_n} z_1^{k_1} z_2^{k_2} \ldots z_n^{k_n}, \\ &= \sum_{\{k_1,\ldots,k_n\}\in\mathbb{N}^n} \alpha_{k_1,\ldots,k_n}, \phi_1^{k_1}(x)\phi_2^{k_2}(x)\ldots\phi_n^{k_n}(x), \end{aligned}$$

Using the algebraic property of the Koopman eigenfunctions in (1.10), we can write the Koopman linear expansion of g as

$$U^t g = \sum_{\{k_1,\ldots,k_n\}\in\mathbb{N}^n} \alpha_{k_1,\ldots,k_n} e^{(k_1\lambda_1+k_2\lambda_2+\ldots+k_n\lambda_n)t} \phi_1^{k_1}\phi_2^{k_2}\ldots\phi_n^{k_n}.$$

Recall that the original Hartman-Grobman theorem for nonlinear systems is local [2], in the sense that we knew the conjugacy exists for some neighborhood of the fixed point. But the results in [4] has extended the conjugacy to the whole basin of attraction for stable fixed points using the properties of the Koopman eigenfunctions.

3. Now consider the motion in the basin of attraction of a (stable) limit cycle. The Koopman linear expansion for observables on such system can be constructed by, roughly speaking, combining the above two examples. That is, observables are

decomposed into Koopman eigenfunctions, and each Koopman eigenfunction is a product of a periodic component, corresponding to the limit cycling, and a linearly contracting component for the stable motion toward the limit cycle. The development of this expansion is lengthy and can be found in [4].

The major class of dynamical systems for which the Koopman linear expansion *does not hold* is the class of chaotic dynamical systems. It turns out that for these systems, the eigenfunctions of the Koopman operator do not span the space of observables and we cannot decompose all the fluctuations of the system into exponentials and sinusoids. In such cases the Koopman operator usually possesses a *continuous* spectrum, i.e. a continuum of eigenvalues in the complex plane which are not associated with any finite-dimensional subspace of the observables. (We note that chaos in measure-preserving system is associated by continuous spectrum but continuous spectrum can also be seen in non-chaotic systems. See the cautionary tale in [4]). We will discuss the continuous spectrum further in chapter 2.

Nevertheless, some systems may possess mixed spectra which is a combination of eigenvalues and continuous spectrum. For these systems the evolution of a generic observable is composed of two parts: one part associated with eigenvalues and eigenfunctions which evolves linearly in time and a fully chaotic part corresponding to continuous spectrum. As such, the linear expansion (and the Koopman modes defined below) does hold for part of the data. Example of such a system is given in [5], and we will discuss an example from fluid mechanics in chapter 2.

1.4 Koopman Mode Decomposition (KMD)

A lot of times the data that is measured on a dynamical systems comes to us not from a single observable, but multiple observables. For example, when we are monitoring

a power network system, we may have access to the time series of power generation and consumption on several nodes, or in the study of climate dynamics there are recordings of atmospheric temperature measured at different stations around the globe. We can easily integrate these multiplicity of time-series data into the Koopman operator framework and Koopman linear expansion.

We use $\mathbf{g} : S \to \mathbb{R}^m$ to denote a vector-valued observable, i.e.,

$$\mathbf{g} = \begin{bmatrix} g^1 \\ g^2 \\ \vdots \\ g^m \end{bmatrix}, \quad g^j : S \to \mathbb{R},\ 1 \leq j \leq m.$$

If we apply the linear Koopman expansion (1.12) to each g^j, we can collect all those expansions into a vector-valued linear expansion for $\mathbf{g}$,

$$U^t \mathbf{g}(x) = \sum_{k=0}^{\infty} \mathbf{g}_k e^{\lambda_k t} \phi_k(x). \tag{1.13}$$

The above expansion is the *Koopman Mode Decomposition (KMD)* of observable $\mathbf{g}$ and $\mathbf{g}_k$ is called the *Koopman mode* of observable $\mathbf{g}$ at the eigenvalue λ_k. Koopman modes are in fact the projection of the vector-valued observable $\mathbf{g}$ onto the Koopman eigenfunctions. We can think of $\mathbf{g}_k$ as a structure (or shape) within the data that evolves as $e^{\lambda_k t}$ with time. Let us examine the concept of the Koopman modes in the examples mentioned above. In the context of power networks, we can associate the network instabilities with the Koopman eigenvalues that grow in time, that is $\lambda_k > 0$, and as such, the entries of Koopman mode $\mathbf{g}_k$ give the relative amplitude of each node in unstable growth and hence predict which nodes are most susceptible to breakdown. In the example of climate time series, the Koopman modes of temperature recordings give us the

spatial pattern (depending on the location of stations) of temperature change that is proportional to $e^{\lambda_k t}$, and therefore indicate the spots with extreme variations.

In some physical problems, we have a *field of observables*, i.e., an observable that assigns a physical field to each element of the state space. A prominent example, that we focus on in the next chapter, is a fluid flow. The pressure field over a subdomain of the flow, or the whole vorticity field, are two examples of field of observable defined on a flow, since the knowledge of the flow state (e.g. instantaneous velocity field) unqiuely determines those fields. We can formalize the notion of a field of observable as a function $\mathbf{g} : (S, \Omega) \to \mathbb{R}$ where Ω is the flow domain and $g(x, z)$ determines the value of the field at point z in the flow domain when the flow is at state x. The Koopman linear expansion for $\mathbf{g}$ would be

$$U^t \mathbf{g}(x, z) = \sum_{k=0}^{\infty} \mathbf{g}_k(z) e^{\lambda_k t} \phi_k(x), \tag{1.14}$$

where the Koopman mode $\mathbf{g}_k(z)$ is a fixed field by itself, and similar to the Koopman mode vectors, determines a shape function on Ω which grows with the amplitude $e^{\lambda_k t}$ in time. In a fluid flow, the Koopman modes of vorticity, are steady vorticity fields, and the whole flow can be decomposed into such fields. We will consider this extensively in chapter 2.

1.5 History of Koopman operator theory and its application to data analysis

The Koopman operator formalism originated in the early work of Bernard Koopman in 1931 [6]. He introduced the the linear transformation that we now call the Koopman operator, and realized that this transformation is unitary for Hamiltonian dynamical

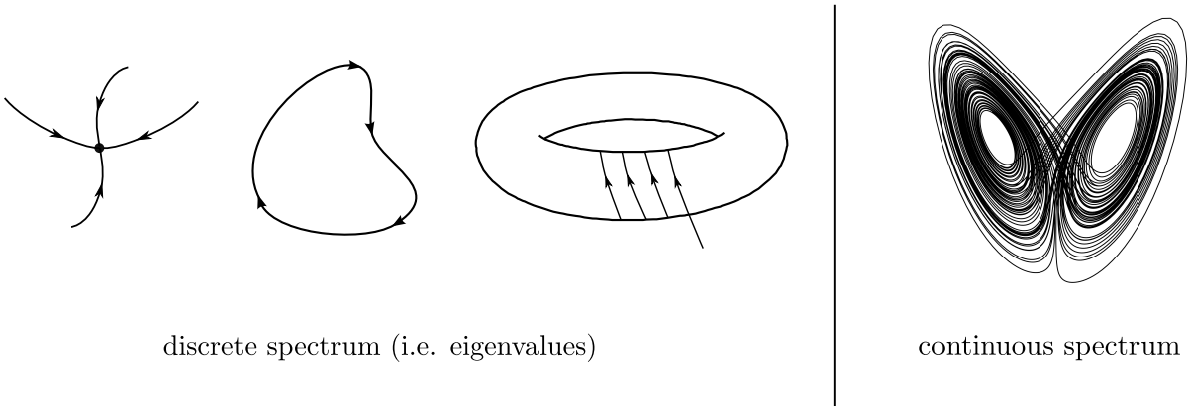

Figure 1.2: Koopman Mode Decomposition fully describes the evolution of observables on systems with Koopman discrete spectrum, but not for chaotic systems which have continuous spectrum.

systems (the "U" notation comes from unitary property). This observation by Koopman inspired John Von Neumann to give the first proof for a precise formulation of ergodic hypotheses, known as *mean ergodic theorem* [7]. In the next year, they wrote a paper together, in which they introduced the notion of the *spectrum of a dynamical system*, i.e. the spectrum of the associated Koopman operator, and noted the connection between chaotic behavior and the continuous part of the Koopman spectrum.

For several decades after the work of Koopman and Von Neumann, the notion of Koopman operator was mostly limited to the study of measure-preserving systems; it can be found as the unitary operator in the proof of the mean ergodic theorem or discussions on the spectrum of measure-preserving dynamical systems [8, 9]. It seldom appeared in other applied fields until it was brought back to the general scene of dynamical system by two articles in 2004 and 2005 [5, 10]. The first paper showed how we can construct important objects like the invariant sets in high-dimensional state spaces from data. The second paper discussed the spectral properties of the Koopman operator further, and introduced the notion of Koopman modes. Both papers also discussed the idea of applying Koopman methodology to capture the regular components of data in systems

with combination of chaotic and regular behavior.

In 2009, the idea of Koopman modes was applied to a complex physical example which is a jet in a cross flow [11]. This work showed the promise of KMD in capturing the dynamically relevant structures in fluid flows and their associated time scales. Unlike other decomposition techniques in flows, KMD combines two advantageous properties: it makes a clear connection between the measurements in the physical domain and the dynamics of state space (unlike proper orthogonal decomposition), and it is completely data-driven (unlike the global mode analysis). The work in [11] also showed that KMD can be computed through a numerical decomposition technique known as *Dynamic Mode Decomposition (DMD)* [12]. Since then, KMD and DMD has become immensely popular in analyzing the nonlinear flows [13, 14, 15, 16, 17, 18, 19, 20, 21]. A review of the Koopman theory in the context of flows can be found in [22], and we will discuss it further in chapter 2.

In the recent years, the extent of KMD applications for data-driven analysis has grown enormously. Some of these applications include model reduction and fault detection in energy systems for buildings [23, 24], coherency identification and stability assessment in power networks [25, 26], extracting spatio-temporal patterns in brain activity [27], background detection and object tracking in videos [28, 29] and design of algorithmic trade strategies in finance [30].

Parallel to the applications, the computation of Koopman spectral properties (modes, eigenfunctions and eigenvalues) has also seen a lot of major advancements. For post-transient systems, the Koopman eigenvalues lie on the unit circle and Fourier analysis techniques can be used to find the Koopman spectrum and modes [5]. We will discuss this line of computation in chapter 2. DMD on the other hand, is the more popular technique for computation of Koopman spectrum from data. In [31] the idea of Extended DMD was introduced for general computation of Koopman spectrum by sampling the state space.

The works in [32] and [33] discussed the linear algebraic properties of the algorithm and suggested new variations for better performance and wider applications. New variants of DMD were also introduced in [34] to unravel multi-time-scale phenomena and in [35] to account for linear input to the dynamical system. Due to constant growth in the size of the available data, new alterations or improvements of DMD are also devised to handle larger data sets [36, 37], different sampling techniques [38, 33, 37] and noise [39, 40]. The convergence of DMD-type algorithms for computation of Koopman spectrum was established in [41] and [42]. We will discuss DMD in chapter 3.

The ultimate goal of many data analysis techniques is to provide information that can be used to predict and manipulate a system to our benefit. Application of the Koopman operator techniques to data-driven prediction and control are just being developed, with a few-year lag behind the above work. This lag is perhaps due to the need to account for the effect of input in the formalism, but promising results have already appeared in this line of research. The work in [43] showed an example of optimal controller which was designed based on a finite-dimensional Koopman linear expansion of nonlinear dynamics. The works in [44, 45] have developed a framework to build state estimators for nonlinear systems based on Koopman expansions. More recent works, have shown successful examples of Koopman linear predictors for nonlinear systems [46], and optimal controllers of Hamiltonian systems designed based on Koopman eigenfunctions [47].

Chapter 2

Study of dynamics in post-transient flows via Koopman operator theory

[1] In this chapter, we discuss the application of Koopman operator theory to study of state space dynamics in *post-transient* flows. By "post-transient", we mean that the trajectory in the state space of the flow has converged to an attractor and there are no transient motions. The major questions to be answered are

1. how can we identify the state space dynamics (for example, type of the attractor) from data using the Koopman operator formalism?

2. and how can we compute the Koopman operator spectrum for such flows?

The traditional approach to determine the dynamic regime of fluid systems is to look at the Fourier or power spectrum of time series . The existence of sharp peaks in those spectra is deemed to indicate periodic motion while broadband spectrum is often interpreted as a sign of chaos [48, 49, 50, 51, 52, 53]. We point out the relationship between

[1] The contents of this chapter are to appear in the journal of Physical Review Fluids.

this classical viewpoint and the Koopman spectral analysis, and describe how the Koopman spectrum of data can be used to determine the geometry of the attractor, using the results in [4]. However, the Koopman viewpoint generalizes the classical spectral analysis by relating the data spectrum to the geometry of the state space through the notion of Koopman eigenfunctions and modes. As a result, one could connect this viewpoint to other state-space analysis and control techniques which are not reachable by Fourier analysis. In particular, Koopman eigenfunctions and eigenvalues provide linearly evolving coordinates in the state space and their knowledge can be used to construct nonparametric predictors [54, 46], state estimators [45, 44] and nonlinear controllers [46, 47] using linear system strategies. The utility of the Koopman eigenfunctions in the context of flow decomposition is further discussed in a recent review in [55]. In this chapter, we present a new way to construct (and visualize) the Koopman eigenfunctions in post-transient flows which are ergodic in the state space.

We apply the Koopman analysis to the two dimensional lid-driven cavity flow with regularized lid velocity. This flow provides a good benchmark for our analysis, since it shows a wide range of dynamic behavior over various Reynolds numbers. The dynamics of each flow regime is discussed in terms of the Koopman spectral properties: the Koopman spectrum determines the type of the attractor, the Koopman eigenfunctions indicate the oscillatory directions of motion in the state space, and the Koopman modes describe the evolution of velocity field in the flow domain. In particular, we use the Koopman modes to study the traveling waves that appear as a result of bifurcation from steady solution to periodic and quasi-periodic flow.

The lid-driven cavity flow becomes fully chaotic at ultimately high Reynolds numbers. In such flows, the Koopman spectrum is continuous and does not contain any (non-trivial) eigenvalues. Using the properties of the Koopman operator and plausible assumptions on the post-transient dynamics, one can show how the measurements of observables on

the chaotic flow can be interpreted as a realization of a *wide-sense stationary stochastic process*. This observation allows us to use the techniques from random signal processing to compute the continuous spectrum of the Koopman operator. We also study the flow regimes with mixed spectra, i.e., flows that have both discrete and continuous spectrum. In those flows, the evolution of flow observables is a mixture of quasi-periodic and chaotic motion, and the Koopman eigenfunctions help us distinguish and extract the quasi-periodic components of motion in the state space.

As of now, DMD-type algorithms (discussed in Chapter 3) are the established tools for computation of Koopman spectral properties. Here, we use a different approch based on methods of classical spectral analysis. For post-transient flows, the spectrum of the Koopman operator (including both continuous and discrete components) lies on the imaginary axis, and the problem of estimating the Koopman spectrum - under certain assumptions - reduces to the classical spectral estimation of signals. This problem is challenging for flows with mixed spectra where there is no a priori model for the continuous spectrum. Our methodology for Koopman spectral estimation consists of three steps: first, we apply a high-resolution algorithm - adapted from Laskar [56, 57]- to detect the candidate discrete Koopman frequencies and modes. The Laskar algorithm provides a controllable balance between accuracy and computational efficiency which makes it suitable for large data sets like high-resolution flow snapshots. Moreover, it makes direct use of the harmonic averaging [10] which has proven convergence properties for computation of Koopman modes. In the second step, we use the ergodic properties of the attractor to discard the spurious frequencies that are artifacts of the continuous spectra. After extracting the periodic components of the flow, we estimate the continuous Koopman spectrum by applying the Welch method [58] to the chaotic residual of the data. Our computational approach is advantageous over DMD-type algorithms since it can handle the continuous spectrum, and it is related to the well-studied techniques and notions in

spectral analysis of signals.

A key objective of modal decomposition techniques is to obtain low-dimensional representation of the data from experiments or numerical simulations. Therefore, an important question regarding any decomposition is how efficiently it can capture the flow evolution. Several authors have already proposed variations of DMD algorithm to obtain low-dimensional description of the the flow features in an optimal manner [32, 59, 60]. DMD is also used in a data assimilation approach to obtain a low-dimensional dynamic model of the cylinder wake flow [61]. Here, we study the efficiency of the Koopman modes by considering the error in the low-dimensional truncations of KMD in representing the cavity flow dynamics. We also compare the performance of Koopman modes with the modes obtained by Proper Orthogonal Decomposition (POD).

The outline of this chapter is as follows. In section 2.1, we review the spectral theory of Koopman operator in more detail and describe how the Koopman spectrum is related to the geometry of the attractor. In section 2.2, we present the Koopman formalism that connects the deterministic evolution of dynamical systems to stochastic processes. This shows us why and how we can use the tools from spectral processing of random signals to compute the Koopman continuous spectrum. The connection between the KMD of different observables such as stream function, velocity field and vorticity are discussed in section 2.3. In section 2.4, we describe the flow settings for the lid-driven cavity flow and the numerical method for solving Navier-Stokes equation. In section 2.5, we discuss the problem of estimating the Koopman spectrum. And finally in section 2.6, we present the results of Koopman spectral analysis for the cavity flow.

2.1 Koopman spectrum and data dynamics

Before we present a formal description of the Koopman spectral expansion, we have to review some mathematical notions and specify the appropriate space of observables to work with: We call a subset of the state space, denoted by A, an attractor of the dynamical system, if for many initial conditions the systems evolves toward A. Moreover A is a minimal set in the sense that it cannot be split into smaller sets with the same attracting property (see chapter 1 or [2]). Simple examples of attractors in the state space of flows include stable fixed points and periodic orbits which correspond to steady and time-periodic flows, respectively. The attractor could be complicated and have chaotic behavior such as the butterfly-shaped attractor of the chaotic Lorenz system. The dynamics on the attractor usually preserves a measure, which we denote by μ. Roughly speaking, this assumption implies that the time-averages (and therefore statistical properties) of observables on the flow are well-defined. Now we let $\mathcal{H} := L^2(A, \mu)$ be the Hilbert space of square-integrable observables defined on the attractor of the flow A with respect to measure μ. In this work, we are interested in observables that belong to $\mathcal{H}$. It turns out that Koopman operator defined in (1.5) is a unitary operator in $\mathcal{H}$ [62], which implies that its spectrum lies on the unit circle. In the following, we use the symbol $\overset{\mu}{=}$ to describe the functional equalities, i.e., the functions on different sides of $\overset{\mu}{=}$ are equal everywhere on A except on a set with zero μ-measure. We also use $< f, g >_{\mathcal{H}}$ to denote the inner products in $\mathcal{H}$.

Let us revisit one key assumption that led to derivation of KMD in chapter 1, namely, the Koopman eigenfunctions spanning the space of observables, in this case, $\mathcal{H}$. For simple attractors like limit cycles and torus, this assumption holds and the expansion in (1.13) can be used to explain the behavior of all observables. For systems with more complicated attractors, the Koopman eigenfunctions might not exist but there is a more

general form of spectral expansion for the Koopman operator, which we will consider shortly.

When the trajectory in the state space of the flow evolves on a limit cycle or a torus, the post-transient flow shows (quasi-)periodic time dependence. Let $\mathbf{\Omega} = [\omega_1, \omega_2, \ldots, \omega_m]^T$ denote the vector of basic frequencies for the motion of state variable on an $m-$dimensional torus (for limit cycles $m = 1$). The Koopman spectral expansion for the flow is given by ([4])

$$U^\tau \mathbf{g} \overset{\mu}{=} \sum_{\mathbf{k}\in\mathbb{Z}^m} \mathbf{g}_\mathbf{k} \phi_\mathbf{k} e^{i\mathbf{k}\cdot\mathbf{\Omega}\tau}. \tag{2.1}$$

We have dropped the dependence of $\mathbf{g}$ and ϕ_k on the state $\mathbf{u}$ to simplify the notation. The above equation is a functional equality which holds almost everywhere on the attractor. However, we can evaluate it for a single trajectory starting from the initial state $\mathbf{u}_0$ to obtain the vector expansion

$$U^\tau \mathbf{g}(\mathbf{u}_0) = \sum_{\mathbf{k}\in\mathbb{Z}^m} \mathbf{g}_\mathbf{k} \phi_\mathbf{k}(\mathbf{u}_0) e^{i\mathbf{k}\cdot\mathbf{\Omega}\tau}. \tag{2.2}$$

The term $U^\tau \mathbf{g}(\mathbf{u}_0)$ is the signal generated by observing $\mathbf{g}$ over the trajectory starting at $\mathbf{u}_0$. If the attractor is a limit cycle, this signal is time-periodic and (2.2) is simply the Fourier series expansion in time. If the attractor is a torus, this expansion is a generalized Fourier expansion for the quasi-periodic signal that is generated by measuring $\mathbf{g}$. We observe that the Koopman frequencies in the above expansion form a *lattice* on the frequency axis. For limit cycling systems, the frequencies are multiples of the basic frequency ω_1, while for the torus attractors, they are linear combinations of the basic frequencies in $\mathbf{\Omega}$ with integer coefficients. Hence, a bifurcation from a limit cycle to a torus can be easily detected by counting the number of basic frequencies in the lattice of Koopman frequencies obtained from the data.

The point-evaluated expansion in (2.2) is more suitable for the study of fluid flows than the function expansion in (2.1). This is due to the fact that each flow simulation or experiment provides us with only a single trajectory in the state space and direct evaluation of the Koopman eigenfunctions on arbitrary regions of state space is not practical. In case of post-transient flows, however, the ergodicity condition - which is discussed later - allows us to construct and visualize the Koopman eigenfunctions on the attractor using the signals coming from as few as one trajectory. We will use this fact to construct and visualize the eigenfunctions in section 2.6.

The converse of the above statements is also true, that is, if the Koopman spectrum of observables has only a countable number of frequencies, then the flow trajectory must be evolving on a torus-shaped attractor in the state space. In fact, the *representation theorem* from the ergodic theory states that if the post-transient flow dynamics is ergodic and smooth, the Koopman operator having only discrete spectrum implies that the motion in the state space is topologically equivalent to rotation on a torus [62]. This classic result combined with numerical KMD algorithm gives a practical framework for detecting motion on tori in high-dimensional systems.

For post-transient flows with chaotic behavior, the Koopman eigenfunctions do not span H and evolution of observables cannot be described based on them. In fact, the Koopman operator spectra, in addition to eigenvalues, includes so-called continuous spectrum which is related to the chaotic component of the flow. The spectral expansion for the Koopman operator takes a more general form (see e.g. [63]), however, as first stated in [10], we can still represent it in a way that distinguishes the quasi-periodic and chaotic components of the evolution. For the scalar observable g, it can be written as

$$U^\tau g \overset{\mu}{=} \sum_{\mathbf{k}\in\mathbb{Z}^m} g_{\mathbf{k}}\phi_{\mathbf{k}} e^{i\mathbf{k}\cdot\mathbf{\Omega}\tau} + \int_{-\infty}^{\infty} e^{i\alpha\tau} dE_\alpha(g). \tag{2.3}$$

The first term on the right-hand-side is the contribution of discrete spectrum and describes the quasi-periodic part of the flow (similar to (2.1)). The second term is the contribution of the continuous spectrum. Informally speaking, $i\alpha$ with $\alpha \in (-\infty, \infty)$, denotes a continuum of eigenvalues distributed along the imaginary axis. The term $dE_\alpha(\cdot)$ is the spectral measure of the Koopman operator, that is, for each interval of frequencies such as $I = [\alpha_1, \alpha_2]$, $\int_{\alpha \in I} dE_\alpha(g)$ is the projection of the observable g onto the eigen-subspace of H associated with I. The above expansion in the functional form is not suitable for flow applications, and it can be converted to a scalar equality by taking its inner product with the same observable g. That is

$$< g, U^\tau g >_H = \sum_{k=1}^{\infty} |g_k|^2 e^{i\omega_k \tau} + \int_{-\infty}^{\infty} e^{i\alpha\tau} \rho_g(\alpha) d\alpha. \tag{2.4}$$

where we have assumed that eigenfunctions are normalized, i.e., $\|\phi_k\|_H = 1$. In passing from (2.3) to (2.4), we have made a technical assumption that the spectral measure of the Koopman operator for the chaotic part is absolutely continuous. The Koopman spectral density ρ_g denotes the contribution of the continuous spectrum, such that the contribution of the frequency interval I to the evolution of g is given by

$$\mu_g(I) = \int_I \rho_g(\alpha) d\alpha. \tag{2.5}$$

In order to compute the spectrum of the Koopman operator from the flow data, we need to assume that *the post-transient dynamics is ergodic*. This implies that the statistics of the flow is independent of the initial condition, and the trajectories starting almost everywhere provide a perfect sampling of observables (in the sense defined in (2.6) below). The ergodicity assumption holds for post-transient evolution of typical dynamical systems, including systems with periodic and quasi-periodic attractors and

many chaotic systems like Lorenz [64]. Under this condition, we can use the pointwise ergodic theorem [8] to approximate the inner product in (2.4) from the data,

$$< g, U^{\tau} g >_H = r_g(\tau) := \lim_{T\to\infty} \frac{1}{T} \int_0^T g(t) g^*(t+\tau) dt. \tag{2.6}$$

where $r_g(\tau)$ is the autocovariance function of g at time τ. Therefore, we can approximate the spectral density of the Koopman operator by first extracting the chaotic component of g, then approximating r_g using finite-time observations (i.e. finite T in (2.6)), and finally applying inverse Fourier transform to r_g. We will discuss the practical aspects of this computation in section 2.5.

2.2 Stochastic processes and Koopman representation of deterministic chaos

In analyzing the chaotic data from experiments and simulations, it is customary to use the tools from applied probability theory even in the case that underlying dynamical systems is fully deterministic. The reasoning behind this approach is the duality between the post-transient evolution of dynamical systems which is measure-preserving and the stationary stochastic processes. A classic formalism of this duality can be found e.g. in [65]. In this section, we reiterate this connection in the framework of the Koopman operator theory with an emphasis on the spectral expansion of observables.

Recall that a continuous-time stochastic process is a collection of real random variables that are indexed by time, and denoted by

$$\{X_t\}_{t\in\mathbb{R}}. \tag{2.7}$$

where X_t is the random variable at time t with a certain distribution over real line. A stochastic process is called *wide-sense stationary* if it satisfies two conditions: its mean does not change with time, i.e.,

$$\mathbb{E}(X_t) = \mathbb{E}(X_{t+\tau}) = m, \quad \text{for all } \tau \in \mathbb{R} \tag{2.8}$$

where $\mathbb{E}(\cdot)$ denotes the expected value over different realizations, and second, its autocovariance function only depends on the lag time, i.e.,

$$cov(X_t, X_{t+\tau}) = \mathbb{E}((X_t - m)(X_{t+\tau} - m)) = cov(\tau). \tag{2.9}$$

Now we consider the deterministic flow evolving on the attractor A which preserves the normalized measure μ ($\mu(A) = 1$). We see that the collection of observables

$$\{U^t g\}_{t\in\mathbb{R}}, \tag{2.10}$$

is a stochastic process defined on the probability space (A, μ). Each observable $U^t g$ is a proper random variable whose probability distribution on the real line is given by

$$\mathbf{P}(B) = \mu\big((U^t g)^{-1}(B)\big), \quad B \subset \mathbb{R}. \tag{2.11}$$

where $\mathbf{P}(B)$ is the probability of the interval B on the real line induced by observable $U^t g$. Because of the measure-preserving property of the dynamics, this probability is independent of t, and the stochastic process in (2.10) is identically distributed (but not independent). Moreover, it is a wide-sense stationary process; in view of (3.15), we can write

$$\mathbb{E}(U^t g) =< U^t g, 1 >_{\mathcal{H}} =< g, U^{-t} 1 >_{\mathcal{H}} =< g, 1 >_{\mathcal{H}} = \mathbb{E}(g), \tag{2.12}$$

and

$$\begin{aligned} cov(U^t g, U^{t+\tau} g) &= < U^t g, U^{t+\tau} g >_{\mathcal{H}}, \\ &= < U^{-t} U^t g, U^\tau g >_{\mathcal{H}}, \\ &= < g, U^\tau g >_{\mathcal{H}} = cov(\tau). \end{aligned}$$

where we have used the unitary property of the Koopman operator $(U^t)^* = U^{-t}$. Using the measure-preserving property, one can go further and show (2.10) is also strictly stationary [65], but that is not required for the spectral expansion.

According to the Wiener-Khintchine theorem (e.g. [66]), the covariance of any wide-sense stationary process, such as (2.10), has a spectral expansion in the following form,

$$cov(g, U^\tau g) = \int_{-\infty}^{\infty} e^{i\alpha\tau} dF(\alpha)$$

where F is the power spectral distribution of the process. Note that this expansion holds for the general post-transient dynamics including both chaotic and quasi-periodic behavior. In the case that there are no quasi-periodic components in the flow, and F is absolutely continuous similar to (2.4), we can rewrite the above expansion as

$$cov(g, U^\tau g) = \int_{-\infty}^{\infty} e^{i\alpha\tau} \rho(\alpha) d\alpha$$

where ρ is called the Power Spectral Density (PSD) of the stochastic process. Despite the deterministic nature of our system, we observe that we can treat the chaotic component of the data as a a realization of a stationary process, and consequently, the notion of the Koopman spectral density coincides with that of PSD for random signals. This observation is specially helpful in computation, since it enables us to use the spectral

estimation techniques of stochastic signals to find the Koopman spectrum.

2.3 Choice of observables and the relationship between their Koopman modes

In this section, we consider the choice of observables for KMD and the relation between their modal decomposition. This question is important since applying KMD to an observable reveals only the Koopman eigenvalues that are present in the expansion of that observable. Furthermore, one can use the relationship between the Koopman modes of different observables to reduce the computational cost of the analysis. Here, we provide two propositions that describe this relationship.

Proposition 1

Let $g, h : \Omega \times M \to \mathbb{R}$ be two fields of observables defined on the flow domain Ω and the state space of the flow M. Assume $g(., z),\ h(., z) \in \mathcal{F}(\Omega)$ for every state $z \in M$ where $\mathcal{F}(\Omega)$ denotes a normed space of fields on Ω. Moreover, the observables are related through a linear operator $\mathcal{D} : \mathcal{F}(\Omega) \to \mathcal{F}(\Omega)$, such that $\mathcal{D}g = h$ and $\mathcal{D}$ is bounded in $\mathcal{F}$. Let g_i and h_i denote the Koopman modes of observable g and h, respectively, associated with the Koopman eigenvalue λ_j. Then those modes are related to each other via $\mathcal{D}g_i = h_i$. In words, the Koopman mode decomposition commutes with the linear bounded operator $\mathcal{D}$.

Proof: Let us assume for now that the dynamical system is measure-preserving which implies $\lambda_j = i\omega_j,\ \omega_j \in \mathbb{R}$. The Koopman modes are computed via the harmonic

averaging [10] and it follows that

$$\begin{aligned} h_j &= \lim_{T\to\infty} \frac{1}{T}\int_0^T h(t)e^{-i\omega_j t}dt \\ &= \lim_{T\to\infty} \frac{1}{T}\int_0^T \mathcal{D}g(t)e^{-i\omega_j t}dt \\ &= \lim_{T\to\infty} \frac{1}{T}\mathcal{D}\int_0^T g(t)e^{-i\omega_j t}dt \\ &= \mathcal{D}\lim_{T\to\infty} \frac{1}{T}\int_0^T g(t)e^{-i\omega_j t}dt \\ &= \mathcal{D}\ g_j \end{aligned} \tag{2.13}$$

We have used the linearity and continuity (i.e. boundedness) of $\mathcal{D}$ in the 3rd and 4th equalities, respectively. If the system is dissipative, the Koopman modes are given by Generalized Laplace Analysis formula [22]. The above argument could be used, along with induction, to prove the statement for that case. ■

In application to fluids, we are mostly interested in linear operators that involve spatial derivatives, such as gradient or curl. The derivative operator, however, is not bounded and therefore needs a special treatment which is given by the following proposition.

Proposition 2

Let $g, h : \Omega \times M \to \mathbb{R}$ be two fields of observables defined on the flow domain Ω and the state space of the flow denoted by M. Assume the observables are bounded over their domain and related to each other through

$$\mathcal{D}g = h, \tag{2.14}$$

where D denotes the partial derivative with respect to a spatial coordinate in Ω. Let g_k and h_k denote the Koopman modes of observables associated with the Koopman frequencies

$\omega_k,\ k = 1, 2, \ldots.$ *Then*

$$\mathcal{D} g_k = h_k. \tag{2.15}$$

for every $x \in \Omega$. *In words, the Koopman mode decomposition commutes with the spatial differentiation in the flow domain.*

Proof: Define the finite-time harmonic average of g at the frequency ω_k by

$$g_k^T(x) = \frac{1}{T} \int_0^T g(x,t) e^{-i\omega_k t} dt. \tag{2.16}$$

The Koopman mode of g associated with ω_k is then given by

$$g_k = \lim_{T\to\infty} g_k^T. \tag{2.17}$$

The Leibniz rule implies that the spatial derivative commutes with the finite-time averaging in (2.16), i.e.,

$$h_k^T = \mathcal{D} g_k^T. \tag{2.18}$$

for any finite T. Fix x. If both $h(x)$ and $g(x)$ are integrable functions, then the existence of $g_k(x)$ implies the existence of $h_k(x)$ [67], and since the scalar functions $h_k^T(x)$ and $\mathcal{D} g_k^T(x)$ are equal up to any finite T, their limits as $T \to \infty$ must be equal, i.e., $h_k(x) = \mathcal{D} g_k(x)$. ■

For example, consider the field of stream function ψ and the velocity field $\mathbf{u}$ in an incompressible 2D flow. These two observables are related thorough the linear operator $\nabla^\perp := [\partial/\partial y, -\partial/\partial x]^T$, that is, $\mathbf{u} = \nabla^\perp \psi$. Let ψ_j and $\mathbf{u}_j$ denote the Koopman modes of these two observable fields associated with Koopman eigenvalue λ_j, then

$$\mathbf{u}_j = \nabla^\perp \psi_j, \quad j = 1, 2, 3, \ldots. \tag{2.19}$$

A similar relationship could be established between the Koopman modes of the vorticity field, denoted by $\boldsymbol{\zeta}_j$, and those of the velocity field,

$$\boldsymbol{\zeta}_j = \nabla \times \mathbf{u}_j, \quad j = 1, 2, 3, \ldots. \tag{2.20}$$

This further implies that applying KMD to either of the these observable fields yields the same Koopman eigenvalues as long as none of the modes lie in the null space of the linear operator.

The knowledge of any of the above observable fields, i.e., stream function, velocity field or vorticity, uniquely determines the state of the system and therefore it can be used to elicit the Koopman spectrum of all other observables of interest. Thus, we conclude that applying KMD to any of these fields would give us the information which is sufficient to detect the flow bifurcations. In the dynamical analysis of the cavity flow, we choose the stream function as the primary observable for the application of KMD since its Koopman modes and eigenvalues are least expensive to compute. The Koopman modes of velocity and vorticity can be computed using (2.19) and (2.20).

2.4 The lid-driven cavity flow

The 2D lid-driven cavity flow is a simple model of a fluid confined to a rectangular box with a moving lid that induces a circulating flow inside the box. This flow requires a relatively simple computational setup, and it is commonly used as a benchmark for computational schemes (see e.g. [68]). It is is also realized in experiments on 2D fluid phenomena using soap films [69]. The lid-driven cavity flow represents a simplified model of geophysical flows driven by shear [70, 71], and some common types of mixers in polymer engineering [72]. This flow is particularly interesting for dynamical analysis since it shows

a wide range of behaviors by increasing the velocity of the top lid [73, 74, 75, 76, 52, 77].

Our computational model of the flow consists of a square domain $[-1, 1]^2$, with solid stationary boundaries, except the top lid (at $y = 1$) which moves with a regularized velocity profile,

$$u_{lid} = (1 - x^2)^2, \quad x \in [-1, 1]. \tag{2.21}$$

This boundary condition has a low-order polynomial form which satisfies the continuity and incompressibility in the top corners (as opposed to the uniform velocity profile), and it is frequently used in numerical studies on cavity flow [73, 78, 77].

The incompressibility of the flow allows us to use the stream function formulation of the Navier-Stokes equation,

$$\frac{\partial}{\partial t}\nabla^2\psi + \frac{\partial\psi}{\partial y}\frac{\partial}{\partial x}\nabla^2\psi - \frac{\partial\psi}{\partial x}\frac{\partial}{\partial y}\nabla^2\psi = \frac{1}{Re}\nabla^4\psi, \tag{2.22}$$

subject to two types of boundary condition on the stream function,

$$\psi\Big|_{\partial\Omega} = 0 \quad and \quad \frac{\partial\psi}{\partial n}\Big|_{\partial\Omega} = u_w, \tag{2.23}$$

where the wall velocity u_w is zero everywhere except at the top wall, where $u_w(y = 1) = u_{lid}$. The solution of the cavity flow as described above is known to exist and be unique, and moreover, the flow trajectory asymptotically converges onto a universal attractor in the state space [79].

For numerical solution, we have used the Chebyshev-spectral collocation method described in Ref. [80]. The stream function is approximated by a polynomial of order N in

spatial directions. This polynomial is determined by its values at the Chebyshev points,

$$(x_i, y_j) = \left(\cos(\frac{i\pi}{N}), \cos(\frac{j\pi}{M})\right) \tag{2.24}$$
$$i = 0, 1, \ldots, N, \quad j = 0, 1, \ldots, M.$$

Given the polynomial approximation and the prescribed boundary condition in (2.23), we use the transformed variable $q(x, y)$ defined by

$$\psi(x, y) = (1 - x^2)(1 - y^2)q(x, y). \tag{2.25}$$

which satisfies the Dirichlet boundary condition identically, and turns the Neumann boundary condition into Dirichlet boundary condition, i.e.,

$$q(\pm 1, y) = q(x, -1) = 0, \tag{2.26}$$
$$q(x, +1) = -\frac{1}{2}u_{top}(x). \tag{2.27}$$

For the temporal discretization of the ordinary differential equations on $q(x_i, y_i)$, we have used the second-order Crank-Nicholson scheme for the diffusion terms and second-order Adams-Bashforth discretization for the convection terms. The flow solutions studied in this work are computed using zero initial velocity. The numerical solutions of the steady flow obtained by our method agree with the results reported in [73]. There is also agreement on the time periods of the periodic flows between the two studies. To the best of our knowledge, however, there are no reported benchmark solutions for quasi-periodic or aperiodic flow.

2.5 Numerical computation of Koopman spectrum and modes using techniques from signal processing

As discussed in section section 2.1, the Koopman spectrum of post-transient flows lies on the imaginary axis, and its estimation reduces to the classical spectral analysis of flow signals. In this work, we are specially interested in flows that possess a continuous spectrum in addition to discrete frequencies. Reliable estimation of each of these two components from data has a rich history in the context of signal processing and is still a subject of ongoing research. The Discrete Fourier Transform (DFT) algorithm, by itself, gives a good approximation for the location of the discrete frequencies and there are a large number of the so-called *high- or super-resolution* algorithms, based on DFT or otherwise, that improve the accuracy of such estimation. For continuous spectra, however, the DFT is a poor estimator. Application of DFT to the autocovariance function in (2.6) produces an estimate of spectral density with high fluctuations that *do not* diminish with the increase of data samples [81]. Therefore, the algorithms developed to resolve continuous spectrum use some type of local averaging over frequency domain to reduce this variance. Conversely, this averaging process reduces the frequency resolution and makes these algorithms ill-suited for detection of discrete spectra [82].

Our strategy for computing the Koopman spectrum is to first detect and extract the discrete frequencies using a high-resolution algorithm, and then apply a continuous spectra estimator to the remainder. Note that estimation of mixed spectrum (i.e. including both continuous and discrete) from finite-data is an ill-posed inverse problem, and most of the developed methods for accurate estimation of mixed spectrum are parametric, in the sense that they are based on specific models for the continuous spectrum such

as colored or auto-regressive noise [82, 83, 84], which are not valid for typical chaotic dynamical systems. Our methodology here is non-parametric, and the only assumption that we make on the continuous spectrum is that it is absolutely continuous (section 2.1). Instead, we connect our analysis to the theory of dynamical systems through the ergodicity assumption. Namely, given the ergodicity of motion on the attractor, we use the fact that the Koopman modes are unique (i.e. depend only on the observable and the flow parameters) which allows us to identify and discard the spurious discrete frequencies that are not robust with respect to the choice of initial condition or the time interval of integration.

The succession of ideas in this section are as follows: first, we describe the idea of harmonic averaging from classical ergodic theory which has proven convergence properties for computation of Koopman modes given the knowledge of Koopman frequencies. Then, we discuss the Laskar algorithm for computation of the discrete spectrum and benchmark its numerical performance against other high-resolution algorithms. In the last subsection, we discuss our procedure for approximation of Koopman continuous spectrum from the chaotic component of the data, and test its performance for two well-known chaotic dynamical systems.

2.5.1 Harmonic averaging and DFT

For post-transient flows, the Koopman eigenfunctions are orthogonal [10] and the Koopman modes can be computed via direct projection of the observables onto the Koopman eigenfunctions. Let ϕ_j be the normalized Koopman eigenfunctions ($\|\phi_j\| = 1$) associated with the frequency ω_j. We observe that the Koopman eigenfunction evolves as $\phi^\tau(\mathbf{u}_0) = e^{i\omega\tau}$ over a single trajectory of the system. Using the pointwsie ergodic

theorem, we can compute the Koopman modes using the *harmonic average*,

$$\mathbf{g}_j := < \mathbf{g}, \phi_j >_H = \lim_{T\to\infty} \frac{1}{T} \int_0^T \mathbf{g}(\tau) e^{-i\omega_j \tau} d\tau. \tag{2.28}$$

The above limit is known to exist for almost every initial condition under the assumption that the dynamics on the attractor is preserving a measure [67] - which is less restrictive than ergodicity. The time series obtained by experiments and simulations consists of time-discrete samples over finite intervals. Assuming uniform sampling at time instants $\{\tau_0 = 0, \tau_1, \ldots, \tau_{N-1} = T\}$, we can approximate the harmonic average as

$$\mathbf{g}_j^N = \frac{1}{N} \sum_{k=0}^{N-1} \mathbf{g}(k) e^{-i\omega_j \tau_k}, \tag{2.29}$$

where $\mathbf{g}(k)$ is the value of observable at the sampling time τ_k. For any ω_j that is a Koopman frequency, we have $\mathbf{g}_j^N \to \mathbf{g}_j$ as $N \to \infty$, and otherwise $\mathbf{g}_j^N \to 0$. For periodic and quasi-periodic attractors, the rate of convergence is proportional to N [85], but for typical chaotic systems it scales with $\sqrt{N}$ [86].

Given a uniform sampling in time, we can use DFT frequencies as a rough approximation of the Koopman frequencies. Let the number of samples N be even, and denote the sampling interval by $\Delta\tau := T/(N-1)$. The DFT grid of frequencies is

$$\Omega_j = \frac{2\pi j}{N\Delta\tau}, \quad j = -\frac{N}{2}, -\frac{N}{2}+1, \ldots, 0, \ldots, \frac{N}{2}-1, \tag{2.30}$$

Accordingly, computing the harmonic average in (2.29) reduces to computing the DFT amplitude of the observations,

$$\hat{\mathbf{g}}_j = \frac{1}{N} \sum_{k=0}^{N-1} \mathbf{g}(k) e^{-i\Omega_j k\Delta\tau}. \tag{2.31}$$

DFT is already shown to be equivalent to DMD when applied to a linearly independent sequence of snapshots with zero mean [32]. The advantage of using DFT to find the Koopman modes lies in its relative simplicity and the availability of Fast Fourier Transform (FFT) algorithms for its implementation. On the other hand, it suffers from two basic shortcomings. The first one is the *picket fencing*, i.e., the Koopman frequencies depend on the dynamics and may occupy arbitrary locations on the real interval, whereas the DFT frequencies are determined by the sampling rate and observation interval. The second phenomenon, known as *spectral leakage*, refers to the spillage of energy from a frequency to its neighborhood, and it is due to the finite length of observation interval which leads to errors in approximation of the modes [87, 81]. In the following, we discuss some of the methods developed to overcome these problems.

2.5.2 Estimation of Koopman frequencies

The problem of detecting discrete frequencies from noisy signals is often called *line spectral estimation*. The general goal of the methods for line spectral estimation is to eliminate the shortcomings of DFT and compute estimates of frequencies with errors that are smaller than the DFT frequency resolution. Many of such methods use DFT as a preliminary step because of its computational efficiency, and often utilize a combination of windowing and interpolation to reduce the leakage and fencing problem (see e.g. [88, 89, 90]). Some other techniques, including Prony analysis [91] and Nonlinear Last-Squares (NLS) method [81], treat the line spectral estimation as a data fitting problem to find the frequencies and associated amplitudes that represent the time series with least error. These methods do not face the the DFT shortcomings, but they are more costly for computation and suffer vulnerability to noise (e.g. Prony analysis) or the choice of initial guess for the optimal values of fitting (e.g. NLS) [81]. We note that using Prony analysis

to compute the Koopman modes is explored in [92].

There are also the so-called *subspace* techniques which exploit the linear algebraic properties of matrices that embed the signal information. The two most popular algorithm in this class are the MUSIC [93] and ESPRIT [94] which use eigen-decomposition of the data covariance matrix. These methods circumvent the obstacles of the DFT-based methods by posing the frequency estimation as an eigenvalue problem, which leads to accurate estimates at a higher computational complexity due to the embedding of time-series in large matrices. Moreover, these methods are parametric and their good performance is only guaranteed when the noise follows a pre-determined model (which is usually white noise) [81]. A more recent class of super-resolution algorithms recast the line spectral estimation as a convex optimization of measures on the frequency domain [95, 96]. Under the two conditions of spectral sparsity and minimum separation between the frequencies, this framework recovers the exact values of frequencies from a finite number of time samples. Unfortunately, this framework has a high computational complexity and it is only suitable for discrete spectrum identification in presence of little noise.

In this work, we adapt the algorithm suggested by Laskar [56, 57] to compute the discrete Koopman frequencies and the associated modes. This algorithm is attractive for two reasons: first, it makes explicit use of harmonic averaging which allows us to assess its convergence based on the theory. In fact, this algorithm was invented to detect chaotic motion from data in Hamiltonian systems with a moderate number of degrees of freedom, like the solar system (see [56]). Secondly, this algorithm is related to a popular sparse approximation technique known as Orthogonal Matching Pursuit (OMP)[97]. OMP efficiently approximates a sparse vector (i.e. vector with few non-zero elements) given a relatively small number of linear measurements on the sparse vector through an iterative greedy algorithm. Different variants of this algorithm are

frequently used in decomposition of signals and images into sinusoids, wavelets etc. (see e.g. [98, 99, 100, 101]).

The main idea in Laskar algorithm is to discretize the frequency domain and use OMP (implemented as FFT and harmonic averaging) to find the frequencies and associated amplitudes that best explain the time-sampled values of the observables (which are the linear measurements in the sense of OMP). The algorithm also uses windowing and adaptive refinement of the initial grid to diminish the effect of spectral leakage and picket fencing. The computational steps are outlined in algorithm 1, and below we describe the structure of data matrix used as the input.

Let $\{\mathbf{g}(0), \mathbf{g}(1), \ldots, \mathbf{g}(N-1)\}$ be the set of observations on the vector-valued observable $\mathbf{g}$, made on uniformly-spaced time instants $\{\tau_0 = 0, \tau_1, \ldots, \tau_{N-1} = T\}$. The snapshot data matrix G is defined as

$$G = [\mathbf{g}(0)|\mathbf{g}(1)|\ldots|\mathbf{g}(N-1)]. \tag{2.32}$$

Also let $\|\cdot\|$ denote an appropriate vector norm on $\mathbf{g}(\cdot)$, and σ denote the expected $\|\cdot\|$-norm of measurement or computation noise in the data. We denote by $S(\omega)$ the sinusoid associated with frequency ω, that is

$$S(\omega) = [1,\ e^{i\omega\tau_1},\ e^{i\omega\tau_2}, \ldots, e^{i\omega\tau_{N-1}}]^T. \tag{2.33}$$

We also make use of windowing functions in the general form of a weight vector:

$$W = [w_0,\ w_1,\ w_2, \ldots, w_{N-1}]^T. \tag{2.34}$$

Algorithm 1 (Adapted) Laskar algorithm for estimation of Koopman frequencies

Require: Snapshot matrix $G_{M\times N}$.

Ensure: Set of Koopman frequencies $\Omega = \{\omega_1, \ldots, \omega_m\}$ and matrix of Koopman modes $V = [\mathbf{g}_1, \ldots, \mathbf{g}_m]$.

1: Let $R = G$ and initialize the dictionaries $D = [\,]$ and $\Omega = \{\,\}$.

2: Apply row-wise FFT to R. Pick the DFT frequency $\hat{\omega} := \omega_j$ which yields the complex amplitude $\mathbf{g}_j$ with highest $\|\cdot\|$-norm and satisfying $\|\mathbf{g}_j\| > \sigma$. If there is no such frequency proceed to step 8.

3: Compute the windowed harmonic average

$$V_\omega = S^*(\omega) diag(W) R^T \tag{2.35}$$

over a refined grid of frequencies centered around $\hat{\omega}$. Pick the frequency ω_k that yields V_{ω_k} with the highest $\|\cdot\|$-norm.

4: Add ω_k and its sinusoid to the dictionary:

$$\Omega \leftarrow \Omega \cup \{\omega_k\}, \tag{2.36}$$

$$D \leftarrow [D\ S(\omega_k)]. \tag{2.37}$$

5: Solve the least-square problem

$$W = \arg\min_{\hat{W}} \|G^T - D\hat{W}\|_{fro}. \tag{2.38}$$

6: Compute the new remainder R by subtracting the contribution of the frequencies in the dictionary

$$R = G^T - DW. \tag{2.39}$$

7: Go to step 2.

8: Return Ω and $V = W^T$.

Choice of data matrix G and appropriate norm: We have applied the above algorithm to the vector of the stream function (ψ) values at the computational grid points given in (2.25). The Koopman modes of velocity and vorticity are subsequently computed using (2.19) and (2.20). The results reported in this paper are computed using the sampling rate $\omega_s = 10\ sec^{-1}$, where sec is the unit of the the characteristic time given by

$$1\ sec := \frac{L_R}{U_R} \tag{2.40}$$

and L_R and U_R are the half of the cavity side length and maximum velocity on the top lid, respectively. Our numerical experiments show that the computed frequencies are independent of the sampling frequency $\omega_s \in [10, 200]$. We have chosen the vector-norm in the above algorithm such that it reflects the kinetic-energy norm of the Koopman modes, that is,

$$\|\mathbf{u}_j\| := \|\mathbf{u}_j\|_{KE} = \left(\frac{\int_\Omega |\nabla^\perp \psi_j|^2 ds}{U_R^2} \right)^{1/2}. \tag{2.41}$$

with U_R denoting the maximum velocity on the top lid. We choose $\sigma^2 = 10^{-6}\|\mathbf{u}_0\|^2$. This is a heuristic choice and reflects how strong a periodic component we want to resolve. Other factors that might be considered are the accuracy of the numerical simulation and the computational cost.

Dictionary of frequencies for real-valued data and choice of the window function: Given that the spectrum is symmetric for real-valued data, we can effectively reduce the computational cost by doing the search and refinement (step 1 and 2) for a non-zero frequency ω_k and then add the pair $(-\omega_k, \omega_k)$ to the dictionary in step 3. To evaluate the filtered harmonic average in step 2, we use the Hann window given by

$$w(k) = \frac{1}{2} + \frac{1}{2}\cos(\pi k/N). \tag{2.42}$$

Using the window function is not necessary but improves the detection of frequencies that are close to each other - in the case of quasi-periodic flow - as it reduces the local spectral leakage. Alternative window functions can be chosen based on the proximity and relative strength of the frequencies (see e.g. [81]).

Least-square projection and harmonic average: The least-square problem in step 4 is equivalent to orthogonal projection of observables onto the Koopman eigenfunctions. In fact, in the limit of $N \to \infty$, the computation of Koopman modes in step 4 reduces to the harmonic average in (2.28). To see this, note that the solution to (2.38) is given by $W = D^{\dagger}G^{T}$, however as $N \to \infty$, the columns of D become orthogonal and $D^{\dagger} \to (1/N)D^{*}$. It is easy to check that $(1/N)D^{*}G^{T}$ yields the harmonic average of columns of G^{T}, i.e., the Koopman modes.

Computational complexity: Given $G_{M\times N}$, the implementation of FFT in step 1 requires $O(MN \log N)$ operations. An efficient implementation of step 2 in a form of matrix multiplication requires $O(MNd)$ operations with d being the size of the refined grid. The complexity of the least square problem using direct methods is $O(K^2N + KNM)$ where K is the number of frequencies. Since the algorithm runs K iterations, the total complexity is $O(K^2NM + K^3N + KMNd)$. For a typical application to flow snapshots (i.e. $M, N \gg K$), the complexity will be $O(KMNd)$.

Benchmark: We compare the performance of Laskar algorithm to two other high-resolution algorithms. The first one is the Newtonized Orthogonal Matching Pursuit (NOMP) [101]. The benchmark study in [101] suggests that NOMP is a near-optimal algorithm in the sense that its accuracy is close to the theoretical limit. This algorithm is similar to Laskar, but one of its distinctive features is the refinement of *all* frequency estimates after the detection of each new frequency. The computational run-time of NOMP is approximately $O(K^2)$ longer than Laskar, where K is the number of detected frequencies. We also implement the MUSIC algorithm using the `rootmusic()` function

in MATLAB. This algorithm estimates the frequencies based on the eigen-decomposition of the data covariance matrix and has a high computational complexity which does not allow its implementation on large number of observables. In case of large data sets where these two algorithms cannot be applied to the all data, we implement them in the compact form, i.e., we choose the sampling of the stream function at 10 random points, and apply MUSIC/NOMP to compute the Koopman frequencies and then compute the Koopman modes using an orthogonal projection onto the dictionary of sinusoids.

Spectral estimation by MUSIC and NOMP do not suffer from the fencing problem since they don't use the discretization of the frequency domain, and therefore provide accurate estimates of Koopman frequencies for (purely) periodic and quasi-periodic flows. The accuracy of Laskar algorithm, on the other hand, depends on the choice of adaptive frequency grid, and higher resolutions requires evaluating (2.35) over finer grids. However, comparison (in FIG. 2.1) shows that Laskar algorithm is better suited for computing the Koopman frequencies and modes in case of large flow data with mixed spectrum. The reason for this is two-fold: Many super-resolution algorithms are based on a special model for the noise spectrum (e.g., the MUSIC algorithm relies on the white noise model), which does not hold for the continuous spectrum of dynamical systems. (In the context of detecting discrete frequencies, we treat the continuous spectrum as noise.) The second reason is related to the computational cost of the algorithm. The super-resolution algorithms that are not based on FFT are computationally expensive, and can only be applied in the compact form, (i.e. applying to one or few observables simultaneously). In such cases, they may fail to capture many of low-energy frequencies in the presence of noise, as in the case of mixed spectra shown in FIG. 2.1. (We have verified those frequencies by the criteria introduced in the next section and the fact that they lie on the lattice of frequencies described in (2.1)). In contrast, the computational parsimony of the Laskar algorithm allows estimation of the frequencies using a larger set

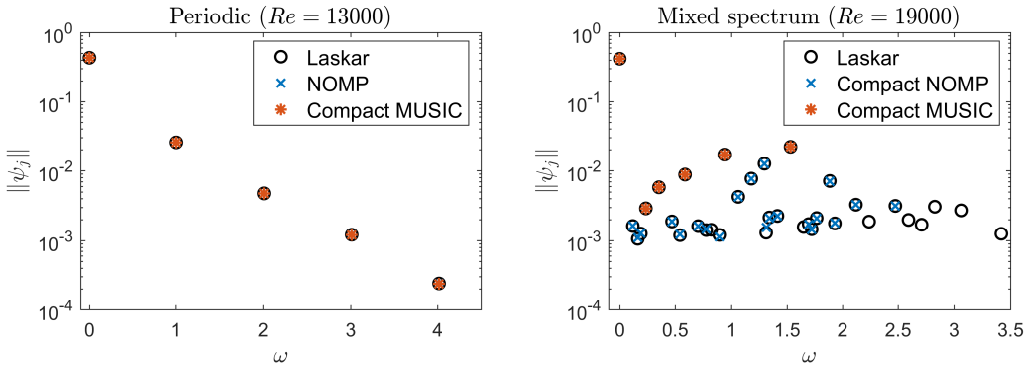

Figure 2.1: Comparison of Laskar Algorithm with MUSIC [93] and NOMP[101]. In the right panel, the continuous spectrum and frequencies with $\|\mathbf{u}_j\| < 10^{-3}$ are omitted to avoid clutter.

of (and possibly all) the observables. This, in turn, increases the effective signal-to-noise ratio for the low-energy periodic components which leads to detection of their associated frequencies.

2.5.3 Detection of the spurious frequencies in flows with mixed spectra

In the case of mixed spectra, application of high-resolution methods to the data might produce peaks that are not genuine Koopman frequencies, but artifacts of the continuous spectrum. In such flows, we need a criteria to distinguish such peaks from the actual frequencies. On the other hand, the assumption of the ergodicity implies that the Koopman modes are unique (i.e. don't depend on the initial condition), and therefore Koopman modes computed over different (and sufficiently long) intervals should be the same. To use this notion we run Laskar'a algorithm on different (overlapping or non-overlapping) chunks of the snapshot matrix. We discard the frequencies whose associated modes show too much variability depending on the time interval of computation. In the results to be presented, we have discarded the modes that show more than %5 variability in the kinetic energy norm, while the modes are computed over intervals of 1000 *sec* and

longer.

2.5.4 Estimation of Koopman continuous spectrum

Recall from **S**2.2, that the spectral density of the Koopman operator appearing in (2.4) coincides with the PSD of the chaotic component of signals generated by measuring observables. If g is a real-valued observable with purely continuous spectrum, then we can approximate the autocovariance function in (2.6) using the time series data

$$r(\pm\tau) = \frac{1}{N}\sum_{k=0}^{N-1} g(k)g(k+\tau), \quad 0 \leq \tau \leq N-1, \tag{2.43}$$

and compute the *correlogram* approximation of PSD as

$$\rho_g(\alpha) = \sum_{\tau=-(N-1)}^{N-1} r(\tau)e^{-i\alpha\tau}, \quad \alpha \in [0, 2\pi). \tag{2.44}$$

Such a direct evaluation produces a highly fluctuating estimate of ρ_g, and the computation must be modified to get a more reliable estimate [102].

We use the Welch method [58] to approximate the continuous part of the Koopman spectrum. The idea behind this algorithm is simple: it approximates the spectral density of the signal over small (and possibly overlapping) subsamples of the data using FFT, and averages the computed densities over all those subsamples. The averaging process reduces the variance of PSD estimation by a factor that is equal to the number of subsamples [58]. This reduction in the variance comes at the price of low spectral resolution (which increases with the length of subsamples), and using too many subsamples may result in over-averaging and getting a flat spectrum. Therefore, the number and length of windows should be chosen carefully to maintain an accurate estimate while resolving the distribution of energy over frequencies.

The Welch method reduces to the Bartlett method [103] in case of non-overlapping subsamples. Bartlett was among the first to realize that different subsamples of the data can be averaged to find a better estimate of the spectral density given that the autocovariance decays rapidly enough and the subsamples are sufficiently large. This methodology can be interpreted as special case in the well-known class of Balckman-Tukey estimators [104] and the general class of filter bank approaches. We refer the reader to [81] for a discussion of connections between these methods.

We apply the Welch method, outlined in algorithm 2, to the chaotic component of the velocity field. This component is computed by extracting the contribution of Koopman modes from the original data matrix. To measure the contribution of the continuous spectrum to the whole flow field, we compute the kinetic energy density of the continuous spectrum given by

$$p(\omega) := \frac{1}{U_R^2} \int_\Omega \rho_{\mathbf{u}}(\omega) ds. \tag{2.45}$$

This definition would allows us to compute the kinetic energy content of each frequency interval via integrating $p(\omega)$ over that interval, i.e.,

$$P(I) := \frac{1}{2\pi} \int_I p(\omega) d\omega. \tag{2.46}$$

and we will recover the average kinetic energy of chaotic fluctuations by calculating $P([0, 2\pi))$.

Algorithm 2 Welch method for estimation of Koopman continuous spectrum

Require: Snapshot matrix $G_{M\times N}$, length of subsamples L and overlapping length K.

Ensure: Matrix of spectral densities $R_{M\times L}$.

1: Let $S = \text{FLOOR}[(M-L)/K] - 1$ be the number of subsamples.

2: **for** the i-th row of G denoted by r **do**

3: Divide r into S subsamples given by

$$r_j(m) = r((j-1)K + m),\ m = 1, 2, \ldots, L, \quad j = 1, 2, \ldots, S.$$

4: **for** each subsample r_j **do**

5: Use FFT to compute the PSD of r_j (2.44) and denote it by $\phi_j(\omega_k)$ where ω_k with $k =, 1, \ldots, L$ are the L-point FFT frequencies.

6: **end for**

7: Let

$$R_{ik} = \frac{1}{S}\sum_{j=1}^{S} \phi_j(\omega_k)$$

8: **end for**

9: Return R and $\Omega = \{\omega_0, \omega_1, \ldots, \omega_L\}$.

We test the Welch algorithm using two well-known chaotic dynamical systems. The first one is a discrete-time map on a periodic 2D domain, known as Arnold's cat map, and given by

$$\begin{aligned} x(t+1) &= 2x(t) + y(t) \mod 1, \\ y(t+1) &= x(t) + y(t) \mod 1. \end{aligned}$$

For the choice of observables

$$\begin{aligned} g_1(x,y) &= e^{2\pi i(2x+y)} + \frac{1}{2}e^{2\pi i(5x+3y)}, \\ g_2(x,y) &= g_1(x,y) + \frac{1}{4}e^{2\pi i(13x+8y)}. \end{aligned}$$

the Koopman spectral density is known in analytical form [105],

$$\begin{aligned} \rho(g_1;\theta) &= \frac{1}{2\pi}\left(\frac{5}{4} + \cos\theta\right), \\ \rho(g_2;\theta) &= \frac{1}{2\pi}\left(\frac{21}{16} + \frac{5}{4}\cos\theta + \frac{1}{2}\cos 2\theta\right). \end{aligned}$$

where $\theta \in [0, 2\pi)$ is the discrete-time frequency.

The second system that we consider is the chaotic Lorenz system:

$$\begin{aligned} \dot{x} &= 10(y-x), \\ \dot{y} &= x(28-z) - y, \\ \dot{z} &= xy - \frac{8}{3}z. \end{aligned}$$

This system is known to have only continuous spectrum (except the zero frequency) [64], but no analytical expression exists for the spectral density of non-trivial observables. We compare the Welch estimation of the Lorenz spectrum with the recent results in [106] which is based on the approximation of Fourier moments of the spectral measure and the Christoffel-Darboux kernel. In particular, we consider the observable

$$g_3(x,y,z) = x.$$

and compute its spectral density $\rho(g_3;\omega)$ where $\omega \in [0, \omega_s/2)$ is the continuous time

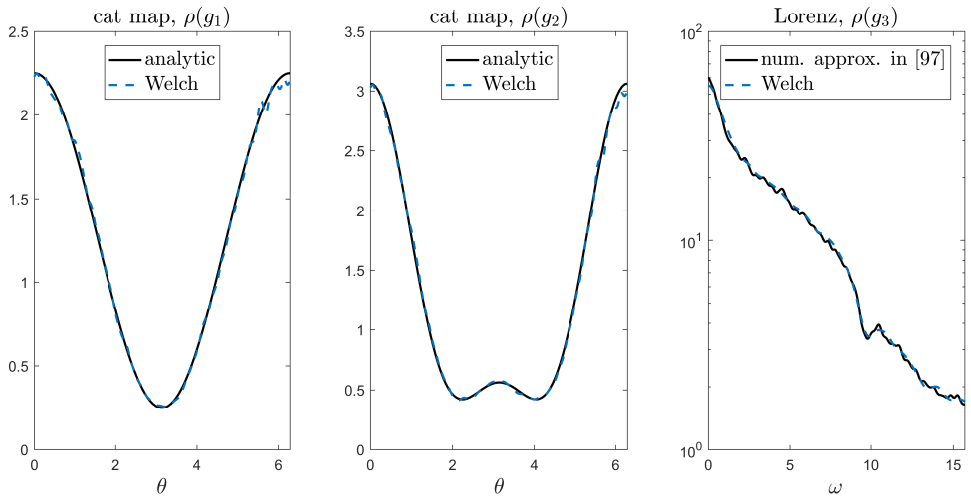

Figure 2.2: Validation of Welch method for computing Koopman spectral density in Arnold's cat map (the left two panels) and chaotic Lorenz system. The densities for cat map are known in analytic form [105], and the numerical benchmark results for Lorenz system are from [106].

frequency and sampling frequency ω_s is 10π. The comparison in FIG. 2.2 shows great agreement between the results of Welch method, analytic densities of the cat map and the numerical results of [106] on Lorenz system.

2.6 Cavity flow dynamics and KMD

2.6.1 Koopman spectrum

Figure 2.3 shows the distribution of kinetic energy in the discrete and continuous spectrum of the Koopman operator. The energy contained in Koopman modes (black bars in the figure) is simply the kinetic energy contained in each mode, but the representation of energy over the continuous spectrum is slightly different: the amount of energy contained at each frequency interval is the integral of the kinetic energy density of continuous spectrum (defined in (2.45) and shown as the blue curve) over that interval.

The evolution of the Koopman spectrum in FIG. 2.3 indicates the sequence of the

bifurcations as follows: for $Re \leq 10000$, the cavity flow induced by regularized lid velocity converges to a steady laminar solution which corresponds to a fixed point in the state space of the flow. The Koopman mode expansion for steady flow is trivial (hence not shown) and consists of zero frequency with an associated mode which is the steady flow. At a Reynolds number slightly above 10000, the steady solution becomes unstable and the numerical solution converges to a time-periodic flow which maintains stability up to $Re = 15000$. The kinetic energy in this range is fully distributed in the Koopman modes. The basic frequency of periodic flow decreases with the Reynolds number, until at $Re \geq 15000$, another bifurcation occurs and the solution converges to a quasi-periodic flow. The basic frequencies of the quasi-periodic flow also decrease with the Re, but around $Re = 18000$ another bifurcation occurs and the level of kinetic energy lying in continuous spectrum quickly rises to a few percent. This kinetic energy of continuous spectra keeps rising such that at $Re \geq 22000$ we cannot detect any robust Koopman modes which indicates there are no quasi-periodic components in the state space dynamics.

The discrete Koopman frequencies obtained for periodic, quasi-periodic, and interestingly, the mixed-spectra flow match the lattice structure of the frequencies in the KMD of quasi-periodic flow (2.1). That is, every frequency is accurately described by the integer combination of one or two basic frequencies (table 2.1). From the representation theorem mentioned in section 2.1, we recall that this means the attractor is shaped like a limit cycle or a torus in the state space. For the flow with the mixed spectra, however, no such theorem exists but we can speculate that it consists of both a quasi-periodic factor and a chaotic factor. This type of attractor is called *skew-periodic* in the literature of dynamical systems theory [107].

The evolution of the Koopman spectrum in FIG. 2.3 offers a picture of transition to chaos that is consistent with the theory of Ruelle and Takens [108]. According to this theory, the chaotic state of the flow can be reached after one or two Hopf bifurcations

Re=13000 (periodic)		Re=16000 (quasi-periodic)		Re=19000 (mixed spectra)	
St	k	St	**k**	St	**k**
0.000000	0	0.000000	(0,0)	0.000000	(0,0)
0.159826	1	0.155375	(1,0)	0.243822	(1,1)
0.319653	2	0.252287	(1,1)	0.150046	(1,0)
0.479479	3	0.096911	(0,1)	0.206310	(2,-1)
0.639303	4	0.193823	(0,2)	0.093778	(0,1)
0.799130	5	0.310751	(2,0)	0.300089	(2,0)
0.958954	6	0.213839	(2,-1)	0.187556	(0,2)
		0.349197	(1,2)	0.056266	(1,-1)
		0.407661	(2,1)	0.450133	(8,-8)
		0.058463	(1,-1)	0.393868	(7,-7)
		0.116927	(2,-2)	0.337602	(6,-6)
		0.135359	(-1,3)	0.225068	(4,-4)
		0.446109	(1,3)	0.487643	(2,2)
		0.290733	(0,3)	0.018756	(2,-3)
		0.038447	(-1,2)	0.431379	(6,-5)
		0.504573	(2,2)	0.543910	(8,-7)
		0.020017	(2,-3)	0.375111	(0,4)
		0.232270	(-1,4)	0.468886	(0,5)
		0.466125	(3,0)	0.693955	(9,-7)
		0.272303	(3,-2)	0.581423	(2,3)

Table 2.1: Koopman frequencies with highest kinetic energy in the lid-driven cavity flow. The basic frequency vector is $St = 0.159826$ for the flow at Re=13000, $St = [0.15538, 0.09691]$ for Re=16000 and $St = [0.15005, 0.09378]$ for $Re = 19000$. The rest of the frequencies can be described (to the sixth digit of accuracy) as a linear combination of the basic frequencies. The coefficients of the combination are given by **k** in the table.

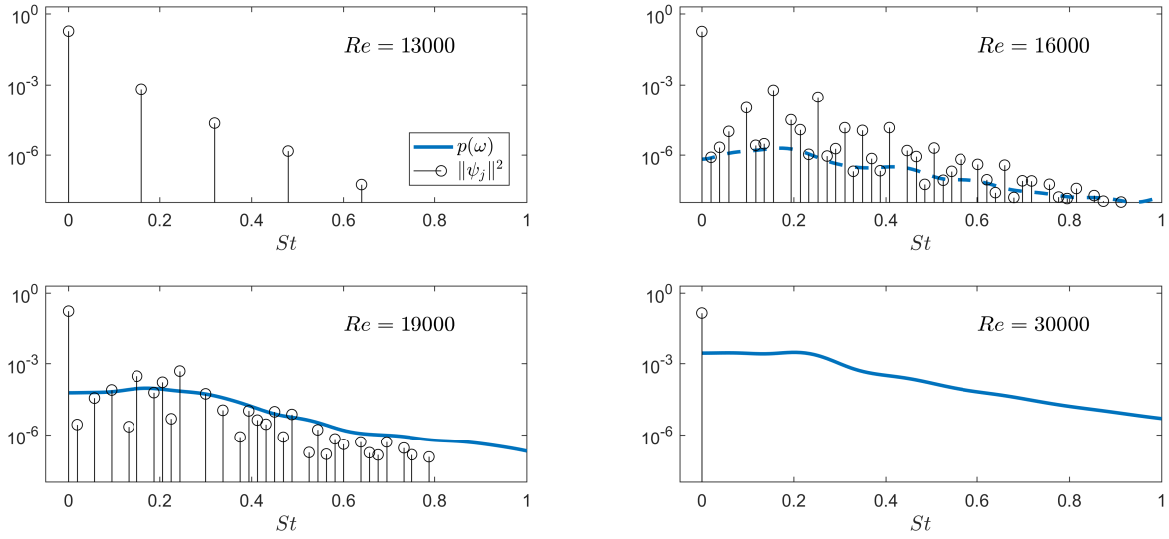

Figure 2.3: Distribution of energy in the discrete (black bar) and continuous (blue curve) spectrum of the Koopman operator for cavity flow. The evolution of spectrum indicates the transition from periodic to chaotic flow. The ratio of average chaotic fluctuation energy to total kinetic energy of unsteady motion is 1.5×10^{-3}, 0.11 and 1.00 for $Re = 16000, 19000$ and 30000, respectively.

from an initially stable steady flow. Physical evidence for this theory appeared in the experiments on rotating Couette flow and natural convection by Swinney and Gollub [48]. In particular, they detected the flow bifurcations using the power spectrum of velocity measurements at a single point in the flow domain. The transition to chaos was marked by the sudden growth of "background noise" in the power spectrum of the quasi-periodic flow. The above results show that the Koopman spectrum can be used as a generalized spectral tool for study of bifurcations; it offers a clear quantification of the energy in terms of true periodicity and contribution of continuous spectra for deterministic flows, and furthermore it connects the discrete spectrum to the state space geometry and flow domain.

2.6.2 Koopman eigenfunctions

In this section, we discuss the relationship between the Koopman spectrum and the state space dynamics. This relationship is realized through the notion of Koopman eigenfunctions, which are associated with the Koopman eigenvalues. For post-transient flows, the eigenfunctions provide an intrinsic coordinate on the state space along which the time evolution is linear oscillation. First, we construct the Koopman eigenfunctions for the quasi-periodic cavity flow using the theory presented in [4, 5], and then we discuss its application to the flow with mixed spectra. Note that for flows with ultimately high Reynolds (e.g. $Re = 30000$), the only Koopman frequency is zero and there are no oscillatory Koopman eigenfunctions and modes.

Consider the quasi-periodic flow at $Re = 16000$. This flow possesses a torus-shaped attractor and the state space trajectory evolves on this torus with two basic frequencies ω_1 and ω_2 (whose non-dimensional values are given in table 2.1. We can parameterize the torus using two *time-linear coordinates*, that is $(\theta, \gamma) \in [0, 2\pi)^2$ with the linear evolution equation

$$\begin{aligned} \dot{\theta} &= \omega_1, \\ \dot{\gamma} &= \omega_2. \end{aligned}$$

The evolution of the trajectories on the actual torus in the state space is nonlinear, but the tuple (θ, γ) are angular coordinates along a torus with uniform flow which is dynamically equivalent to the actual torus in the state space [4]. On this time-linear coordinates the Koopman eigenfunctions are the same as the Fourier functions, i.e., the Koopman eigenfunction $\phi_{k,l}$ associated with frequency $\omega_{k,l} = k\omega_1 + l\omega_2$ is

$$\phi_{k,l}(\theta, \gamma) = e^{ik\theta + il\gamma}. \tag{2.47}$$

Although there is no analytical formula for transformation from the actual attractor to the time-linear coordinates defined above, we can construct the eigenfunctions in the state space using information on a trajectory, given that the trajectory is ergodic and sufficiently long. We can normalize an the eigenfunctions such that $\phi^{t=0}(\mathbf{u}) = 1$, and hence the value of the eigenfunction along the trajectory is given by setting $\theta = \omega_1 t$ and $\gamma = \omega_2 t$ in (2.47).

Figure 2.4 shows the construction of the eigenfunctions in the state space of the flow. The state space is realized by delay embedding of some typical observables [109] - in this case the stream function at random points in the flow domain. The attractor of the periodic flow is a limit cycle (top row in the figure) and the Koopman eigenfunctions (shown as color field) correspond to the one dimensional linear time coordinate ($\theta \in [0, 2\pi)$). For the quasi-periodic flow, the attractor is a 2-torus and the Koopman eigenfunctions show the directions on the torus where the evolution is linear and periodic, e.g., the eigenfunction $\phi_{0,1}$, shown in the rightmost panel of the second row shows the coordinate γ along which the trajectories oscillate with frequency ω_2.

For skew-periodic attractors (i.e. flow with mixed spectra) the eigenfunctions are even more interesting because they provide coordinates on an attractor which is not exactly a torus, but possesses directions with periodic motion. The embedded attractor of the flow at $Re = 19000$, for example, is similar to a torus which is related to the fact that this flow possesses a strong discrete spectrum (in the energy sense) with two basic frequencies and a relatively weak continuous spectrum. In fact, using the Koopman eigenfunctions, we can compute the *factors* (i.e. geometric slice) of such an attractor, on which, the motion is purely quasi-periodic. The existence of such factorization for systems with discrete Koopman eigenvalues was shown in [5]. Here, we use this idea to reconstruct the quasi-periodic component of the attractor at $Re = 19000$. Let E be the observable whose embedding is used to construct the attractor. According to the (2.3), this observable can

be split to two components:

$$E = E_{qp} + E_c, \tag{2.48}$$

where E_{qp} denotes the component of E that lies in the span of Koopman eigenfunctions (including the eigenfunction at zero frequency), and E_c is the chaotic component that belongs to subspace associated with the continuous spectrum. By doing KMD on E, we can extract its Koopman modes and reconstruct the evolution quasi-periodic component E_{qp} over the trajectory which is given by the first two terms in (2.3). The embedding of E_{qp} constructs the torus which corresponds to the quasi-periodic part of the motion. As such, the general motion on the skew-periodic attractor (third row of the figure) can be decomposed into rotational motion along its quasi-periodic component (bottom row) superposed with chaotic motion in an unknown direction. We stress that the above constructions are valid for any type of state space realization as long as the data from an ergodic trajectory is available.

2.6.3 Koopman modes

The Koopman modes of the vorticity field associated with the basic frequencies of each flow are shown in FIG. 2.5. Each mode can be interpreted as the component of the vorticity field along the eigenfunction coordinates in the state space (the color field in FIG. 2.4). For the eigenfunction at zero frequency, this component is the mean flow (Koopman mode associated with zero frequency) and does not change in time. The oscillatory modes however are components of the vorticity field that linearly oscillate along the eigenfunction directions.

The major share of kinetic energy in all the unsteady regimes is contained within the mean flow. This mode is essentially composed of the central vortex in the flow and the corner eddies in the left corners. For fully chaotic flows, the mean flow is the only

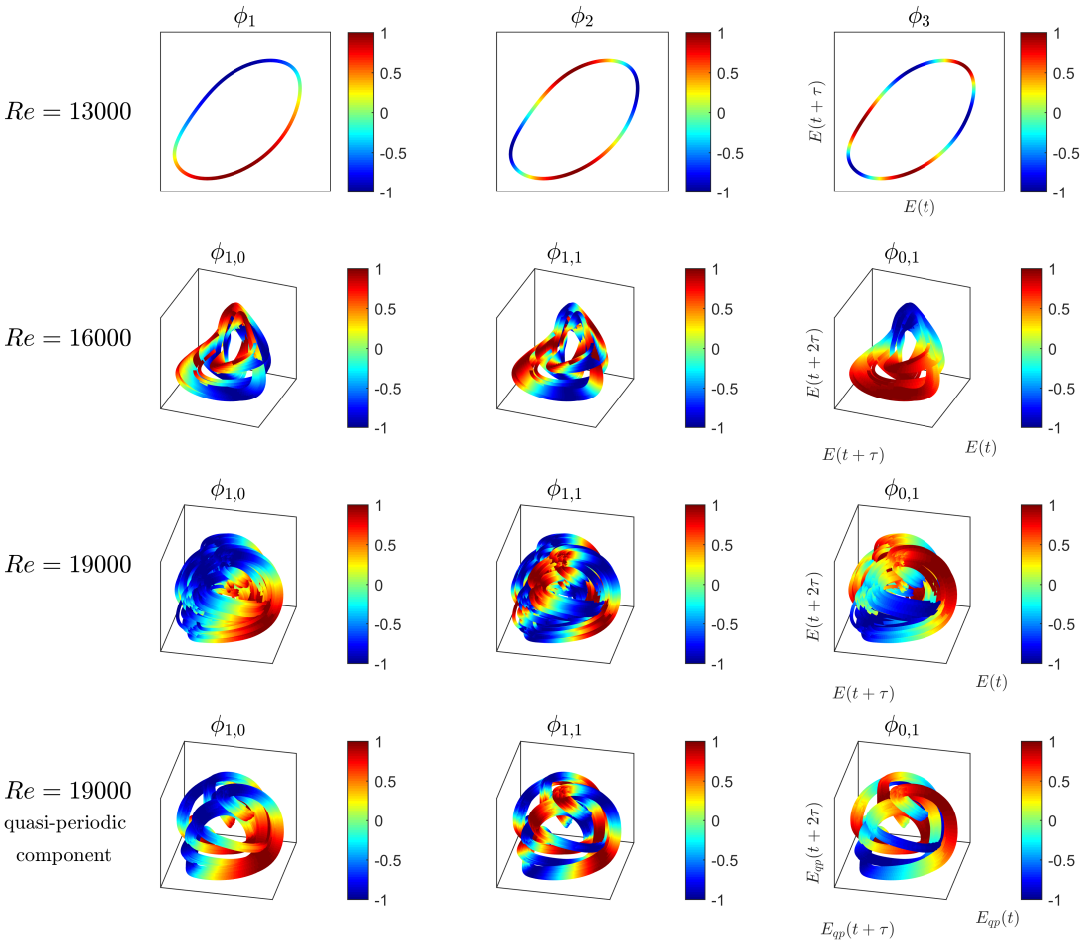

Figure 2.4: The (real part of) Koopman eigenfunctions shown as color field on the periodic, quasi-periodic and skew-periodic attractors (row 1-3). The last row is the quasi-periodic component of the skew-periodic attractor extracted using Koopman eigenfunctions. The attractors are reconstructed using delay embedding of stream function values at random points in the flow domain (E) with the time delay of 1.0 *sec* for the periodic flow, and 2.4 *sec* for the rest.

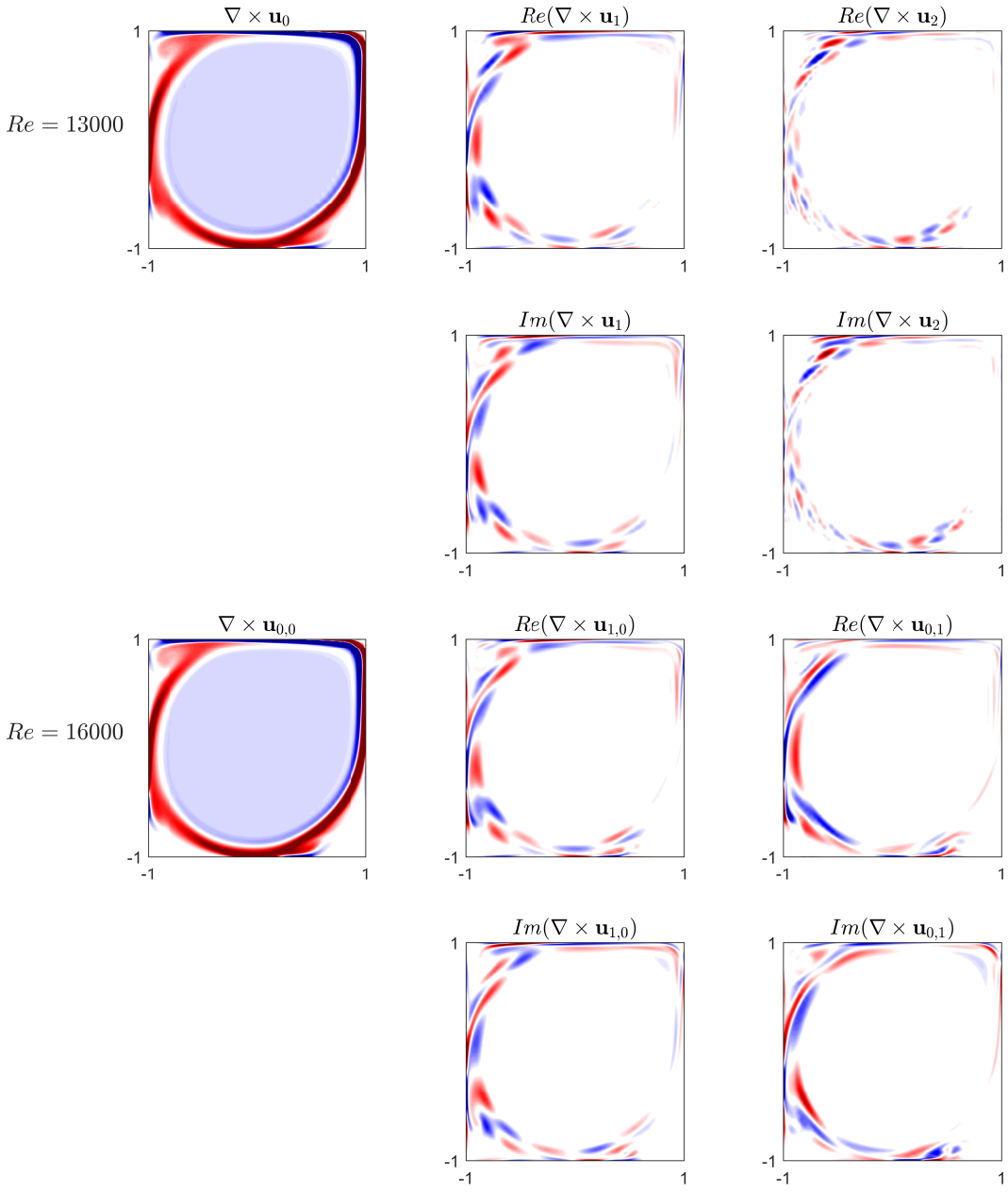

Figure 2.5: The Koopman modes of vorticity in cavity flow (see the caption in next page).

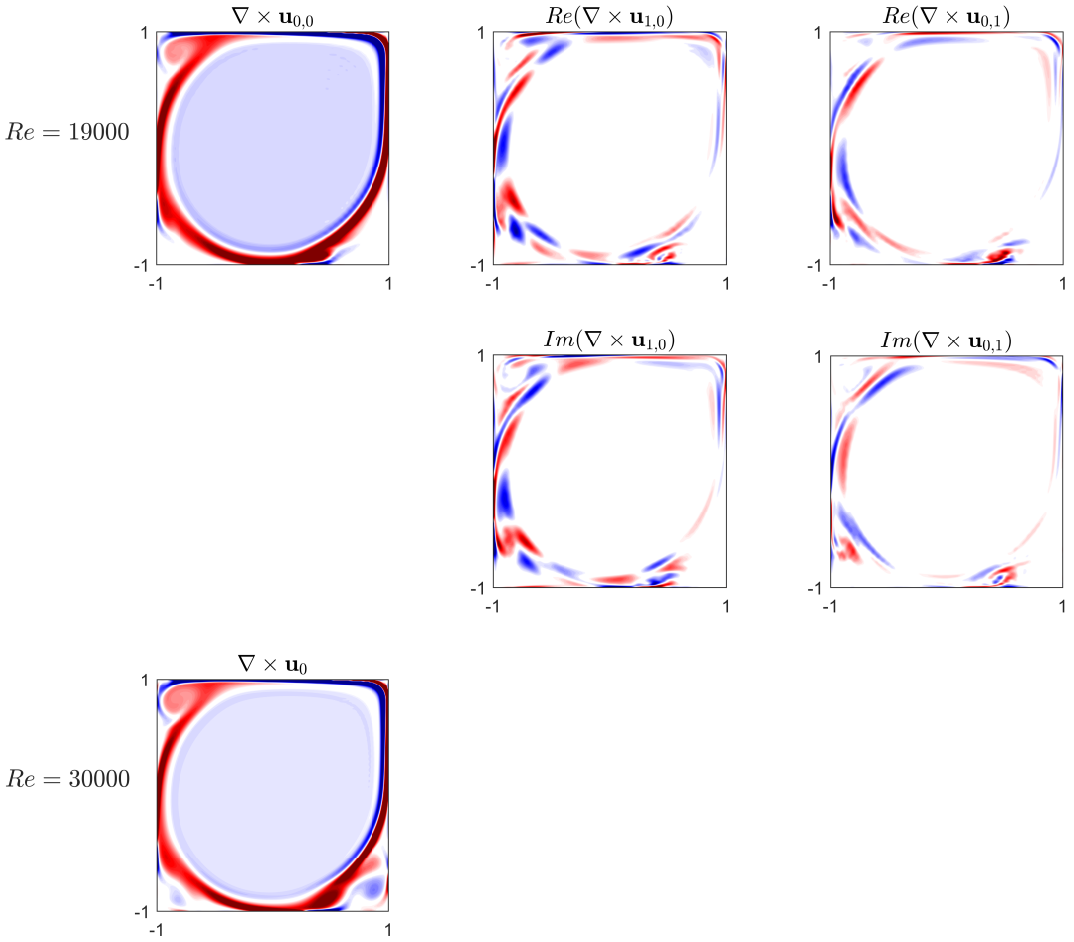

Figure 2.5: The Koopman modes of the cavity flow associated with basic Koopman frequencies: The color field shows the real part of vorticity, with clockwise rotation shown in red, and counterclockwise in blue. The general structure of Koopman modes associated with same frequency trace remains unchanged as the Reynolds number is varied.

Koopman mode, and its structure is similar to the mean flow of periodic and quasi-periodic flow except for the intensification of the downstream eddy in the bottom right corner.

The oscillatory Koopman modes, on the other hand, describe the flow oscillations around the edge of the central vortex in the mean flow. To be more precise, the evolution of the mode $\mathbf{u}_k$ can be written as

$$\begin{aligned} \mathbf{u}(t) &= \mathbf{u}_k e^{i\omega_k t} + \overline{\mathbf{u}}_k e^{i\omega_k t}, \\ &= 2Re(\mathbf{u}_k)\cos\omega_k t - 2Im(\mathbf{u}_k)\sin\omega_k t. \end{aligned} \tag{2.49}$$

A careful examination of the figure shows that $Re(\mathbf{u}_k)$ and $Im(\mathbf{u}_k)$ are similar for each k but appear to be shifted in the direction along the shear layer of the mean flow. This observation is related to the fact that the unsteady motion in periodic and quasi-periodic regimes corresponds to wave(s) that travel along the downstream edge of the central vortex. This traveling wave structure is observed in the previous studies of cavity flow (see e.g. the sequence of flow snapshots in [74, 76]) but never characterized.

The Koopman modes provide a straightforward framework to characterize the traveling waves from the data. Let's consider a simple example first: let $[0, 1]$ be a periodic domain, over which, the general form of traveling wave is

$$f(\omega t - 2\pi k x),\ x \in [0, 1] \tag{2.50}$$

with f being 2π-periodic. Using the Fourier series expansion, we have

$$\begin{aligned} f(\omega t - 2\pi k x) &= \sum_{j=-\infty}^{\infty} e^{ij(\omega t - 2\pi k x)}, \\ &= \sum_{j=-\infty}^{\infty} e^{ij\omega t} e^{-2\pi j k x}. \end{aligned} \tag{2.51}$$

Clearly, the last expression is the KMD of f with the Koopman modes given as $f_j(x) = \exp -2\pi j k x$. Having this example in mind, we can compute the wave numbers (and phase velocity) of traveling waves in the cavity flow through the following steps: First, we compute the phase of each Koopman mode given by

$$\theta_k := \angle \mathbf{u}_k = \tan^{-1}\left(\frac{Re(\mathbf{u}_k)}{Im(\mathbf{u}_k)}\right). \tag{2.52}$$

Then, we sample the values of θ_k along the direction of travel, denoted by $\hat{x}$, and compute the average local slope of $\theta_k(\hat{x})$ to get the wave number of the mode. This process is summarized in FIG. 2.6 (a) for the Koopman mode $\mathbf{u}_1$ of the periodic flow at $Re = 13000$. The results of this computation for different Koopman modes (shown in FIG. 2.6(b)) indicates that the Koopman modes associated with higher frequencies have proportionally higher wave numbers. This is expected from the KMD expansion of traveling wave (2.51). Moreover, it suggests that the wave numbers rarely change with the Reynolds number, however the phase velocity (slope of the lines in FIG. 2.6(b)) slightly decreases due to the decrease in the Koopman frequencies. We note that the above methodology based on Koopman modes is in fact a boiled down and cleaner version of a popular technique for extraction of the wave numbers from experimental data. Examples of application for this technique which is based on Hilbert transform are the study nonlinear waves in thermally-driven flows [110, 111], and internal waves in stratified flows [112].

An interesting observation is that the oscillatory Koopman modes show a remarkable

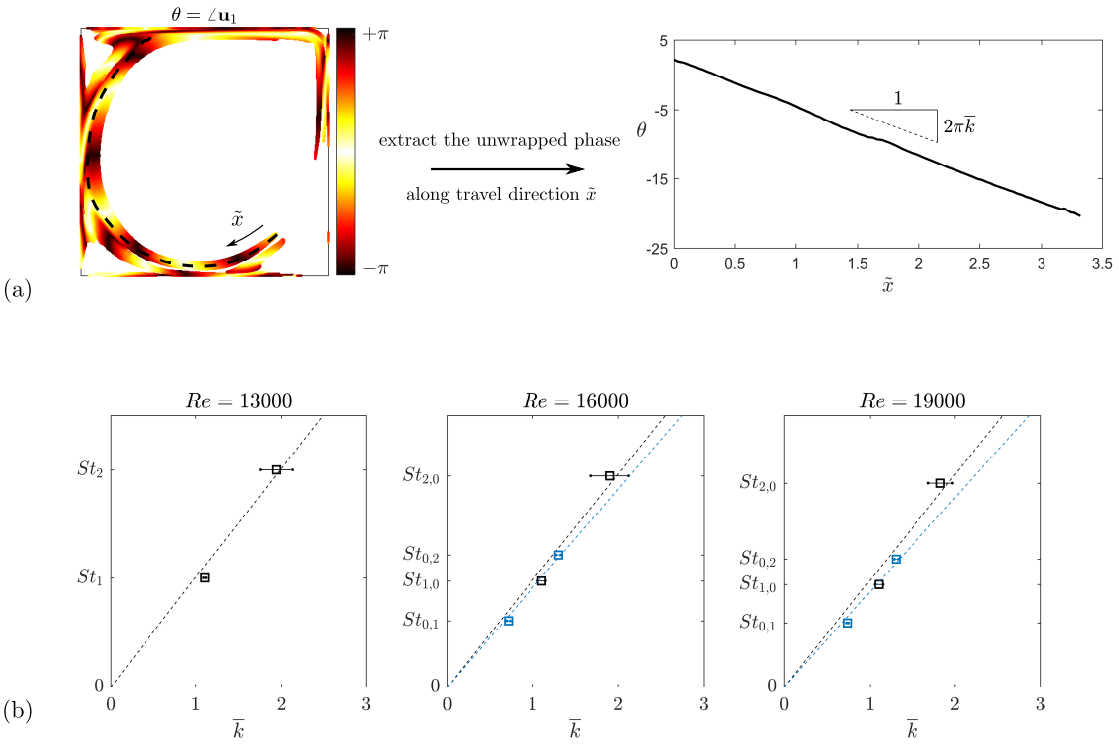

Figure 2.6: (a) The process of extracting the (spatial) wave number from each Koopman mode and (b) relationship between the Koopman frequency and wave number of Koopman modes.

structural robustness in the range $Re = 11000 - 19000$, despite the flow undergoing bifurcations from periodic to quasi-periodic and then skew-periodic. An examples of this robustness are the modes in panel 2, 7 and 12 in FIG. 2.5 (counting from top left to right) which correspond to the frequency trace of $St_{1,0}$ in periodic, quasi-periodic and mixed-spectra regimes, and panel 8 and 13 associated with the frequency $St_{0,2}$ in quasi-periodic and mixed-spectra regimes. This observation suggests that Koopman modes may provide a suitable basis for reduced modeling of flows (e.g. [113]) over wide range of Reynolds number.

2.6.4 Spectral Projections and Proper Orthogonal Decomposition (POD)

We study the the efficiency of Koopman modes in representing the flow, by computing the error of the spectral-projection models. An $n-$dimensional spectral projection model, is an n-term truncation of the KMD where the modes are sorted based on their kinetic energy. The error defined as

$$\tilde{e}(n) = \frac{1}{T}\int_0^T \left\| \mathbf{u}(\mathbf{x},t) - \sum_{k=1}^{n} \mathbf{u}_k(\mathbf{x}) e^{i\omega_k t} \right\| dt \tag{2.53}$$

gives the kinetic-energy norm of the difference between the spectral projection model (the sum in the above expression) and the actual flow field. Given the finite-dimensional nature of these models, they are essentially quasi-periodic approximations of the flow. The time-averaged kinetic energy of the error for the spectral projections of order 1-10 is shown in FIG. 2.7. In the periodic and quasi-periodic flows, the bulk of the motion is readily captured by a few Koopman modes and the low-order projections approximate the flow with great accuracy. As the flow becomes less periodic with the increase of

Reynolds number, the approximation error increases as well. For fully chaotic flows, the only Koopman mode is the mean flow and therefore there are no low-dimensional spectral projections except the steady one-dimensional model which is the mean flow itself. For purpose of comparison, however, we have plotted the error of spectral projections using Fourier modes (computed via FFT) at Re=30000. The kinetic energy of unsteady motion in this flow is spread in the continuous spectrum and any low-dimensional approximation using oscillatory components would involve large errors.

Figure 2.7 also shows an instructive comparison between Koopman mode decomposition and the Proper Orthogonal Decomposition (POD). POD is a decomposition of the flow field into spatially-orthogonal modes such that the POD-truncated models have the minimum energy error among all choices of orthogonal decompositions [114]. Due to its optimality and advantageous numerical properties, POD has been the keystone of many studies on coherent structures and low-order modeling of complex flows, incldiung the lid-driven cavity flow [75, 77]. In case of periodic and quasi-periodic flow,

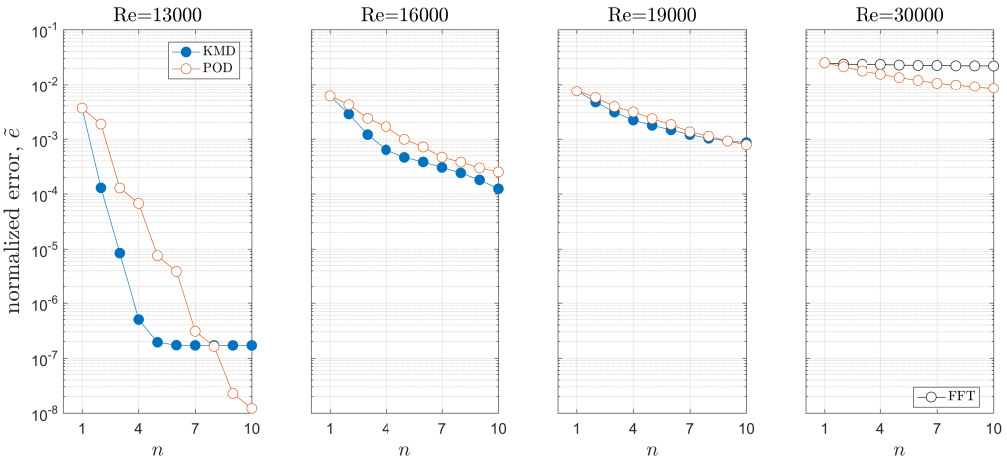

Figure 2.7: The normalized kinetic energy of the error for approximation in Koopman mode decomposition (KMD) and Proper Orthogonal Decomposition (POD) as function of number of modes used in the approximation (n). For $Re = 30000$ FFT modes are used in lieu of Koopman modes.

the low-dimensional spectral projection model gives a better approximation than POD-

truncated models (first two panels in FIG. 2.7). This observation is not contradictory to the optimality of POD-truncated models, but due to the fact that Koopman modes are complex-valued for oscillating systems which allows for better representation of dynamics evolving on limit cycles or torus as previously suggested in [10](see example 4 therein). We speculate that this observations would be valid for other flows that may exhibit strong quasi-periodic behavior over some parameter range, for example, periodically-driven flows (e.g. [115]), rotating Couette flow [116] and Rayleigh-Bernard convection [48], flow in converging-diverging channel [117] and behind bluff objects [50].

For flows with mixed spectra, the error of approximation with spectral projection and POD is generally comparable but as the Reynolds number increases and the flow becomes more chaotic, POD-truncated models perform better. These observations support the alternative decomposition for model reduction proposed in [10], in which, the KMD is used to extract the periodic components of the flow, and then POD is used for representation of the remaining chaotic component.

2.7 Summary

In this chapter, we proposed a new approach for computation of Koopman spectrum and modes, which comprises of a high-resolution algorithm to detect the eigenvalues, and an averaging estimation of the continuous spectrum. In contrast to DMD-type algorithms, this methodology is capable of computing the continuous spectrum of the Koopman operator and detecting genuine Koopman frequencies for flows with mixed spectra.

We also used the spectral properties of the Koopman operator for analysis of a post-transient flow. Understanding of the asymptotic dynamics in the state space of the flow is achieved by inspecting the Koopman spectrum and eigenfunctions obtained by KMD

of numerical flow data. In case of periodic or quasi-periodic attractors, the dominant Koopman frequencies possess a lattice-type structure whereas chaotic flows are associated with the continuous part of the Koopman spectrum. In between these two regimes, we observed flows that exhibit a combination of chaotic and quasi-periodic behavior (i.e. skew-periodic attractor) which is associated with mixed Koopman spectrum. The Koopman eigenfunctions, on the other hand, determine the directions of linear evolution on quasi-periodic and skew-periodic attractors.

Study of unsteady lid-driven cavity flow suggests that in case of periodic and quasi-periodic flow, a handful of Koopman modes are sufficient to represent the spatio-temporal patterns. In fact, the Koopman modes offer a more efficient representation of such flows than POD modes. This is due to the fact that complex-valued Koopman modes are more suitable for describing the evolution on limit cycles and tori.

Chapter 3

DMD and computation of Koopman spectrum for systems with ergodic attractors

[1] Dynamic Mode Decomposition, or DMD in short, is a linear data decomposition technique which was introduced by P. J. Schmid in the context of fluid mechanics [12]. Short after the introduction of this method, it was speculated in [11] that linear expansion in DMD provides a finite dimensional approximation of the Koopman mode decomposition (1.13). Since then, DMD has become the de facto method for computation of Koopman modes in high-dimensional systems. In this chapter, we establish the convergence of a class of DMD algorithm, called Hankel-DMD, for computation of the Koopman eigenvalues and eigenfunctions for systems with ergodic attractors.

The Hankel-DMD algorithm acts on data coming from observables, arranged in Hankel-type matrices. Our proof for convergence relies on the observation that vector

[1]The contents of this chapter are previously published in SIAM Journal of Applied Dynamical Systems, and reproduced here with permission from SIAM.

projections in DMD can be used to approximate the function projections by the virtue of Birkhoff's ergodic theorem. Using this fact, we show that applying DMD to Hankel data matrices in the limit of infinite-time observations yields the true Koopman eigenfunctions and eigenvalues. We also show that the Singular Value Decomposition (SVD), which is the central part of most DMD algorithms, converges to the Proper Orthogonal Decomposition (POD) of observables on ergodic sets. We use this result to obtain a representation of the dynamics of systems with continuous spectrum based on the lifting of the coordinates to the space of observables. The numerical application of these methods is demonstrated using well-known dynamical systems and example of lid-riven cavity flow discussed in the previous chapters.

The Hankel matrices of data are created by delay-embedding of time series measurements on the observables. Delay-embedding is an established method for geometric reconstruction of attractors for nonlinear systems based on measurements of generic observables [109, 118]. By combining delay-embedding with DMD, we are able to extract analytic information about the state space (such as the frequency of motion along the quasi-periodic attractor or the structure of isochrons) which cannot be computed from geometric reconstruction. On the other hand, Hankel matrices are extensively used in the context of linear system identification (e.g. [119, 120]). The relationship between KMD and linear system identification methods was first pointed out in [33]. It was shown that applying DMD to the Hankel data matrix recovers the same linear system, up to a similarity transformation, as the one obtained by Eigensystem Realization Algorithm (ERA)[119]. In a more recent study, Brunton *et al.* [121] proposed a new framework for Koopman analysis using the Hankel-matrix representation of data. Using this framework, they were able to extract a linear system with intermittent forcing that could be used for local predictions of chaotic systems (also see [43] and [27]). Our work strengthens the above results by providing a rigorous connection between linear analysis

of delay-embedded data and identification of nonlinear systems using the Koopman operator theory. The key element in our methodology is to use the vector projections of DMD to approximate the projections of observables in the Hilbert space of functions defined on the attractor. This observation has already been utilized in a different approach for study of the Koopman operator [122]. We also note that the Hankel-DMD algorithm is closely related to the Prony approximation of KMD [92], and it can interpreted as a variation of Extended DMD algorithm [31] on ergodic trajectories (also see [123]).

The outline of this chapter is as follows: In 3.1, we describe a few important variants of DMD algorithm. In 3.2, we review some elementary ergodic theory, the Hankel representation of data and prove the convergence of the companion-matrix Hankel-DMD method. In 3.2.1, we extend the application of this method to observations on trajectories that converge to an ergodic attractors. In 3.3, we point out a new connection between the SVD on data matrices and POD on the ensemble of observables on ergodic dynamical systems. By using this interpretation of SVD, we are able to show the convergence of the Exact DMD for ergodic systems in 3.4. These results enable us to extract the Koopman spectral properties from measurements on multiple observables. We recapitualte the Hankel-DMD algorithm and present some numerical examples in 3.5. We summarize our results in 3.6.

3.1 Review of DMD

The original goal of DMD algorithm (in [12]) was to extract the spatial flow structures that evolve linearly with time, i.e., the structures that grow or decay exponentially - possibly with complex exponents. The connection between this numerical algorithm and the linear expansion of observables in KMD was first noted in [11], and a different variant of this algorithm was used to compute the Koopman modes of a jet in cross

flow. The initial success of this algorithm in the context of fluid mechanics motivated an ongoing line of research on data-driven analysis of high-dimensional and complex systems using the Koopman operator theory, and consequently, a large number of DMD-type algorithms have been proposed in the recent years for computation of the Koopman spectral properties [38, 33, 31, 35, 34].

The three variants of DMD that we consider here are the *companion-matrix DMD* [11], the *SVD-enhanced DMD* [12], and the *Exact DMD* [33]. The SVD-enhanced and Exact variants of DMD are more suitable for numerical implementation, while the companion-matrix method enables a more straightforward proof for the first result of this chapter. In the following, we first describe the mathematical settings for application of DMD, and then describe the above three algorithms and the connections between them.

In this chapter, we will use a slightly different notation from previous chapters to avoid confusion with the notation for data matrices. We will consider the discrete-time dynamical system

$$\mathbf{z}' = \mathbf{T}(\mathbf{z}), \tag{3.1}$$

where $\mathbf{z} \in M$ is the state, and we let

$$\mathbf{f} := \begin{bmatrix} f_1 \\ f_2 \\ \vdots \\ f_n \end{bmatrix} : M \to \mathbb{R}^n \tag{3.2}$$

be a vector-valued observable defined on the dynamical system in (3.1), and let

$$D := \begin{bmatrix} f_1(z_0) & f_1 \circ T(z_0) & \dots & f_1 \circ T^m(z_0) \\ f_2(z_0) & f_2 \circ T(z_0) & \dots & f_2 \circ T^m(z_0) \\ \vdots & \vdots & \ddots & \vdots \\ f_n(z_0) & f_n \circ T(z_0) & \dots & f_n \circ T^m(z_0) \end{bmatrix} \tag{3.3}$$

be the matrix of measurements recorded on $\mathbf{f}$ along a trajectory starting at the initial condition $z_0 \in M$. Each column of D is called a *data snapshot* since it contains the measurements on the system at a single time instant. Assuming only discrete eigenvalues for the Koopman operator, we can rewrite the Koopman mode expansion in (1.13) for each snapshot in the form of

$$D_i := \begin{bmatrix} f_1 \circ T^i(z_0) \\ f_2 \circ T^i(z_0) \\ \vdots \\ f_n \circ T^i(z_0) \end{bmatrix} = \sum_{j=1}^{\infty} \lambda_j^i \mathbf{v}_j \tag{3.4}$$

by absorbing the scalar values of $\phi_j(z_0)$ into the mode $\mathbf{v}_j$. In numerical approximation of the Koopman modes, however, we often assume this expansion is finite dimensional and use

$$\mathbf{f}^i = \sum_{j=1}^{n} \tilde{\lambda}_j^i \tilde{\mathbf{v}}_j \tag{3.5}$$

where $\tilde{\mathbf{v}}_j$ and $\tilde{\lambda}_j$ are approximations to the Koopman modes and eigenvalues in (3.4). This expansion resembles the spectral expansion for a linear operator acting on $\mathbb{R}^n$. This operator, which maps each column of D to the next is called the *DMD operator*. The

general strategy of DMD algorithms is to construct the DMD operator, in the form of a matrix, and extract the dynamic modes and eigenvalues from the spectrum of that matrix. In the companion-matrix DMD (algorithm 3), as the name suggests, the DMD operator is realized in the form of a companion matrix:

Algorithm 3 Companion-matrix DMD

Consider the data matrix D defined in (3.3).

1: Define $X = [D_0\ D_1\ \ldots\ D_{m-1}]$

2: Form the companion matrix

$$\tilde{C} = \begin{pmatrix} 0 & 0 & \ldots & 0 & \tilde{c}_0 \\ 1 & 0 & \ldots & 0 & \tilde{c}_1 \\ 0 & 1 & \ldots & 0 & c_2 \\ \vdots & \vdots & \ddots & \vdots & \vdots \\ 0 & 0 & \ldots & 1 & c_{m-1} \end{pmatrix}, \tag{3.6}$$

with

$$\begin{pmatrix} c_0, & c_1, c_2, & \ldots, & c_{m-2} \end{pmatrix}^T = X^\dagger D_m.$$

The $X^\dagger$ denotes the Moore-Penrose pseudo-inverse of X [124].

3: Let $(\lambda_j, w_j),\ j = 1, 2, \ldots, m$ be the eigenvalue-eigenvector pairs for $\tilde{C}$. Then λ_j's are the dynamic eigenvalues. Dynamic modes $\tilde{v}_j$ are given by

$$\tilde{v}_j = X w_j, \quad j = 1, 2, \ldots, m. \tag{3.7}$$

In the above algorithm, the companion matrix $\tilde{C}$ is the realization of the DMD operator in the basis which consists of the columns in X. The pseudo-inverse in step 2

is used to project the last snapshot of D onto this basis. In the case that D_m lies in the range of X, we have

$$r := D_m - X(X^\dagger D_m) = 0 \tag{3.8}$$

which means that the companion matrix $\tilde{C}$ exactly maps each column of D to the next. If columns of X are linearly dependent, however, the above projection is not unique, and the problem of determining the DMD operator is generally over-constrained. Furthermore, when X is ill-conditioned, the projection in step 2 becomes numerically unstable.

The SVD-enhanced DMD algorithm (algorithm 4), offers a more robust algorithm for computation of dynamic modes and eigenvalues:

Algorithm 4 SVD-enhanced DMD

Consider the data matrix D defined in (3.3).

1: Define $X = [D_0\ D_1\ \ldots\ D_{m-1}]$ and $Y = [D_1\ D_2\ \ldots\ D_m]$

2: Compute the SVD of X:

$$X = WS\tilde{V}^*.$$

3: Form the matrix

$$\hat{A} = W^*Y\tilde{V}S^{-1}.$$

4: Let $(\lambda_j, w_j),\ j = 1, 2, \ldots, m$ be the eigenvalue-eigenvector pairs for $\hat{A}$. Then λ_j's are the dynamic eigenvalues. Dynamic modes $\tilde{v}_j$ are given by

$$\tilde{v}_j = Ww_j, \quad j = 1, 2, \ldots, m.$$

In this method, the left singular vectors W are used as the basis to compute a realization of the DMD operator, which is $\hat{A}$. In fact, column vectors in W form an orthogonal basis which enhances the numerical stability of the projection process (the term W^*Y in step 3). When X is full rank and λ_j's are distinct, the dynamic modes and eigenvalues computed by this algorithm are the same as the companion-matrix algorithm [32].

The Exact DMD algorithm (algorithm 5) generalizes the SVD-enhanced algorithm to the case where the sampling of the data might be non-sequential. For example, consider the data matrices

$$X = \begin{bmatrix} f_1(z_0) & f_1(z_1) & \dots & f_1(z_m) \\ f_2(z_0) & f_2(z_1) & \dots & f_2(z_m) \\ \vdots & \vdots & \ddots & \vdots \\ f_n(z_0) & f_n(z_1) & \dots & f_n(z_m) \end{bmatrix} \tag{3.9}$$

and

$$Y = \begin{bmatrix} f_1 \circ T(z_0) & f_1 \circ T(z_1) & \dots & f_1 \circ T(z_m) \\ f_2 \circ T(z_0) & f_2 \circ T(z_1) & \dots & f_2 \circ T(z_m) \\ \vdots & \vdots & \ddots & \vdots \\ f_n \circ T(z_0) & f_n \circ T(z_1) & \dots & f_n \circ T(z_m) \end{bmatrix}, \tag{3.10}$$

where $\{z_0, z_1, \dots, z_m\}$ denotes a set of arbitrary states of the dynamical system in (3.1). The Exact DMD algorithm computes the operator that maps each column of X to the corresponding column in Y.

The finite-dimensional operator that maps the columns of X to Y is known as the

Algorithm 5 Exact DMD

Consider the data matrices X and Y defined in (3.9) and (3.10).

1: Define $X = [D_0\ D_1\ \dots\ D_{m-1}]$ and $Y = [D_1\ D_2\ \dots\ D_m]$

2: Compute the SVD of X:

$$X = WS\tilde{V}^*.$$

3: Form the matrix

$$\hat{A} = W^*Y\tilde{V}S^{-1}.$$

4: Let $(\lambda_j, w_j),\ j = 1, 2, \dots, m$ be the eigenvalue-eigenvector pairs for $\hat{A}$. Then λ_j's are the dynamic eigenvalues.

5: The exact dynamic modes $\tilde{v}_j$ are given by

$$\tilde{v}_j = \frac{1}{\lambda_j} Y\tilde{V}S^{-1}w_j, \quad j = 1, 2, \dots, m.$$

6: The projected dynamic modes χ_j are given by

$$\chi_j = Ww_j, \quad j = 1, 2, \dots, m.$$

Exact DMD operator, with the explicit realization,

$$\tilde{A} = YX^{\dagger}. \tag{3.11}$$

The matrix $\tilde{A}$ is not actually formed in algorithm 5, however, the dynamic eigenvalues and exact dynamic modes form the eigen-decomposition of $\tilde{A}$. We note that the projected dynamic modes and exact dynamic modes coincide if the column space of Y lie in the range of X. Moreover, applying Exact DMD to X and Y matrices defined in algorithm 4 yields the same eigenvalues and modes as SVD-enhanced DMD.

In the following, we will show how DMD operators converge to a finite-dimensional representation of the Koopman operator for ergodic systems. The critical observation that enables us to do so, is the fact that vector projections in the DMD algorithm can

be used to approximate the projections in the function space of observables.

3.2 Ergodic theory and Hankel-matrix representation of data

In this section, we recall the elementary ergodic theory and give a new interpretation of Hankel-matrix representation of data in the context of the Koopman operator theory. The main result of this section is proposition 3 which asserts the convergence of companion-matrix Hankel-DMD for computation of Koopman spectrum. Despite the intuitive proof of its convergence, this method is not well-suited for numerical practice, and a more suitable alternative for numerical computation will be presented in section 3.4 and 3.5. In section 3.2.1, we present analogous results for the basin of attraction of ergodic attractors.

Consider the dynamics on a compact invariant set A, possibly the attractor of a dissipative dynamical system, given by the measure-preserving map $T : A \to A$. Let μ be the preserved measure with $\mu(A) = 1$, and assume that for every invariant set $B \subset A$, $\mu(B) = 0$ or $\mu(A - B) = 0$, i.e., the map T is ergodic on A. A few examples of ergodic sets in dynamical systems are limit cycles, tori with uniform flow and chaotic sets like Lorenz attractor. We define the Hilbert space $\mathcal{H}$ to be the set of all observables on A which are square-integrable with respect to the measure μ, i.e.,

$$\mathcal{H} := \{f : A \to \mathbb{R} \ s.t. \ \int_A |f|^2 d\mu < \infty\}. \tag{3.12}$$

The Birkhoff's ergodic theorem [125] asserts the existence of infinite-time average of such observables and relates it to the spatial average over the set A. More precisely, if $f \in \mathcal{H}$,

then

$$\lim_{N\to\infty}\frac{1}{N}\sum_{k=0}^{N-1} f\circ T^k(z) = \int_A f d\mu, \quad \text{for almost every } z\in A. \tag{3.13}$$

An important consequence of this theorem is that the inner products of observables in $\mathcal{H}$ can be approximated using the time series of observations. To see this, denote by $\tilde{f}_m(z_0)$ and $\tilde{g}_m(z_0)$ the vector of m sequential observations made on observables $f, g \in \mathcal{H}$ along a trajectory starting at z_0,

$$\tilde{f}_m(z_0) = [f(z_0),\ f\circ T(z_0),\ \ldots,\ f\circ T^{m-1}(z_0)] \tag{3.14a}$$

$$\tilde{g}_m(z_0) = [g(z_0),\ g\circ T(z_0),\ \ldots,\ g\circ T^{m-1}(z_0)] \tag{3.14b}$$

Then for almost every $z_0 \in A$,

$$\lim_{m\to\infty}\frac{1}{m} < \tilde{f}_m(z_0), \tilde{g}_m(z_0) > = \lim_{m\to\infty}\frac{1}{m}\sum_{k=0}^{m-1}(fg^*)\circ T^k(z_0) = \int_A fg^* d\mu = < f, g >_{\mathcal{H}} \tag{3.15}$$

where we have used $< ., . >$ for vector inner product and $< ., . >_{\mathcal{H}}$ for the inner product of functions in $\mathcal{H}$. The key observation in this work is that using the data vectors such as $\tilde{f}_m(z_0)$ we can approximate the projection of observables onto each other according to (3.15).

Now consider the longer sequence of observations

$$\tilde{f}_{m+n} = [f(z_0),\ f\circ T(z_0),\ \ldots,\ f\circ T^{m-1}(z_0),\ \ldots, f\circ T^{m+n-1}(z_0)]$$

which could be rearranged into a Hankel matrix by delay-embedding of dimension m,

$$\tilde{H} = \begin{pmatrix} f(z_0) & f \circ T(z_0) & \dots & f \circ T^{n}(z_0) \\ f \circ T(z_0) & f \circ T^{2}(z_0) & \dots & f \circ T^{n+1}(z_0) \\ \vdots & \vdots & \ddots & \vdots \\ f \circ T^{m-1}(z_0) & f \circ T^{m}(z_0) & \dots & f \circ T^{m+n-1}(z_0) \end{pmatrix} \tag{3.16}$$

Given the definition of the Koopman operator in (1.5), we also observe that $j-$th column of this matrix is the sampling of the observable $U^{j-1}f$ along the same trajectory, and we can rewrite it in a more compact form,

$$\tilde{H} = \left(\tilde{f}_m,\ U\tilde{f}_m, \dots,\ U^n \tilde{f}_m \right).$$

This matrix can be viewed as a sampling of the Krylov sequence of observable f, defined as

$$\mathcal{F}_n := [f,\ Uf,\ \ \dots,\ U^n f].$$

The basic idea of the Hankel-DMD method is to extract the Koopman spectra from this sequence, which is analogous to the idea of Krylov subspace methods for computing the eigenvalues of large matrices [126]. A simplifying assumption that we utilize in most of this chapter is that there exists a finite-dimensional subspace of $\mathcal{H}$ which is invariant under the action of the Koopman operator and contains our observable of interest f. In general, the existence of finite-dimensional Koopman-invariant subspaces is equivalent to the existence of the eigenvalues (i.e. discrete spectrum) for Koopman operator. To be more precise, if such invariant subspace exists, then the Koopman operator restricted to this subspace can be realized in the form of a finite-dimensional matrix and therefore it

must have at least one (complex) eigenvalue. Conversely, if the Koopman operator has eigenvalues, the span of a finite number of associated eigenfunctions forms an invariant subspace. However, it is not guaranteed that the arbitrary observables such as f are contained within such subspaces.

Let k be the dimension of the minimal Koopman-invariant subspace, denoted by $\mathcal{K}$, which contains f. Then the first k iterates of f under the action of the Koopman operator span $\mathcal{K}$, i.e.,

$$\mathcal{K} = \text{span}(\mathcal{F}_n), \text{ for every } n \geq k-1 \tag{3.17}$$

This condition follows from the fact that the Koopman eigenvalues are simple for ergodic systems [62], and as a result, f is cyclic in $\mathcal{K}$ [63]. The following proposition shows that the eigenvalues and eigenfunctions obtained by applying DMD to $\tilde{H}$ converge to true eigenfunctions and eigenvalues of the Koopman operator. Our proof strategy is to show that companion matrix formed in algorithm 3 approximates the $k-$by$-k$ matrix which represents the Koopman operator restricted to $\mathcal{K}$.

Proposition 3 (Convergence of the companion-matrix Hankel-DMD algorithm) *Let the dynamical system in* (3.1) *be ergodic, and* $\mathcal{F}_n = [f,\ Uf, \ldots, U^n f]$ *span a* k*-dimensional subspace of* $\mathcal{H}$ *(with* $k < n$*) which is invariant under the action of the Koopman operator. Consider the dynamic eigenvalues and dynamic modes obtained by applying the companion-matrix DMD (algorithm 3) to the first* $k+1$ *columns of the Hankel matrix* $\tilde{H}_{m\times n}$ *defined in* (3.16).

Then, for almost every z_0*, as* $m \to \infty$*:*

(a) The dynamic eigenvalues converge to the Koopman eigenvalues associated with the k*-dimensional subspace.*

(b) The dynamic modes converge to the sampling of associated Koopman eigenfunctions on the trajectory starting at z_0*.*

Proof: Consider the first k elements of $\mathcal{F}_n$,

$$\left(f,\ Uf,\ \ldots, U^{k-1}f\right) \tag{3.18}$$

which are linearly independent. These observables provide a basis for $\mathcal{K}$, and the restriction of Koopman operator to $\mathcal{K}$ can be (exactly) realized as the companion matrix

$$C = \begin{pmatrix} 0 & 0 & \ldots & 0 & c_0 \\ 1 & 0 & \ldots & 0 & c_1 \\ 0 & 1 & \ldots & 0 & c_2 \\ \vdots & \vdots & \ddots & \vdots & \vdots \\ 0 & 0 & \ldots & 1 & c_{k-1} \end{pmatrix}$$

where the last column is the coordinate vector of the function $U^k f$ in the basis, and it is given by

$$\begin{bmatrix} c_0 \\ c_1 \\ \vdots \\ c_{k-1} \end{bmatrix} = G^{-1} \begin{bmatrix} < f, U^k f >_{\mathcal{H}} \\ < Uf, U^k f >_{\mathcal{H}} \\ \vdots \\ < U^{k-1} f, U^k f >_{\mathcal{H}} \end{bmatrix} \tag{3.19}$$

Here, G is the Gramian matrix of the basis given by

$$G_{ij} =< U^{i-1} f, U^{j-1} f >_{\mathcal{H}} .$$

Now consider the numerical companion-matrix DMD algorithm and let X be the matrix that contains the first k columns of $\tilde{H}$. When applied to the first $k+1$ columns of $\tilde{H}$, the algorithm seeks the eigenvalues of the companion matrix $\tilde{C}$, whose last column is given

by

$$\begin{bmatrix} \tilde{c}_0 \\ \tilde{c}_1 \\ \vdots \\ \tilde{c}_{k-1} \end{bmatrix} = X^\dagger U^k \tilde{f}_m = \tilde{G}^{-1} \begin{bmatrix} \frac{1}{m} < \tilde{f}_m, U^k \tilde{f}_m > \\ \frac{1}{m} < U\tilde{f}_m, U^k \tilde{f}_m > \\ \vdots \\ \frac{1}{m} < U^{k-1}\tilde{f}_m, U^k \tilde{f}_m > \end{bmatrix} \tag{3.20}$$

In the second equality, we have used the following relationship for the Moore-Penrose pseudo-inverse of a full-rank data matrix X,

$$X^\dagger = (X^*X)^{-1}X^* = (\frac{1}{m}X^*X)^{-1}(\frac{1}{m}X^*) := \tilde{G}^{-1}(\frac{1}{m}X^*).$$

and defined the numerical Gramian matrix by

$$\tilde{G}_{ij} = \frac{1}{m} < U^{i-1}\tilde{f}_m, U^{j-1}\tilde{f}_m > .$$

The averaged inner products in the rightmost vector of (3.20) converge to the vector of Hilbert-space inner products in (3.19), due to (3.15). The same argument suggests element-wise convergence of the numerical Gramian matrix to the G in (3.19), i.e.,

$$\lim_{m\to\infty} \tilde{G}_{ij} = G_{ij}.$$

Furthermore

$$\lim_{m\to\infty} \tilde{G}^{-1} = \left(\lim_{m\to\infty} \tilde{G}\right)^{-1} = G^{-1}$$

We have interchanged the limit and inverting operations in the above since G is invertible (because the basis is linearly independent). Thus the DMD operator $\tilde{C}$ converges to the

Koopman operator realization C. The eigenvalues of matrix are depend continuously on its entries which guarantees the convergence of the eigenvalues of $\tilde{C}$ to the eigenvalues of C as well. This proves the statement in (a). Now let v_k be the set of normalized eigenvectors of C, that is,

$$Cv_j = \lambda_j v_j,\ \|v_j\| = 1,\ j = 1, \ldots, k.$$

These eigenvectors give the coordinates of Koopman eigenfunctions in the basis of (3.18). Namely, $\phi_j,\ j = 1, \ldots, k$ defined by

$$\phi_i = \left(f,\ Uf,\ \ldots, U^{k-1}f\right) v_i, \quad i = 1, \ldots, k. \tag{3.21}$$

are a set of Koopman eigenfunctions in the invariant subspace. Given the convergence of $\tilde{C}$ to C and convergence of their eigenvalues, the normalized eigenvectors of $\tilde{C}$, denoted by $\tilde{v}_j,\ j = 0, 1, \ldots, k$ also converge to v_j's. We define the set of candidate functions by

$$\tilde{\phi}_i = \left(f,\ Uf,\ \ldots, U^{k-1}f\right) \tilde{v}_i, \quad i = 1, \ldots, k. \tag{3.22}$$

and show that they converge to ϕ_i as $m \to \infty$. Consider an adjoint basis of (3.18) denoted by $\{g_j\},\ j = 0, 1, .., k-1$ defined such that $< g_i, U^j f >_{\mathcal{H}} = \delta_{ij}$ with δ being the Kronecker delta. We have

$$\lim_{m\to\infty} < \tilde{\phi}_i, g_j >_{\mathcal{H}} = \lim_{m\to\infty} \tilde{v}_{ij} = v_{ij} = < \phi_i, g_j >_{\mathcal{H}}$$

where v_{ij} is the $i-$th entry of v_j. The above statement shows the *weak* convergence of the $\tilde{\phi}_j$ to ϕ_j for $j = 1, \ldots, k$. However, both set of functions belong to the same *finite*-dimensional subspace and therefore weak convergence is strong convergence. The j-th

dynamic mode given by

$$w_i = \left(\tilde{f}_m,\ U\tilde{f}_m,\ \ \ldots, U^{k-1}\tilde{f}_m\right)\tilde{v}_i \tag{3.23}$$

is the sampling of $\tilde{\phi}_j$ along the trajectory, and convergence of $\tilde{\phi}_j$ means that w_j converges to the value of Koopman eigenfunction ϕ_j on the trajectory starting at z_0. The proposition is valid for almost every initial condition for which the ergodic average in (3.13) exists. ■

Remark 1 *In the above results, the data vectors can be replaced with any sampling vector of the observables that satisfy the convergence of inner products as in* (3.15)*. For example, instead of using* $\tilde{f}$ *as defined in* (3.14a)*, we can use the sampling vectors of the form*

$$\hat{f}_m(z_0) = [f(z_0),\ f\circ T^l(z_0),\ f\circ T^{2l}(z_0),\ \ \ldots,\ f\circ T^{(m-1)l}(z_0)]$$

where l *is a positive finite integer.*

3.2.1 Extension of Hankel-DMD to the basin of attraction

Consider the ergodic set A to be an attractor of the dynamical system (3.1) with a basin of attraction $\mathcal{B}$. The existence of ergodic average in (3.13) can be extended to trajectories starting in $\mathcal{B}$ by assuming that the invariant measure on A is a physical measure [127, 128]. To formalize this notion, let ν denote the standard Lebesgue measure on $\mathcal{B}$. We assume that there is a subset $B \subset \mathcal{B}$ such that $\nu(\mathcal{B}-B) = 0$ and for every initial condition in B the ergodic averages of continuous functions exist. That is, if $f : \mathcal{B} \to \mathbb{R}$

is continuous, then

$$\lim_{N\to\infty} \frac{1}{N} \sum_{k=0}^{N} f \circ T^k(z) = \int_A f d\mu, \quad \text{for } \nu-\text{almost every } z \in \mathcal{B}. \tag{3.24}$$

Roughly speaking, this assumption implies that the invariant measure μ rules the asymptotics of almost every trajectory in $\mathcal{B}$, and therefore it is relevant for physical observations and experiments. Using (3.24), we can extend proposition 3 to the trajectories starting almost everywhere in $\mathcal{B}$. The only extra requirement is that *the observable must be continuous in the basin of attraction.*

Proposition 4 (Convergence of Hankel-DMD in the basin of attraction)
Let A be the ergodic attractor of the dynamical system (3.1) *with the basin of attraction $\mathcal{B}$ which supports a physical measure. Assume $f : \mathcal{B} \to \mathbb{R}$ is a continuous function with $f|_A$ belonging to a k-dimensional Koopman-invariant subspace of $\mathcal{H}$. Let $\tilde{H}$ be the Hankel matrix* (3.16) *of observations on f along the trajectory starting at $z_0 \in \mathcal{B}$ with $n > k$. Consider the dynamic modes and eigenvalues obtained by applying the companion-matrix DMD (algorithm 3) to the first $k+1$ columns of $\tilde{H}$.*

Then, for $\nu-$almost every z_0, as $m \to \infty$:

(a) The dynamic eigenvalues converge to the Koopman eigenvalues.

(b) The dynamic modes converge to the value of associated eigenfunctions ϕ_j along the trajectory starting at z_0.

Proof: The proof of (a) is similar to proposition 3 and follows from the extension of ergodic averages to the basin of attraction by (3.24). To show that the dynamic mode w_j converges to Koopman eigenfunctions along the trajectory, we need to consider the

evolution of w_j under the action of the Koopman operator:

$$\begin{aligned}
\lim_{m\to\infty} Uw_j &= \lim_{m\to\infty} U[\tilde{f}_m, U\tilde{f}_m, \ldots, U^{k-1}\tilde{f}_m]\tilde{v}_j \\
&= \lim_{m\to\infty} [U\tilde{f}_m, U^2\tilde{f}_m, \ldots, U^k\tilde{f}_m]\tilde{v}_j \\
&= \lim_{m\to\infty} [\tilde{f}_m, U\tilde{f}_m, \ldots, U^{k-1}\tilde{f}_m]\tilde{C}\tilde{v}_j \\
&= \lim_{m\to\infty} [U\tilde{f}_m, U^2\tilde{f}_m, \ldots, U^k\tilde{f}_m]\tilde{\lambda}_j\tilde{v}_j \\
&= \lim_{m\to\infty} \tilde{\lambda}_j w_j \\
&= \lambda_j w_j.
\end{aligned}$$

Therefore, w_j converges to the sampling of values of the eigenfunction associated with eigenvalue λ_j. ■

3.3 SVD and POD for ergodic systems

SVD is a central algorithm of linear algebra that lies at the heart of many data analysis techniques for dynamical systems including linear subspace identification methods [120] and DMD [12, 33]. POD, on the other hand, is a data analysis technique frequently used for complex and high-dimensional dynamical systems. Also known as Principal Component Analysis (PCA), or Karhonen-Loeve decomposition, POD yields an orthogonal basis for representing ensemble of observations which is optimal with respect to a pre-defined inner product. It is known that for finite-dimensional observables on discrete-time dynamical systems, POD reduces to SVD [129]. Here, we establish a slightly different connection between these two concepts in the case of ergodic systems. Our motivation for derivation of these results is the role of SVD in DMD algorithms, however, the orthogonal basis that is generated by this process can be used for further

analysis of dynamics in the space of observables, for example, to construct a basis for computing the eigenfunctions of the Koopman generator as in [122]. We first review POD and then record our main result in proposition 5.

Let $\mathcal{F} = [f_1,\ f_2,\ \ldots,\ f_n]$ be an ensemble of observables in the Hilbert space $\mathcal{H}$ which spans a $k-$dimensional subspace. Applying POD to $\mathcal{F}$ yields the expansion

$$\begin{aligned} \mathcal{F} &= \Psi \Sigma V^*, \\ &= [\psi_1, \psi_2, \ldots, \psi_k] \begin{bmatrix} \sigma_1 & 0 & \ldots & 0 \\ 0 & \sigma_2 & \ldots & 0 \\ \vdots & \vdots & \ddots & \vdots \\ 0 & 0 & \ldots & \sigma_k \end{bmatrix} \begin{bmatrix} — & v_1^* & — \\ — & v_2^* & — \\ & \vdots & \\ — & v_k^* & — \end{bmatrix}, \end{aligned} \tag{3.25}$$

where ψ_j's, $j = 1, 2, \ldots, k$ form an orthonormal basis for span$\{\mathcal{F}\}$, and are often called the *empirical orthogonal functions* or *POD basis* of $\mathcal{F}$. The diagonal elements of Σ, denoted by $\sigma_j, j = 1, 2, \ldots, k$ are all positive and signify the $\mathcal{H}$-norm contribution of the basis element ψ_j to the $\mathcal{F}$. The columns of V, denoted by v_i and called the *principal coordinates*, are the normalized coordinates of vectors in $\mathcal{F}$ with respect to the POD basis. This decomposition can be alternatively written as a summation,

$$f_i = \sum_{j=1}^{k} \sigma_j \psi_j v_{ji}. \tag{3.26}$$

If we index the principal coordinates such that $\sigma_1 > \sigma_2 > \ldots > \sigma_k > 0$, then this decomposition minimizes the expression

$$e_p = \frac{1}{n} \sum_{i=1}^{n} \left\| \sum_{j=1}^{p} \sigma_j \psi_j v_{ji} - f_i \right\|_{\mathcal{H}}$$

for any $p \leq k$, over the choice of all orthonormal bases for span$\{\mathcal{F}\}$. The term e_p

denotes the average error in approximating f_i's by truncating the sum in (3.26) at length p. This property, by design, guarantees that low-dimensional representations of $\mathcal{F}$ using truncations of POD involves the least $\|\cdot\|_{\mathcal{H}}$-error compared to other choices of orthogonal decomposition.

An established method for computation of POD is *the method of snapshots* [130]: we first form the Gramian matrix G, given by $G_{ij} =< f_i, f_j >_{\mathcal{H}}$. The columns of V are given as the normalized eigenvectors of G associated with its non-zero eigenvalues, and those non-zero eigenvalues happen to be σ_i^2's, that is,

$$GV = V\Sigma^2. \tag{3.27}$$

Since G is a symmetric real matrix, V will be an orthonormal matrix and the decomposition in (3.25) can be easily inverted to yield the orthonormal basis functions,

$$\psi_j = \frac{1}{\sigma_j}\mathcal{F}v_j.$$

The SVD of tall rectangular matrix has a similar structure to POD. Consider $X_{m\times n}$, with $m > n$, to be a matrix of rank r. The *reduced SVD* of X is

$$\begin{aligned} X &= W S \tilde{V}^* \\ &= \begin{bmatrix} | & | & & | \\ w_1 & w_2 & \dots & w_r \\ | & | & & | \end{bmatrix} \begin{bmatrix} s_1 & 0 & \dots & 0 \\ 0 & s_2 & \dots & 0 \\ \vdots & \vdots & \ddots & \vdots \\ 0 & 0 & \dots & s_r \end{bmatrix} \begin{bmatrix} — & \tilde{v}_1^* & — \\ — & \tilde{v}_2^* & — \\ & \vdots & \\ — & \tilde{v}_r^* & — \end{bmatrix} \end{aligned} \tag{3.28}$$

where W and V are orthonormal matrices, and S is a diagonal matrix holding the singular values $s_1 > s_2 > \ldots > s_r > 0$. The columns of W and V are called, respectively, left and

right singular vectors of X.

The usual practice of POD in data analysis is to let $\mathcal{H}$ be the space of snapshots, e.g. $\mathbb{R}^m$ equipped with the usual Euclidean inner product, which makes POD and SVD identical [129]. In that case, $\mathcal{F}$ would be a snapshot matrix such as (3.3) and its left singular vectors are the POD basis. We are interested in $\mathcal{H}$, however, as the infinite-dimensional space of observables defined in (3.12). Given the sampling of a set of observables on a single ergodic trajectory, our computational goal is to get the sampling of the orthonormal basis functions for the subspace of $\mathcal{H}$ spanned by those observables. The next proposition shows that this can be achieved by applying SVD to a data matrix whose columns are ergodic sampling of those observables. Incidentally, such matrix is the transpose of a snapshot matrix!

Proposition 5 (Convergence of SVD to POD for ergodic systems)
Let $\mathcal{F} = [f_1,\ f_2,\ \ldots,\ f_n]$ be an ensemble of observables on the ergodic dynamical system in (3.1). *Assume $\mathcal{F}$ spans a $k-$dimensional subspace of $\mathcal{H}$ and let*

$$\mathcal{F} = \Psi \Sigma V^*,$$

be the POD of $\mathcal{F}$. Now consider the data matrix,

$$\tilde{F} = \begin{pmatrix} f_1(z_0) & f_2(z_0) & \ldots & f_n(z_0) \\ f_1 \circ T(z_0) & f_2 \circ T(z_0) & \ldots & f_n \circ T(z_0) \\ \vdots & \vdots & \ddots & \vdots \\ f_1 \circ T^{m-1}(z_0) & f_2 \circ T^{m-1}(z_0) & \ldots & f_n \circ T(z_0) \end{pmatrix} \tag{3.29}$$

and let

$$\frac{1}{\sqrt{m}} \tilde{F} \approx W S V^*$$

be the reduced SVD of $(1/\sqrt{m})\tilde{F}$.

Then, for almost every z_0, *as* $m \to \infty$,

(a) $s_j \to \sigma_j$ *for* $j = 1, 2, \ldots, k$ *and* $s_j \to 0$ *for* $j = k+1, \ldots, n$.

(b) $\tilde{v}_j \to v_j$ *for* $j = 1, 2, \ldots, k$.

(c) $\sqrt{m}w_j$ *converges to the sampling of* ψ_j *along the trajectory starting at* z_0 $j = 1, 2, \ldots, k$.

Proof: Consider the numerical Gramian matrix

$$\tilde{G} := (\frac{1}{\sqrt{m}}\tilde{F})^*(\frac{1}{\sqrt{m}}\tilde{F}) = \frac{1}{m}\tilde{F}^*\tilde{F}.$$

As shown in the proof of (3), the assumption of ergodicity implies the convergence of $\tilde{G}$ to the Gramian matrix G in (3.27) as $m \to \infty$. Now denote by $\lambda_j,\ j = 1, 2, \ldots, k$, the k eigenvalues of $\tilde{G}$ that converge to positive eigenvalues of G, and denote by $\lambda'_j,\ j = 1, \ldots, n-k$, the eigenvalues of $\tilde{G}$ that converge to zero. There exists m_0 such that for any $m > m_0$, all the singular values $s_j = \sqrt{\lambda_j}$ are larger than $s'_j = \sqrt{\lambda'_j}$ and therefore occupy the first k diagonal entries of S, which completes the proof of statement in (a).

The statement in (b) follows from the convergence of the normalized eigenvectors of $\tilde{G}$ associated with λ_j's to those of G. To show that (c) is true, we first construct the candidate functions by letting

$$\tilde{\psi}_j = \frac{1}{s_j}\mathcal{F}\tilde{v}_j,\ j = 1, 2, \ldots, k \tag{3.30}$$

We compute the entries of the orthogonal projection matrix P defined by $P_{i,j} =< \psi_i, \tilde{\psi}_j >$ and consider its limit as $m \to \infty$,

$$\lim_{m\to\infty} P_{i,j} = \lim_{m\to\infty}(\frac{1}{\sigma_i}\mathcal{F}v_i)^*(\frac{1}{s_j}\mathcal{F}\tilde{v}_j) = \frac{1}{\sigma_i}v_i^*\mathcal{F}^*\mathcal{F}\lim_{m\to\infty}\frac{1}{s_j}\tilde{v}_j = \frac{1}{\sigma_i^2}v_i^*Gv_j = \delta_{ij} \tag{3.31}$$

In the last equality, we have used (3.27). This calculation shows that $\tilde{\psi}_j$'s are weakly convergent to ψ_j's, and since they belong to the same finite-dimensional space, that implies strong convergence as well. Noting the definition of left singular vector

$$w_j = \frac{1}{\sqrt{m}s_j}\tilde{F}v_j, \tag{3.32}$$

it is easy to see that $\sqrt{m}w_j$ is the sampling of the candidate function $\tilde{\psi}_j$ along the trajectory starting at z_0. ■

3.3.1 Representation of chaotic dynamics in space of observables using Hankel matrix and SVD

Using the above results, we are able to construct an orthonormal basis on the state space from the time series of an ergodic system and give a new data-driven representation of chaotic dynamical systems. Recall that the columns of the Hankel matrix $\tilde{H}$ defined in (3.16) provides an ergodic sampling of the Krylov sequence of observables $\mathcal{F}_n = [f,\ Uf,\ ,U^n f]$ along a trajectory in the state space. Therefore by applying SVD to $\tilde{H}$, we can approximate an orthonormal basis for $\mathcal{F}_n$, and furthermore, represent the Koopman evolution of observable f in the form of principal coordinates.

We show an example of this approach using the well-known chaotic attractor of the Lorenz system [131]. This attractor is proven to have the mixing property which implies ergodicity [64]. The Lorenz system is given by

$$\begin{aligned}
\dot{z}_1 &= \sigma(z_2 - z_1),\\
\dot{z}_2 &= z_1(\rho - z_3) - z_2,\\
\dot{z}_3 &= z_1 z_2 - \beta z_3,
\end{aligned}$$

with $[z_1, z_2, z_3] \in \mathbb{R}^3$ and parameter values $\sigma = 10$, $\rho = 28$ and $\beta = 8/3$. First, we sample the value of observable $f(\mathbf{z}) = z_1$ every 0.01 seconds on a random trajectory, and then form a tall Hankel matrix as in (3.16) with $m = 10000$ and $n = 100$. Figure 3.1 shows the values of first six left singular vectors of the Hankel matrix, which approximate the basis functions ψ_j. The corresponding right singular vectors, shown in fig. 3.2, approximate the principal coordinates of $\mathcal{F}_n$. We make note that the computed basis functions and their associated singular values show little change with m for $m \geq 10000$.

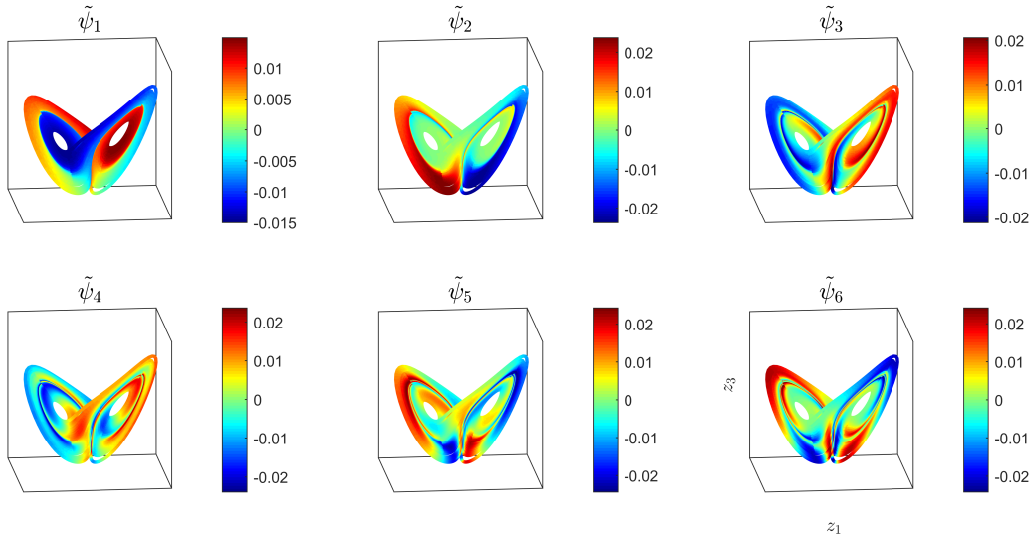

Figure 3.1: The first six POD basis functions of $[f,\ Uf, \ldots, U^i f, \ldots, U^{100} f]$ for chaotic Lorenz system. The observable is $f(z_1, z_2, z_3) = z_1$ and the Hankel matrix has the dimensions $m = 10000$ and $n = 100$.

In mixing attractors such as Lorenz, the only discrete eigenvalue for the Koopman operator is $\lambda = 1$, which is associated with eigenfunction that is constant almost everywhere on the attractor. In this case, the Koopman operator cannot have any invariant finite-dimensional subspace other than span of almost-everywhere constant functions. As a result, for a typical observable f, the Krylov sequence $\mathcal{F}_n$ is always $n + 1$-dimensional and growing with iterations of U. This observation shows that despite the fact that evolution of principal coordinates in fig. 3.2 is linear, there is no finite-dimensional linear

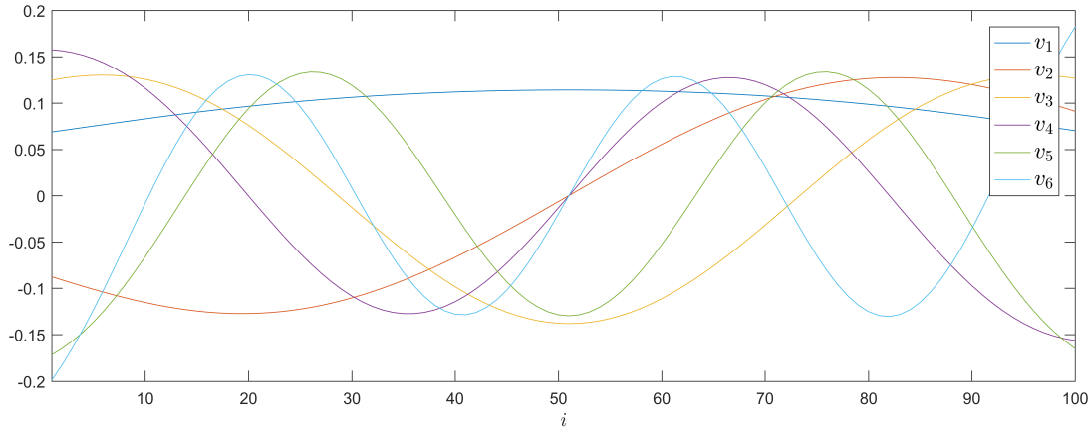

Figure 3.2: The principal coordinates for $[f, \quad Uf, \ldots, U^i f, \ldots, U^{100} f]$ with $f(z_1, z_2, z_3) = z_1$ in the basis shown in fig. 3.1.

system that can describe their evolution.

Proposition 5 offers a lifting of coordinates from state space to the space of observables which can be useful in the study of chaotic systems. Application of SVD to embedded time series in the form of Hankel matrix is a popular technique in the study of climate time series under the name of Singular Spectrum Analysis (SSA) [82]. This method is frequently used for pattern extraction and spectral filtering of short and noisy time series. In a more recent example, Brunton and co-workers [121] have introduced a new framework based on the SVD of Hankel data matrix to construct a linear representation of several chaotic systems including Lorenz attractor. They have discovered that the evolution of principal coordinates in some classes of chaotic systems - including Lorenz attractor - can be described via a low-dimensional linear system with intermittent forcing. By using such model, they were able to predict the highly nonlinear behavior of those systems over short time windows given the knowledge of the forcing. This suggests that replacing the state-space trajectory-based analysis with the evolution of coordinates in space of observable gives a more robust representation of the dynamics for analysis and control purposes.

3.4 Convergence of Exact Hankel-DMD and extension to multiple observables

In this section, we review the functional setting for Exact DMD and prove its convergence for ergodic systems using the assumption of invariant subspace. We then discuss using this method combined with Hankel matrices to compute the Koopman spectra from observations on single or multiple observables. The summary of the numerical algorithm with several examples will be given in the next section.

Let $\mathcal{F} =: [f_1, f_2, \ldots, f_n]$ denote a set of observables defined on the discrete dynamical system in (3.1). We make the assumption that $\mathcal{F}$ spans a $k-$dimensional subspace of $\mathcal{H}$, with $k \leq n$, which is invariant under the Koopman operator. Also denote by $U\mathcal{F} =: [Uf_1, Uf_2, \ldots, Uf_n]$ the image set of those observables under the action of the Koopman operator. We seek to realize the Koopman operator, restricted to this subspace, as a k-by-k matrix, given the knowledge of $\mathcal{F}$ and $U\mathcal{F}$.

Let

$$\mathcal{F} = \Psi \Sigma V^*. \tag{3.33}$$

be the POD of ensemble $\mathcal{F}$ with $\Psi = [\psi_1,\ \psi_2, \ldots,\ \psi_k]$ denoting its POD basis. Since $\mathcal{F}$ spans an invariant subspace, the functions in $U\mathcal{F}$ also belong to the same subspace and their principal coordinates can be obtained by orthonormal projection, i.e.,

$$\Omega = \Psi^* U\mathcal{F}. \tag{3.34}$$

The restriction of the Koopman operator to the invariant subspace is then given by matrix A which maps the columns of ΣV^* to the columns of Ω. The following lemma,

which summarizes some of the results in [33], gives the explicit form of matrix A and asserts its uniqueness under the prescribed condition on $\mathcal{F}$ and $U\mathcal{F}$.

Lemma 1 *Let $X_{k\times n}$ with $n \geq k$ be a matrix whose range is equal to $\mathbb{R}^k$. Let $Y_{k\times n}$ be another matrix which is linearly consistent with X, i.e., whenever $Xc = 0$ for $c \in \mathbb{R}^n$, then $Yc = 0$ as well. Then the Exact DMD operator $A := YX^\dagger$ is the unique matrix that satisfies $AX = Y$.*

Proof: First, we note that condition of Y being linearly consistent with X implies that A satisfies $AX = Y$ (theorem 2 in [33]). To see the uniqueness, let $\tilde{A}$ be another matrix which satisfies $\tilde{A}X = Y$. Now let $b \in \mathbb{R}^k$ be an arbitrary vector. Given that X spans $\mathbb{R}^k$, we can write $b = Xd$ for some $d \in \mathbb{R}^n$. Consequently,

$$\tilde{A}b = \tilde{A}Xd = Yd = AXd = Ab,$$

which means that action of A and $\tilde{A}$ on all elements of $\mathbb{R}^k$ is the same, therefore $\tilde{A} = A$. ■

Since $\mathcal{F}$ and $U\mathcal{F}$ are related through a linear operator, their principal coordinates with respect to the same orthogonal basis satisfy the condition of linear consistency, and the Koopman operator restricted to the invariant subspace is represented by the matrix

$$A = \Omega(\Sigma V^*)^\dagger = \Omega V \Sigma^{-1}, \tag{3.35}$$

where we have used the fact that Σ is diagonal and V is orthonormal. Let (w_j, λ_j), $j = 1, 2, \ldots, k$ denote the eigenvector-eigenvalue pairs of A. Then λ_j's are the Koopman eigenvalues and the associated Koopman eigenfunctions are given by

$$\phi_j = \Psi w_j, \quad j = 1, 2, \ldots, k. \tag{3.36}$$

Now we can assert the convergence of Exact DMD projected modes and eigenvalues to Koopman eigenfunctions and eigenvalues given the ergodic sampling of functions in $\mathcal{F}$ and $U\mathcal{F}$.

Proposition 6 (Convergence of Exact DMD for ergodic sampling)

Let $\mathcal{F} =: [f_1, f_2, \ldots, f_n]$ denote a set of observables that span a $k-$dimensional invariant subspace of the Koopman operator with $k \leq n$, defined on the dynamical system (3.1) *which is ergodic. Now consider the data matrices*

$$X = \begin{bmatrix} f_1(z_0) & f_2(z_0) & \ldots & f_n(z_0) \\ f_1 \circ T(z_0) & f_2 \circ T(z_0) & \ldots & f_n \circ T(z_0) \\ \vdots & \vdots & \ddots & \vdots \\ f_1 \circ T^{m-1}(z_0) & f_2 \circ T^{m-1}(z_0) & \ldots & f_n \circ T^{m-1}(z_0) \end{bmatrix}$$

and

$$Y = \begin{bmatrix} f_1 \circ T(z_0) & f_2 \circ T(z_0) & \ldots & f_n \circ T(z_0) \\ f_1 \circ T^2(z_0) & f_2 \circ T^2(z_0) & \ldots & f_n \circ T^2(z_0) \\ \vdots & \vdots & \ddots & \vdots \\ f_1 \circ T^m(z_0) & f_2 \circ T^m(z_0) & \ldots & f_n \circ T^m(z_0) \end{bmatrix}$$

Let λ_j and χ_j denote the dynamic eigenvalues and projected dynamic modes, respectively, obtained by applying Exact DMD (algorithm 5) to X and Y, using a k-dimensional truncation of SVD (i.e. with discarding the $n-k$ smallest singular values) in step 2.

Then, for almost every z_0, as $m \to \infty$:

(a) The dynamic eigenvalues converge to the Koopman eigenvalues.

(b) $\sqrt{m}\chi_j$ for $j = 1, 2, \ldots, k$ converge to the sampling of Koopman eigenfunctions along the trajectory starting at z_0.

Proof: We first show that as $m \to \infty$, the matrix $\tilde{A}$ constructed in the step 3 of the

algorithm 5 converges to the matrix A in (3.35). Let $X = WS\tilde{V}$ be the k-dimensional truncated SVD of X. It follows from the proof of proposition 5 that $S/\sqrt{m} \to \Sigma$ and $\tilde{V} \to V$ as $m \to \infty$. Then

$$\lim_{m\to\infty} \tilde{A} = \lim_{m\to\infty} W^*Y\tilde{V}S^{-1} = \left(\lim_{m\to\infty} \frac{1}{\sqrt{m}} W^*Y\right) V\Sigma^{-1}. \tag{3.37}$$

We need to show that $\tilde{\Omega} := 1/\sqrt{m}W^*Y$ converges to Ω (defined in (3.34)) as $m \to \infty$. To this end, recall the candidate functions in $\tilde{\Psi}$ defined in proof of proposition 5. We see that

$$\tilde{\Omega}_{i,j} = \frac{1}{\sqrt{m}} W_i^* Y_j = \frac{1}{m}\sum_{l=0}^{m-1} (\tilde{\psi}_i \circ T^l(z_0))^* (Uf_j \circ T^l(z_0)) := \frac{1}{m}\sum_{l=0}^{m-1} \tilde{\psi}_i^{l*} Uf_j^l \tag{3.38}$$

Since $\tilde{\psi}_i$'s are defined by linear combination of functions in $\mathcal{F}$, they lie in the span of Ψ. In fact, we have

$$\tilde{\psi}_i = \sum_{q=1}^{k} P_{i,q}\psi_q, \tag{3.39}$$

where $P_{i,q}$ denotes an entry of the orthogonal projection matrix P defined in the proof of proposition 5. The computation in (3.31) shows that as $m \to \infty$, we have $P_{i,q} \to 0$ if $q \neq i$ and $P_{i,i} \to 1$. Now we replace $\tilde{\psi}_i$ in (3.38) with its expansion in (3.39), while

considering the term

$$
\begin{aligned}
d_1 :&= \tilde{\Omega}_{i,j} - \frac{1}{m}\sum_{l=0}^{m-1}(\psi_i \circ T^l(z_0))^*(Uf_j \circ T^l(z_0)), \\
&:= \tilde{\Omega}_{i,j} - \frac{1}{m}\sum_{l=0}^{m-1}\psi_i^{l*}Uf_j^l, \\
&= \sum_{q=1}^{k} P_{i,q}\frac{1}{m}\sum_{l=0}^{m-1}\psi_q^{l*}Uf_j^l - \frac{1}{m}\sum_{l=0}^{m-1}\psi_i^{l*}Uf_j^l, \\
&= \sum_{q=1,\ q\neq i}^{k} P_{i,q}\frac{1}{m}\sum_{l=0}^{m-1}\psi_q^{l*}Uf_j^l + (P_{i,i}-1)\frac{1}{m}\sum_{l=0}^{m-1}\psi_i^{l*}Uf_j^l.
\end{aligned} \tag{3.40}
$$

The convergence of sums over l for $m \to \infty$ in the last line is given by (3.15). Combining that with the convergence of $P_{i,q}$'s, we can conclude that for every $\epsilon > 0$, there exists m_1 such that for any $m > m_1$, we have $|d_1| < \epsilon/2$. Now consider the term

$$
\begin{aligned}
d_2 &= \frac{1}{m}\sum_{l=0}^{m-1}\psi_i^{l*}Uf_j^l - \Omega_{i,j} \\
&= \frac{1}{m}\sum_{l=0}^{m-1}\psi_i^{l*}Uf_j^l - <\psi_i, Uf_j>.
\end{aligned} \tag{3.41}
$$

The convergence in (3.15) again implies that for every $\epsilon > 0$ there exists an m_2 such that for any $m > m_2$, we have $|d_2| < \epsilon/2$. Now it becomes clear that

$$
|\tilde{\Omega}_{i,j} - \Omega_{i,j}| = |d_1 + d_2| \leq |d_1| + |d_2| = \epsilon, \tag{3.42}
$$

for any $m > \max(m_1, m_2)$. This proves the convergence of $\tilde{\Omega}$ to Ω, which, by revisiting (3.37), means

$$
\lim_{m\to\infty} \tilde{A} = A. \tag{3.43}
$$

The eigenvalues of $\tilde{A}$ converge to the eigenvalues of A which are the Koopman eigenvalues. Let $\tilde{w}_j,\ j = 1, 2, \ldots, k$ denote the normalized eigenvectors of $\tilde{A}$, and define the candidate functions $\tilde{\phi}_j = \tilde{\Psi}\tilde{w}_j = \Psi P\tilde{w}_j$. Given that P converges to I, and $\tilde{w}_j$ converges to w_j as $m \to \infty$, it follows that $\tilde{\phi}_j$ strongly converge to the Koopman eigenfunctions $\phi_j = \Psi w_j$.

Now note that $\sqrt{m}\chi_j = \sqrt{m}U\tilde{w}_j$ is the sampling of candidate eigenfunction $\tilde{\phi}_j$ along the trajectory, and therefore it converges to the sampling of the Koopman eigenfunction ϕ_j as $m \to \infty$. ■

Recall that in section 3.2.1, we extended the application of companion-matrix Hankel-DMD to the basin of attraction of an ergodic set A by assuming the invariant measure on A is physical. An analogous extension of the above proposition can be stated using the same assumption:

Corollary 1 *Proposition 6 is also valid for $\nu-$almost every $z_0 \in \mathcal{B}$ (ν is the Lebesgue measure), where $\mathcal{B}$ is the basin of attraction for the ergodic attractor A of the dynamical system* (3.1)*, given that*

(i) The invariant measure on A is a physical measure,

(ii) $\mathcal{F}|_A$ spans a k-dimensional invaraint subspace of $\mathcal{H}$, and

(iii) $\mathcal{F}$ is continuous over $\mathcal{B}$.

Proof: The proof is similar to proposition 4. ■

Let us first consider the application of the above proposition using measurements on a single observable f. We can supplement those measurements using delay-embedding which is equivalent to setting $\mathcal{F} = [f,\ Uf, \ldots, U^{n-1}f]$. An ergodic sampling of $\mathcal{F}$ and $U\mathcal{F}$ is then given by data matrices

$$X = \tilde{H} \qquad Y = U\tilde{H}$$

where $\tilde{H}$ is the Hankel matrix defined in (3.16) and $U\tilde{H}$ is the same matrix but shifted one step forward in time. In such case, the Exact DMD reduces to the SVD-enhanced DMD as discussed in section 3.1.

In case of multiple observables, we can combine the delay-embedded measurements of the observables with each other. For example, let f and g be the only observables that could be measured on a dynamical system. Then, we let

$$\mathcal{F} = [f,\ Uf, \ldots,\ U^{l-1}f,\ g,\ Ug, \ldots,\ U^{q-1}g]$$

and data matrices would contain blocks of Hankel matrices, i.e.,

$$X = \begin{bmatrix} \tilde{H}_f & \tilde{H}_g \end{bmatrix}, \quad Y = \begin{bmatrix} U\tilde{H}_f & U\tilde{H}_g \end{bmatrix}, \tag{3.44}$$

The above proposition guarantees the convergence of the Exact DMD method if l and q are chosen large enough, e.g., $l, q > k + 1$ where k is the dimension of the invariant subspace containing f and g.

In numerical practice, however, the block Hankel matrices need some scaling. For instance assume $\|g\|_{\mathcal{H}} \ll \|f\|_{\mathcal{H}}$. The POD basis that corresponds to the measurements on g is associated with smaller singular values and might be discarded through a low-dimensional SVD truncation. To remedy this issue, we can use the fact that the ratio of the norm between observables in ergodic systems can be approximated from the measurements:

$$\alpha := \frac{\|f\|_{\mathcal{H}}}{\|g\|_{\mathcal{H}}} = \lim_{m\to\infty} \frac{\|\tilde{f}_m\|}{\|\tilde{g}_m\|}, \tag{3.45}$$

where $\tilde{f}_m$ and $\tilde{g}_m$ are the observation vectors defined in (3.14a). The scaled data matrices

in that case become

$$X = \begin{bmatrix} \tilde{H}_f & \alpha \tilde{H}_g \end{bmatrix}, \quad Y = \begin{bmatrix} U\tilde{H}_f & \alpha U \tilde{H}_g \end{bmatrix}. \tag{3.46}$$

3.5 Numerical application of Hankel-DMD method

Algorithm 6 summarizes the Hankel-DMD method for extracting the Koopman spectrum from single or multiple observables. This algorithm acts on Hankel matrices of the data in the form of

$$\tilde{H}^i = \begin{pmatrix} f_i(z_i) & f_i \circ T(z_i) & \dots & f_i \circ T^n(z_i) \\ f_i \circ T(z_i) & f_i \circ T^2(z_i) & \dots & f_i \circ T^{n+1}(z_i) \\ \vdots & \vdots & \ddots & \vdots \\ f_i \circ T^{m-1}(z_i) & f_i \circ T^m(z_i) & \dots & f_i \circ T^{m+n-1}(z_i) \end{pmatrix}, \quad i = 1, 2, \dots l, \tag{3.47}$$

and $U\tilde{H}^i$ which is the same matrix shifted forward in time. The data from observable f_i is collected from a trajectory starting at z_i which is in the basin of attraction of an ergodic attractor. Unlike the classical DMD algorithms in section 3.1, the number of modes obtained by this method depends on the length of the signal and the dimension of subspace in which the observable lies.

The rate of convergence for the Hankel-DMD can be established by considering the rate of convergence for ergodic averages. For periodic and quasi-periodic attractors, the error of approximating the inner products by (3.15) is generally bounded by $|c/m|$ for some $c \in \mathbb{R}$ [85]. For strongly mixing systems, the rate of convergence slows down to $c/\sqrt{m}$. However, for the general class of ergodic systems convergence rates cannot be established [132]. As we will see in this section, a few hundred samples would be enough to determine the Koopman frequencies of periodic systems with great accuracy, while a

few thousand would be enough for systems with a 2-torus attractor.

Remark 2 *In proving the convergence of the Hankel-DMD algorithm, we have assumed the explicit knowledge of the dimension of the invariant subspace (k) that contains the observable. In numerical practice, k can be found in the SVD step of the algorithm: proposition 5 showed that as $m \to \infty$, the number of singular values converging to positive values is equal to k. Therefore, we can approximate the invariant subspace by counting the number of singular values that don't seem to decay to zero. We can implement this assumption in algorithm 6 by hard-thresholding of the SVD in step 3, i.e., discarding the singular values that are smaller than a specified threshold. Such a threshold can be selected based on the desired numerical accuracy and considering the rate of convergence for ergodic averages which is discussed above. In case that the observable lies in an infinite-dimensional Koopman invariant subspace, we are going to assume that it lives in a finite-dimensional subspace down to a specific numerical accuracy. We can enforce this accuracy, again, by hard-thresholding the SVD. In the following examples, we have chosen the hard threshold of SVD to be 1e-10.*

3.5.1 Application to single observable: periodic and quasi-periodic cavity flow

In chapter 2, the lid-driven cavity flow was shown to exhibit periodic and quasi-periodic behavior at Reynolds numbers (Re) in the range of 10000-18000. The Koopman eigenvalues were computed by applying an adaptive combination of FFT and harmonic averaging to the discretized field of stream function, which is an observable with $\sim$ 4000 values. We use the Hankel-DMD method (algorithm 6) to extract the Koopman eigenvalues and eigenfunctions using a scalar valued observable (the kinetic energy) and compare our results with the following cases studied in chapter 2:

Algorithm 6 Hankel DMD

Consider the Hankel matrices $\tilde{H}^i$'s defined in (3.47).

1: Compute the scaling factors

$$\alpha_i = \frac{\|H^i_{n+1}\|}{\|H^1_{n+1}\|}, \quad i = 2, 3, \ldots, l,$$

where H^i_{n+1} is the last column of H^i.

2: Form the composite matrices

$$X = \begin{bmatrix} \tilde{H}_1 & \alpha_2 \tilde{H}_2 & \ldots & \alpha_l \tilde{H}_l \end{bmatrix}, \quad Y = \begin{bmatrix} U\tilde{H}_f & \alpha_2 U\tilde{H}_2 & \ldots & \alpha_l U\tilde{H}_l \end{bmatrix}.$$

3: Compute the truncated SVD of X (see remark 2):

$$X = WS\tilde{V}^*.$$

4: Form the matrix

$$\hat{A} = W^* Y \tilde{V} S^{-1}.$$

5: Let (λ_j, w_j), $j = 1, 2, \ldots, m$ be the eigenvalue-eigenvector pairs for $\hat{A}$. Then λ_j's approximate the Koopman eigenvalues.

6: The dynamic modes χ_j given by

$$\chi_j = W w_j, \quad j = 1, 2, \ldots, m.$$

approximate the Koopman eigenfunctions.

- At $Re = 13000$, the trajectory in the state space of the flow converges to a limit cycle with the basic frequency of $\omega_0 = 1.0042\ rad/sec$. The Koopman frequencies in the decomposition of analytic observables are multiples of the basic frequency, i.e., $k\omega_0,\ k = 0, 1, 2, \ldots$.

- At $Re = 16000$, the post-transient flow is quasi-periodic with two basic frequencies $\omega_1 = 0.9762\ rad/sec$ and $\omega_2 = 0.6089\ rad/sec$. In this case, the flow trajectory wraps around a 2-torus in the state space of the flow and the Koopman frequencies are integral multiples of ω_1 and ω_2, that is $\omega = \mathbf{k} \cdot (\omega_1, \omega_2),\ \mathbf{k} \in \mathbb{Z}^2$.

Let $\{E_i := E(t_0 + i\Delta t)\}$ denote the measurements on the kinetic energy of the flow at the time instants $t_0 + i\Delta t,\ i = 0, 1, 2, \ldots, s$. We first build the Hankel matrices of the kinetic energy observable,

$$\tilde{H}_E = \begin{pmatrix} E_0 & E_1 & \ldots & E_n \\ E_1 & E_2 & \ldots & E_{n+1} \\ E_2 & E_3 & \ldots & E_{n+2} \\ \vdots & \vdots & \ddots & \vdots \\ E_{m-1} & E_m & \ldots & E_{m+n-1} \end{pmatrix}, \quad U\tilde{H}_E = \begin{pmatrix} E_1 & E_2 & \ldots & E_{n+1} \\ E_2 & E_3 & \ldots & E_{n+2} \\ E_3 & E_4 & \ldots & E_{n+3} \\ \vdots & \vdots & \ddots & \vdots \\ E_m & E_{m+1} & \ldots & E_{m+n} \end{pmatrix}. \tag{3.48}$$

and then apply algorithm 6. Due to the discrete-time nature of the measurements, the eigenvalues computed by this method correspond to the discrete map obtained by strobing the original continuous-time dynamical system at intervals of length Δt. The eigenvalues $\lambda_j, j = 1, 2, \ldots$ computed via Hankel-DMD are related to the Koopman frequencies $\omega_j,\ j = 1, 2, \ldots$ through the following:

$$\lambda_j = e^{i\omega_j \Delta t}.$$

The computed dynamic modes $\tilde{\phi}_j$ approximate the value of the associated Koopman eigenfunctions along the first m points on the trajectory of the system.

For the periodic flow, we use 200 samples of the kinetic energy signal, with sampling interval of 0.1 *sec*, to form the above Hankel matrix with $m = n = 100$. In table table 3.1, we present frequencies obtained using the DMD-Hankel method, labeled by $\tilde{\omega}_k$, and compare with frequencies computed in chapter 2. We also compare the computed eigenfunctions with the theory for periodic and quasi-periodic attractors presented in [4]. In fact, the Koopman eigenfunctions for periodic and quasi-periodic attractors are the Fourier basis in the time-linear coordinates defined on the attractor. To make this notion precise, let $s \in [0, 2\pi)$ be the parametrization of the limit cycle given by $\dot{s} = \omega_0$. The Koopman eigenfunction associated with the Koopman frequency $\omega_k := k\omega_0$ is given by

$$\phi_k = e^{iks}, \quad k = 1, 2, 3, \ldots. \tag{3.49}$$

The real part of the Koopman eigenfunctions $\tilde{\phi}_k$ computed via the Hankel-DMD method are shown along the trajectory in figure fig. 3.3. The mean squared error in the approximation of the six eigenfunctions with largest vector energy is from an order of 10^{-5} or smaller (last column in the table table 3.1).

k	$\tilde{\omega}^k$	ω^k (ch. 2)	relative error	$var(\tilde{\phi}_k - \phi_k)$
0	0	0	0	$< 1e{-}10$
1	1.00421	1.00423	$1.59e{-}5$	$1.46e{-}6$
2	2.00843	2.00840	$1.56e{-}5$	$2.25e{-}5$
3	3.01264	3.01262	$4.94e{-}6$	$< 1.00e{-}10$
4	4.01685	4.01680	$1.55e{-}5$	$< 1.00e{-}10$
6	6.02528	6.02525	$5.03e{-}6$	$< 1.00e{-}10$

Table 3.1: The dominant Koopman frequencies and eigenfunctions for periodic cavity flow computed using observations on kinetic energy.

For the quasi-periodic cavity flow, a longer sequence of observations is required to

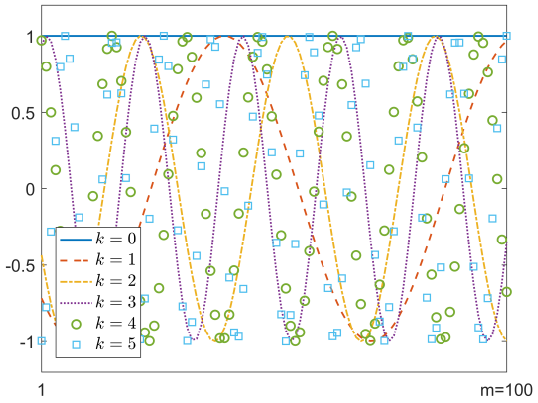

Figure 3.3: Real part of the computed Koopman eigenfunctions $\tilde{\phi}_k$ along the trajectory for periodic cavity flow at $Re = 13000$.

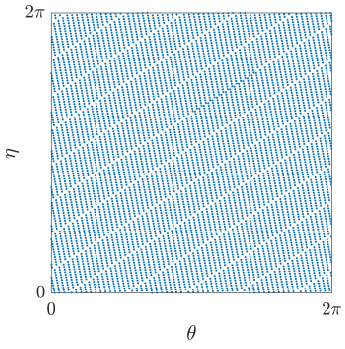

Figure 3.4: The trajectory of quasi-periodic flow on the parameterized torus defined in (3.50).

sufficiently sample the attractor which is a 2-torus. The eigenvalues shown in table 3.2 are computed using 6500 samples of the kinetic energy signal with sampling interval of 0.1 seconds, and by setting $m = 6000$ and $n = 500$. Once the basic frequency vector (ω_1, ω_2) is determined, the attractor can be parameterized by the time-linear coordinates $(\theta, \eta) \in [0, 2\pi)^2$ with

$$\begin{aligned} \theta &= \omega_1 t, \\ \eta &= \omega_2 t. \end{aligned} \tag{3.50}$$

The trajectory of the system on the parameterized torus is shown in fig. 3.4. The Koopman eigenfunctions associated with the frequency $\mathbf{k} \cdot (\omega_1, \omega_2)$ are given by

$$\phi_{\mathbf{k}} = e^{i\mathbf{k}\cdot(\theta,\eta)}, \qquad \mathbf{k} \in \mathbb{Z}^2. \tag{3.51}$$

The modes obtained by Hankel-DMD method provide an approximation of the Koopman eigenfunction along the trajectory (the dots in fig. 3.4) which could be extended to the whole torus through an interpolation process. Using this technique, we have plotted the Koopman eigenfunctions on the parameterized torus in fig. 3.5. The computed value of frequencies and eigenfunctions are in good agreement with the results in chapter 2 (Table 3.2).

3.5.2 Asymptotic phase for nonlinear oscillators

We show an application of corollary 1 by computing the asymptotic phase for trajectories of the Van der Pol oscillator. For definition of this problem, we closely follow the

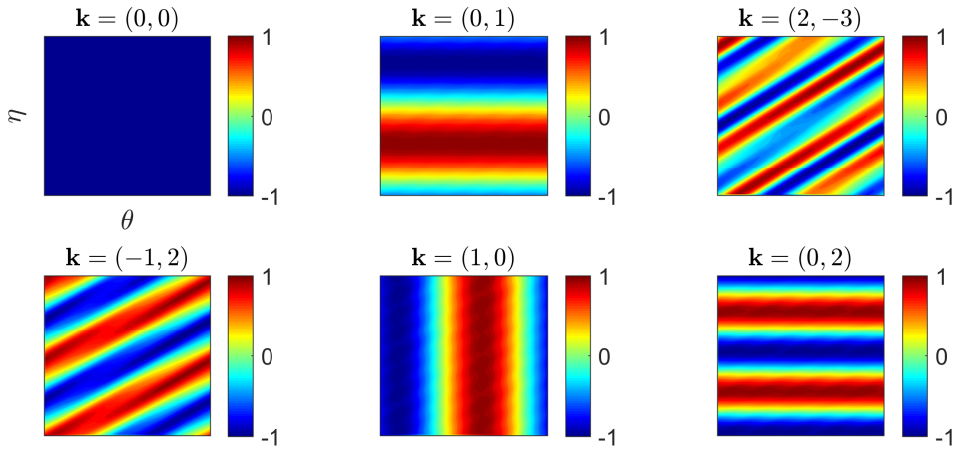

Figure 3.5: Real part of Koopman eigenfunctions $\tilde{\phi}_{\mathbf{k}}$ on the parameterized torus of quasi-periodic cavity flow at $Re = 16000$, computed using kinetic energy observable.

$\mathbf{k}$	$\tilde{\omega}_{\mathbf{k}}$	$\omega_{\mathbf{k}}$ (ch. 2)	relative error	$var(\tilde{\phi}_{\mathbf{k}} - \phi_{\mathbf{k}})$
$(0,0)$	0	0	0	$1.64e-9$
$(0,1)$	0.60891	0.60890	$1.58e{-}5$	$9.58e{-}4$
$(2,-3)$	0.12443	0.12598	$1.23e{-}2$	$1.69e{-}1$
$(-1,2)$	0.24159	0.24149	$3.96e{-}4$	$1.88e{-}2$
$(1,0)$	0.97624	0.97624	$3.68e{-}6$	$1.12e{-}3$
$(0,2)$	1.21781	1.21773	$6.40e{-}5$	$6.29e{-}3$

Table 3.2: The dominant Koopman frequencies and eigenfunctions for quasi-periodic cavity flow computed using observations on kinetic energy.

discussion in [133]. Consider the classical Van der Pol model

$$\dot{z}_1 = z_2, \;\; \dot{z}_2 = \mu(1 - z_1^2)z_2 - z_1. \quad \mathbf{z} := (z_1, z_2) \in \mathbb{R}^2. \tag{3.52}$$

For the parameter value $\mu = 0.3$, all the trajectories in the state space $\mathbb{R}^2$ converge to a limit cycle Γ with the basic frequency $\omega_0 \approx 0.995$. However, the trajectories converge to different orbits on the limit cycle and their asymptotic phase depends on the initial condition. The problem of determining the asymptotic phase associated with each initial condition in the state space is of great importance, e.g., in analysis and control of oscillator

networks that arise in biology (see e.g. [134, 135]). The Koopman eigenfunctions provide a natural answer for this problem; if ϕ_0 is the Koopman eigenfunction associated with ω_0, the initial conditions lying on the same level set of ϕ_0 converge to the same orbit and will have the same asymptotic phase [133]. The methodology developed in [133] is to compute the Koopman eigenfunction by taking the Fourier (or harmonic) average of a typical observable which requires prior knowledge of ω_0.

We use a slight variation of Hankel-DMD algorithm to compute the basic (Koopman) frequency of the limit cycle and the corresponding eigenfunction ϕ_0 in the same computation. Consider two trajectories of (3.52) starting at initial conditions $\mathbf{z}^1 = (4, 4)$ and $\mathbf{z}^2 = (0, 4)$. The observable that we use is $f(\mathbf{z}) = z_1 + z_2$, sampled at every 0.1 second over a time interval of 35 seconds ($m = 250$ and $n = 100$). Recall from remark 1 that we can use various vectors of ergodic sampling with Hankel-DMD algorithm to compute the spectrum and eigenfunctions of the Koopman operator. We populate the Hankel matrices with observation on both trajectories, such that the $l-$th column of the Hankel matrix, denoted by H^l, is given by

$$H^l = [f(\mathbf{z}^1),\ f(\mathbf{z}^2),\ f \circ T(\mathbf{z}^1),\ f \circ T(\mathbf{z}^2),\ \ldots,\ f \circ T^{m-1}(\mathbf{z}^1),\ f \circ T^{m-1}(\mathbf{z}^2)]^T.$$

Similarly,

$$UH^l = [f \circ T(\mathbf{z}^1),\ f \circ T(\mathbf{z}^2),\ f \circ T^2(\mathbf{z}^1),\ f \circ T^2(\mathbf{z}^2)\ \ldots,\ f \circ T^m(\mathbf{z}^1),\ f \circ T^m(\mathbf{z}^2)]^T.$$

The dynamic modes obtained by applying the Exact DMD to these Hankel matrices approximate the Koopman eigenfunctions along the two trajectories in the form of

$$\tilde{\phi}_0(\mathbf{z}^1, \mathbf{z}^2) := [\phi_0(\mathbf{z}^1),\ \phi_0(\mathbf{z}^2),\ \phi_0 \circ T(\mathbf{z}^1),\ \phi_0 \circ T(\mathbf{z}^2),\ \ldots,\ \phi_0 \circ T^{m-1}(\mathbf{z}^1),\ \phi_0 \circ T^{m-1}(\mathbf{z}^2)]^T.$$

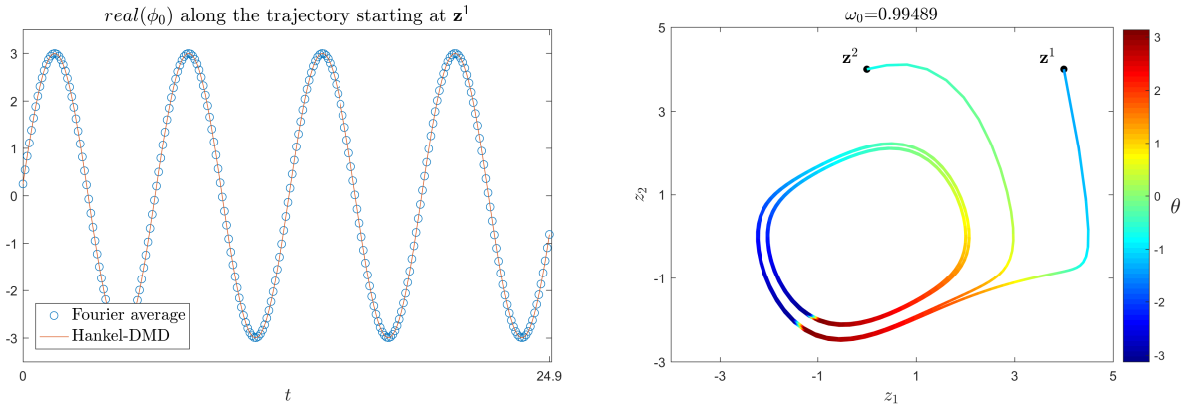

Figure 3.6: Asymptotic phase for Van der Pol oscillator: The Koopman eigenfunction associated with ω_0 along the trajectory starting at $\mathbf{z}^1$ (left), and asymptotic phase for points along two trajectories starting at $\mathbf{z}^1$ and $\mathbf{z}^2$ (right). The states with the same color converge to the same orbit on the limit cycle.

Figure 3.6 shows the agreement between Hankel-DMD and the Koopman eigenfunction obtained from Fourier averaging with known frequency [133]. The right panel shows $\theta = \angle\tilde{\phi}_0$ plotted as the color field along the trajectories which characterizes the asymptotic phase of each point on the trajectories.

3.5.3 Application to multiple observables: the quasi-periodic cavity flow

We show the application of algorithm 6 with multiple observables by revisiting the example of quasi-periodic flow in section 3.5.1. Let $\{G_i := G(t_0 + i\Delta t)\}$ be the set of measurements of the stream function at a point on the flow domain ($x = y = 0.3827$ in the domain defined in ch. 2). Also let E be the kinetic energy of the flow. We use the Hankel matrices of observations on G and E, by setting $m = 6000$ and $n = 500$ and form the data matrices

$$X = \begin{bmatrix} \tilde{H}_E & \tilde{\alpha}\tilde{H}_G \end{bmatrix}, \quad Y = \begin{bmatrix} U\tilde{H}_E & \tilde{\alpha}U\tilde{H}_G \end{bmatrix}. \tag{3.53}$$

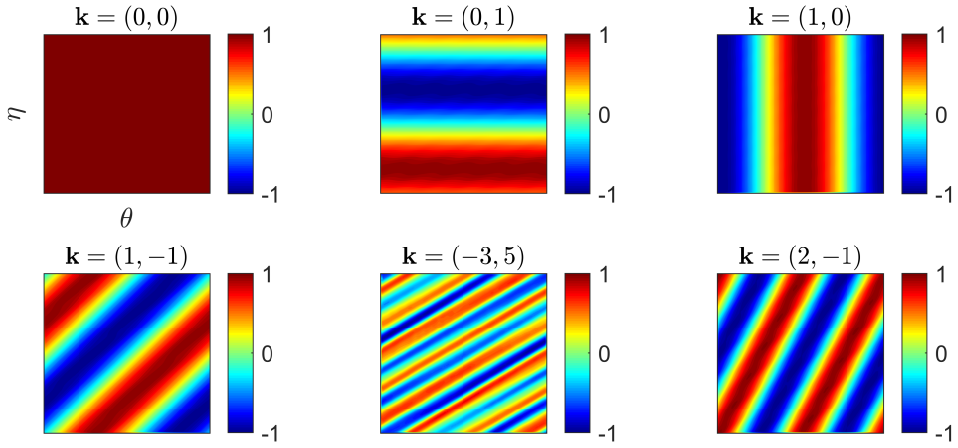

Figure 3.7: Real part of Koopman eigenfunctions $\tilde{\phi}_{\mathbf{k}}$ on the parameterized torus of quasi-periodic cavity flow at $Re = 16000$, computed using two observables: kinetic energy and stream function.

where we have approximated the scaling factor $\tilde{\alpha}$ by

$$\tilde{\alpha} = \frac{\|\tilde{G}_m\|}{\|\tilde{E}_m\|}. \tag{3.54}$$

Table 3.3 shows the error in approximation of Koopman frequencies and eigenvalues using two observables. The accuracy of computation is comparable to the single-observable computation in section 3.5.1. However, since we are supplementing the observation on E with measurements on G, we are able to capture new eigenfunctions, three of which are shown in the bottom row of fig. 3.7.

3.6 Summary

In this chapter, we have studied the convergence of DMD algorithms for systems with ergodic attractors. Our approach is based on approximation of the function projections using the vector projection in DMD, which is made possible by the Birkhoff's ergodic

$\mathbf{k}$	$\tilde{\omega}_{\mathbf{k}}$	$\omega_{\mathbf{k}}$ (ch. 2)	relative error	$var(\tilde{\phi}_{\mathbf{k}} - \phi_{\mathbf{k}})$
$(0,0)$	0	0	0	$6.76e-9$
$(0,1)$	0.60892	0.60890	$1.67e{-}5$	$9.38e{-}4$
$(1,0)$	0.97624	0.97624	$5.86e{-}6$	$5.90e{-}3$
$(1,-1)$	0.36732	0.36728	$1.13e{-}4$	$6.98e{-}4$
$(-3,5)$	0.11680	—	—	$1.34e{-}1$
$(2,-1)$	1.34353	1.34352	$3.68e{-}6$	$1.10e{-}2$

Table 3.3: Accuracy of the dominant Koopman frequencies and eigenfunctions for quasi-periodic cavity flow computed using Hankel-DMD method with two observables.

theorem. We showed a precise connection between SVD, which is frequently used in the DMD algorithms, and POD of ensemble of observables on the state space. By applying SVD to Hankel-embedded time series, we gave a new representation of chaotic dynamics on mixing attractors based on the evolution of coordinates in the space of observables. This representation turns out to be more beneficial for analysis and control purposes than the classic state-space trajectory-based representation. To compute the discrete Koopman operator for systems with ergodic attractors, we introduced the Hankel-DMD algorithm which is equivalent of applying the classic DMD algorithm to Hankel-type data matrices. This algorithm can compute Koopman spectrum using a small number of observables and trajectories in high-dimensional systems like fluid flows, with proven convergence properties.

In chapter 2, we discussed the application of Fourier spectral techniques for computation of Koopman spectrum. Unlike those methods, DMD-type algorithms are not yet capable of capturing continuous spectrum, however, they offer two advantageous feature: DMD is capable of capturing dissipative eigenvalues. In fact, Hankel-DMD method shows promise for computing the such eigenvalues and we will discuss it in future articles. And more importantly, DMD yields an approximation of the Koopman operator in the form of a linear system which can be used for control. A couple of promising studies have already appeared in this direction [46, 47].

Chapter 4

Mixing in the lid-driven cavity flow

Mixing is an important aspect of many natural and industrial flows. Characterizing the vertical mixing in the ocean and atmosphere, for example, constitutes the main challenge in modeling the earth climate [136, 137], while understanding the horizontal mixing on the ocean surface helps us predict the movement of pollution, which could lead to more effective strategies for containment [138]. Other examples from natural flows include the mixing in the earth mantle which led to formation of oceanic islands with nonuniform geochemistry [139], blood flow mixing in relation to health and disease [140] and the role of mixing in shaping the ecological equilibrium in oceanic environment [141]. For the industrial flows, on the other hand, we often try to manipulate mixing, e.g., design devices that efficiently mix the fluids given the constraints by the specific application [142, 143]. All such efforts are based on our understanding of many factors that play into mixing like the flow dynamics, device geometry, initial configuration of the mixing fluids, etc..

Study of mixing in real-world problems is difficult. Most of rigorous analysis in this field comes from theory of chaotic advection, which treats the fluid flow as a dynamical system with trajectories that describe the paths of objects. This theory has made an

enormous impact on how we view the transport of material in flows which are steady or time-periodic, but it offers significantly less insight for flows which are aperiodic in time. On the other hand, most of the natural flows and many industrial flows show aperiodic time dependence. As a result, a large number of techniques have been developed to fill the gap between the knowledge of mixing in periodic flows and the aperiodic flows that appear in practice. Most of these techniques strive to characterize the mixing in a given aperiodic flow by detecting the coherent structures and visualizing the flow in a way that is most informative about the collective behavior of Lagrangian trajectories.

Here, we study mixing from a different perspective, namely, we consider how the mixing portrait is changed while the temporal regime of a bounded flow - the lid-driven cavity flow - changes from steady to aperiodic. This change occurs naturally due to a sequence of bifurcations in the flow dynamics with the increase of the Reynolds number. We also use KMD and POD to characterize the number of modes for each flow that play a significant role in mixing.

We discuss the mixing as the advection of passive tracers, and therefore, ignore the inertial and finite-size effects for particles and molecular diffusion for scalar fields. In other words, we focus on the limit of infinite Peclet number and zero Stokes number in transport of materials with the flow. In order to visualize the mixing in such setting, we use the so-called *hypergraphs*, which are maps that partition the flow domain based on the Lagrangian deformation of the fluid blobs.

An interesting observation from chapter 2 is that vorticity distribution in the mean flow is almost unform in the center. For steady flows, this observation is the result of the Prandtl-Batchelor theory, but here, we extend this to periodic flows and discuss its consequences for mixing. We will also use projection models (based on POD and KMD) to compute the "dimensionality of mixing", that is, the order of Koopman-POD reduced models that are required to emulate the actual mixing in cavity flow.

In section 4.1, we review the literature related to the dynamical-systems analysis of mixing, and also the mixing of the cavity flow. In section 4.2, we explain how we compute and utilize hypergraphs to interpret mixing. In section 4.3, we define KMD+POD projection models. In section 4.4, we present the results of our analysis. We give the proof of the Prandtl-Batchelor theory for periodic flows in section 4.6.

4.1 Related work

4.1.1 Dynamical-systems methods for study of mixing

The foremost contributions to study of mixing in incompressible flows come from the paradigm of *chaotic advection*. This paradigm was initiated by the seminal paper of Aref [144] which showed that chaotic mixing can be achieved in time-periodic flows - contrary to the long-standing belief that chaotic mixing requires chaotic flow field. Using the example of blinking vortex flow, he showed the connection between the concept of non-integrability in dynamical systems theory and the flow mixing property. The pioneering textbook by Ottino [145] further emphasized the connection between geometry of mixing in flows and the dynamical systems theory. It also highlighted the role of stretching and folding in the mixing process, and presented a systematic study of many steady and periodic flows. Another breakthrough in the study of periodic flows was the invention of *lobe dynamics* [146, 147]. In this approach, the spatial domain of a time-periodic flow is partitioned into different regions separated by the invariant manifolds of the flow Poincaré map. The flux of material between those regions is then quantified by the interchange of the so-called lobes at the intersection of those orbits. Further contributions to the field of chaotic advection are too many to enumerate here, and we refer the reader to [148] for a more detailed review of this field.

The majority of the natural and industrial flows exhibit aperiodic time dependence. Unfortunately, chaotic advection theory is incapable of answering the questions that arise in the context of such flows. This is mainly due to the fact that geometric notions in this theory (like invariant manifolds and Poincaré maps), are not well-defined for aperiodic flows or have no significance for observations over finite time. The methodologies developed to address this shortcoming, either try to extend the modern techniques of dynamical systems theory to finite-time and aperiodic flows, or give a new formulation of the concepts related to mixing. In the following, we review some of those methodologies that have gained popularity in the last two decades.

A notable contribution to study of mixing in finite time is the theory of Lagrangian Coherent Structures (LCS). This theory aims to find the material surfaces with maximal attracting, repelling or shear impact on the nearby fluid elements. The LCS defined as such affect the mixing by forming transport barriers or vortical structures that travel with the ambient flow [149]. The hyperbolic LCS are finite-time analogues of invariant manifolds from classical dynamical systems, and serve as boundaries of regions in the flow that show different dynamical behavior [150]. The elliptic (or shear) LCS, on the other hand, are a generalization of structures known as Kolmogorov-Arnold-Moser tori in dynamical systems, and denote the vortical coherent sets [151]. The location of LCS was initially linked to the maxima in the field of the finite-time Lyapunov exponent [152], but recently they have been reformulated based on variational principles (see e.g. [153]).

Another approach toward study of mixing is built on purely topological aspects of 2D flows in bounded domains [154]. In this approach, the space-time trajectories of a set of tracers within the flow, are abstractly represented by algebraic objects known as *braids*. The degree of tangling in the braids is proportional to the topological entropy of the flow, which is, the maximum rate of stretching for material loops within the flow. This entropy indicates the complexity of motion and the strength of mixing. Using

the symbolic representation of the braids, one is able to compute lower bounds on the topological entropy to analyze the mixing performance of stirring protocols or design new efficient mixers [155, 156]. The braid analysis has also been deployed to compute the invariant sets [157] and quantify the complexity of the motion over finite time using spatially sparse measurements [158].

The theory of finite-time coherent sets offers another framework for characterization of mixing in aperiodic flows. This theory was initiated by introduction of almost-invariant sets, which are defined as sets that exhibit minimal leakage of trajectories in autonomous dynamical systems [159, 160]. Later on, the notion of almost-invariant sets was extended to that of (finite-time) coherent sets, i.e., the sets traveling with the flow that have minimal mixing with their surrounding, and used in the study of finite-time transport [161, 162]. This framework is based on approximating the transfer operator of dynamical systems which pushes forward the densities in the state space according to the dynamics. In an equivalent formulation, a coherent set is defined as a set whose perimeter-to-volume ratio remains small while traveling with the flow, and therefore allows minimal dispersion across its boundary [163].

The dynamical-system analysis of the flow domain could be alternatively pursued from a statistical viewpoint. The invariant sets in the spatial extent of a steady or periodic incompressible flow coincide with the level sets of infinite-time averages along Lagrangian trajectories [164]. This allows a feasible detection of invariant subdomains in flows with simple time dependence in numerical and experimental settings [165, 85, 166]. Using this theory, one can also build a low-dimensional representation of Lagrangian dynamics, track the changes in the structure of invariant subdomains, and easily detect the qualitative changes in the mixing behavior [167]. This technique was applied to aperiodic flows in [168], and the mathematical formulation was extended to finite-time observations in [169]. A descendant of this approach is the theory of mesohyperbolicity which partitions the flow

domain into regions with hyperbolic or elliptic behavior over finite time. This partition reveals the the regions which show chaotic-like mixing over finite time and separates them from the stagnating regions [170]. The theory and application of mesohyperbolicity is recently extended to 3D flows in [171].

4.1.2 Previous studies on mixing in lid-driven cavity flow

The mixing in the lid-driven cavity has been explored from many aspects and under different settings. This flow requires a relatively simple computational or experimental setup, and it represents a simplified model of geophysical flows driven by shear [70, 71], or a common type of mixers in polymer engineering known as single-screw extruder [72]. Most of the previous studies have focused on low-Reynolds cavity flows with time-dependent lid motion, and investigated the effect of different factors like lid motion frequency and cavity geometry on enhancement of mixing.

In the steady lid-driven cavity flow at low Reynolds, mixing is generally poor since the tracers are confined to move along the streamlines [145]. The experiments in [172] and [173] showed that mixing is greatly improved if periodic lid motion is used to generate periodic flow. In that case, the motion of tracers inside the cavity is comprised of both periodic and chaotic trajectories. The chaotic trajectories make the well-mixed regions while the tracers with periodic motion form the so-called *periodic islands*. These islands prevent full mixing because the fluid blobs inside them remain coherent and trapped, and do not spread over the cavity. The experiments showed that size of these islands are dependent on the forcing frequency, and therefore it was understood that there are optimal frequencies, at which, the islands are virtually nonexistent, and overall mixing can be achieved. [174] and [175] identified such frequency ranges by studying the linear stability of the periodic orbits that correspond to those islands. Their results showed

good agreement with simulation and previous experiments, and motivated further studies on detection of periodic orbits inside the periodic cavity flow and their role in mixing [176, 177, 178, 179, 180].

The notion of aperiodic mixing is explored in few studies regarding the lid-driven cavity flow. [181] and [182] proposed a non-random aperiodic protocol for the lid motion to enhance mixing. The underlying idea in these work is to manipulate the symmetries in the flow to break up the periodic islands. The numerical studies in [183] also showed that the aperiodic lid motion leads to stronger and more uniform mixing in the cavity flow.

There are also other studies that investigated the mixing in lid-driven cavity flow with different geometries [182, 184, 185], or under the effect of flow stratification [70], multi-phase flow configuration [186, 187], and motion of freely moving solid bodies within the flow [188, 189, 190].

4.2 Visualizing mixing with hypergraphs

In this work, we use hypergraphs as a tool to detect regions of different mixing behavior in the lid-driven cavity flow. The use of hypergraphs in the study of mixing was first introduced by [170], with a successful prediction of oil slick movement in the Deepwater Horizon oil spill. In this section, we explain how hypergraphs can be computed, and utilized to examine mixing for 2D incompressible flows. The reader is referred to [171] for a more detailed discussion of hypergraphs and extension to 3D flows.

The hypergraphs are visualizations of a scalar field known as *mesohyperbolicity* which partitions the flow domain according to the type of Lagrangian deformation. The field of mesohyperbolicity is defined as follows: Consider the trajectory of a passive tracer passing through $\mathbf{x}$ at time t_0. We denote by $\mathbf{u}^{*t_0+T}_{t_0}(\mathbf{x})$, the time-averaged Lagrangian

velocity of the tracer over the time interval $[t_0, t_0 + T]$. The mesohyperbolicity field at the location $\mathbf{x}$ and time T is given by

$$M(\mathbf{x}, T) \equiv \det \left| \nabla_{\mathbf{x}} \mathbf{u}^{*t_0+T}_{t_0}(\mathbf{x}) \right| . \tag{4.1}$$

This field uniquely determines the type of Lagrangian fluid deformation in the neighborhood of the tracer over the time interval $[t_0, t_0 + T]$:

1. In the regions where $M < 0$, the fluid element centered at the tracer is stretched in one direction and contracted in the other while moving. This deformation is similar to behavior of trajectories in the vicinity of a hyperbolic fixed point in a plane, hence called *mesohyperbolic*.

2. When $0 \leq M \leq 4/T^2$, the fluid elements undergo rotation while traveling with the tracer. We call this behavior *mesoelliptic*.

3. The regions with $M > 4/T^2$ show the combination of the above deformations, i.e., the material element rotates while it is stretched in one direction and contracted in the other. This type of deformation is called *mesohelical*.

In the hypergraphs presented in this thesis, the mesohyperbolic behavior is marked by blue, mesoelliptic by green, and mesohelical by red. A typical hypergraph for the periodic cavity flow is shown in fig. 4.1 (left panel). A comparison with the Poincaré map of the same flow (right panel) shows how hypergraphs can be used to determine the well-mixed regions in the flow: The islands of periodic motion which correspond to poorly-mixed regions stand out as concentric bands of alternating colors. The well-mixed regions, however, are revealed in hypergraphs as areas with a fine-grained mixture of the mesohyperbolic and mesohelical deformation (red and blue).

The work in [170] extended the application of hypergarphs to study of finite-time and aperiodic mixing in 2D incompressible flows. Over finite time intervals, the regions of

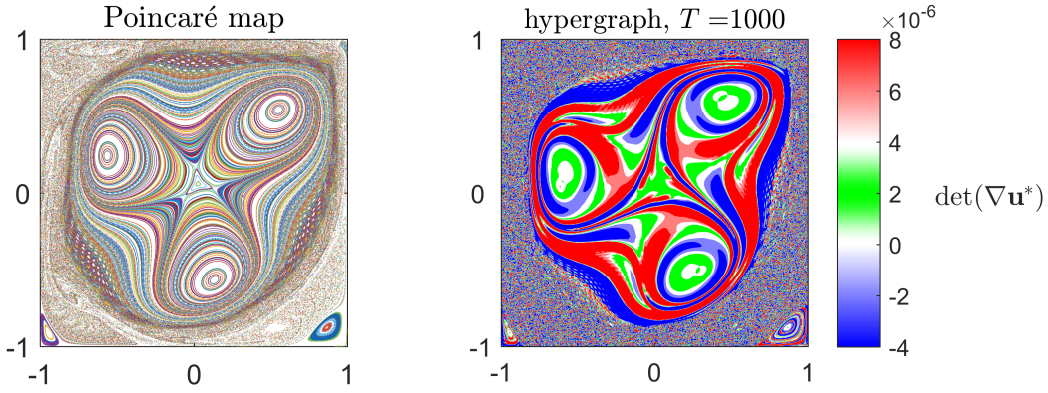

Figure 4.1: (a) Poincaré map of periodic cavity flow at $Re = 13000$, computed using 300 random trajectories over 2000 time periods. (b) Hypergraph of the same flow over 1000 sec, computed on a grid of 300×300 initial conditions. Blue, red and green colors correspond to mesohyperbolic, mesohelical and mesoelliptic behavior respectively. The (chaotic) mixing zones stand out in the hypergraph as regions with fine mixtures of red and blue.

substantial mixing stand out in hypergraphs as areas with a fine-grained combination of red and blue - similar to periodic flows, because those regions host an extensive amount of stretching and folding of the material elements, which is closely associated with (infinite-time) genuine chaotic motion. On the other hand, the poorly-mixed regions divide into two subgroups: regions that are consistently meso-elliptic and therefore show rotation and stagnation zones, and regions with a dominant type of either meso-hyperbolic (blue) or meso-elliptic (red) which denote likely passages for tracer motion in the form of coherent blobs.

4.2.1 Computation and visualization of hypergraphs

Consider the trajectory of a passive tracer starting at $\mathbf{x}$ at time t_0. The position of this tracer at time $t > t_0$ is given by the flow map $\mathbf{F}(\mathbf{x}, t)$, which solves the ordinary

differential equation (ODE)

$$\dot{\mathbf{F}}(\mathbf{x},t) = \mathbf{u}(\mathbf{F}(\mathbf{x},t),t), \quad t \in [t_0, t_0+T], \quad \mathbf{F}(\mathbf{x},t_0) = \mathbf{x}, \tag{4.2}$$

where $\mathbf{u}$ denotes the velocity field. The average Lagrangian velocity of the tracer is computed from the flow map,

$$\mathbf{u}^{*t_0+T}_{t_0}(\mathbf{x}) = \frac{1}{T}(\mathbf{F}(\mathbf{x},t_0+T) - \mathbf{x}). \tag{4.3}$$

Computing the mesohyperbolicity field defined in (4.1) requires two steps of computation. The first step is to solve the above ODE. This is often achieved by direct integration of (4.8) for a grid of passive tracers initially distributed over the flow domain. The second step is to evaluate the gradient of lagrangian velocity. There are two approaches to accomplish this step. In the first approach, the gradient is computed via finite difference on the initial grid of tracers. An auxiliary grid collocated around points of the initial grid can be used to improve the numerical efficiency (see e.g. the computation of the flow map gradient in [153]). The major disadvantage of this method is that in hyperbolic regions, the tracer paths diverge exponentially and the distance between them might become too large for implementation of the finite difference method. In that case, the primary grid points should be equipped with a new auxiliary grid to carry on the computation.

In the second approach, which we take here, the use of finite difference is avoided by integrating the linear differential equation for the flow map gradient [191],

$$\frac{\mathrm{d}}{\mathrm{d}t}\nabla\mathbf{F}(\mathbf{x},t) = \nabla\mathbf{u}(\mathbf{F}(\mathbf{x},t),t)\cdot\nabla\mathbf{F}(\mathbf{x},t), \quad t \in [t_0, t_0+T], \quad \nabla\mathbf{F}(\mathbf{x},t_0) = I, \tag{4.4}$$

with I being the identity matrix. This ODE is solved along with (4.8) for the same set

of tracers. The Lagrangian velocity gradient is given by

$$\nabla \mathbf{u}^{*t_0+T}_{t_0}(\mathbf{x}) = \frac{1}{T}(\nabla \mathbf{F}(\mathbf{x}, t_0 + T) - I). \tag{4.5}$$

This approach requires nearly the same computational effort as the finite difference approach, given that the instantaneous field of $\nabla \mathbf{u}$ is readily available. We used the standard 4th-order Runge-Kutta method to integrate equations (4.8) and (4.4). In doing so, the velocity field obtained by numerical solution of Navier-Stokes equations was interpolated using the spline method in space, and the linear method in time. In the hypergraphs plotted in this paper, the mesohyperbolicity field, $M(\mathbf{x}) := \det|\nabla \mathbf{u}^{*t_0+T}_{t_0}(\mathbf{x})|$, is plotted and partitioned into the mesohyperbolic ($M < 0$), mesoelliptic ($0 < M < 4/T^2$), and mesohelical ($M > 4/T^2$) regions, which are respectively marked by blue, green and red colors. For more readability, the value of mesohyperbolicity field in hypergraphs is cut off for $M > 8/T^2$ and $M < -4/T^2$.

4.3 KMD+POD projection models

In chapter 2, we used the Koopman spectral projections to study the efficiency of Koopman modes in low-dimensional presentation of the flow dynamics. As discussed in section 2.1, the chaotic component of the post-transient flow is a realization of a stationary stochastic process, and therefore it is most beneficial to use statistical tools like POD to obtain a decomposition of such process. POD, also known as principal component analysis, is a linear decomposition of the flow field into spatially orthogonal modes with uncorrelated time-dependent coefficients. Here we use POD to complement

KMD, and construct a modal decomposition of the full flow in the form of

$$\mathbf{u}(\mathbf{x},t) = \sum_{\mathbf{J}\in\mathbb{Z}^2} \mathbf{u}_{\mathbf{J}}(\mathbf{x}) e^{\mathbf{J}\cdot\boldsymbol{\Omega}t} + \sum_k a_k(t)\boldsymbol{\phi}_k(\mathbf{x}). \tag{4.6}$$

The first sum is the KMD of the quasi-periodic component of the flow (described in section 2.1), and the second sum is the POD of the chaotic component. The time-dependent coefficient a_k is the *principal coordinate* associated with the POD mode $\boldsymbol{\phi}_k$. Under the assumption of ergodicity for post-transient flows, the POD modes are unique and independent of the initial condition in the limit of infinitely long observations.

A KMD+POD projected model of order $m+n$ is a truncation of the above decomposition containing m Koopman modes and n POD modes, i.e.,

$$\mathbf{u}_{m,n}(\mathbf{x},t) = \sum_{j=1}^{m} \mathbf{u}_j(\mathbf{x}) e^{\omega_j t} + \sum_{k=1}^{n} a_k(t)\boldsymbol{\phi}_k(\mathbf{x}). \tag{4.7}$$

We can use such models to characterize the effect of Koopman or POD modes on the flow mixing. For example the effect of the $i-$th Koopman mode can be realized as the difference between the mixing in $\mathbf{u}_{i-1,0}$ and $\mathbf{u}_{i,0}$. In particular, we will be interested to the number of modes that play a role in mixing of each flow regime.

4.4 Mixing in the cavity flow

The hypergraphs in fig. 4.2 show the mixing portrait of cavity flow over different flow regimes and time intervals. In the periodic flow ($Re = 13000$), the central region of cavity is occupied with islands of periodic motion, whereas its surrounding area next to the walls (except two little eddies in the bottom corners) seems to be fully mixed. In the quasi-periodic flow ($Re = 16000$) the mixing area grows inward and fills all the

cavity domain except a mesoelliptic region in the center. The behavior of the flow with the mixed spectra ($Re = 20000$) is similar to quasi-periodic mixing, that is, the mixing region emerges from the walls and expands inward, but we see that the coherent island in the center is larger than the quasi-periodic flow. This observation implies that mixing in the flow with mixed spectra (depending on the initial configuration of material) could be slower than quasi-periodic mixing. For a fully chaotic flow ($Re = 30000$), full mixing in the center can be achieved, however, as shown in the figure, there might be islands of coherent motion that persist for long intervals.

The above observations are somewhat contrary to the physical intuition from fluid mechanics. We would expect that mixing would improve with the increase of Reynolds number and transition to chaos, however, the sequence in fig. 4.2 suggests that this enhancement is non-monotonic (the island in the center is larger for $Re = 20000$ than $Re = 16000$). This phenomena can be explained as follows: as the flow transitions from quasi-periodic to chaotic, the kinetic energy moves from a few dozens of Koopman modes to chaotic fluctuations with broadband spectra and small spatial scales. This transfer of energy enhances the local mixing, but it is not as efficient in bulk stretching and folding of the material as the quasi-periodic motion, and as a result the bulk mixing may decrease. As the Reynolds number is further increased, the chaotic fluctuations become stronger and therefore mixing still increases.

The mixing of incompressible flows is often studied using volume-preserving maps from dynamical systems [147]. The work in [192] have made a similar observation on a class of 2D maps (called standard map) which undergo a range of dynamic behavior as the perturbation parameter is varied. At low parameter values, the state space is foliated with periodic and quasi-periodic orbit (similar to the laminae in a laminar flow). As the parameter value increases, most of the regular orbits are destroyed and replaced with chaotic motion (i.e. exponential mixing), but at the same time, some islands of

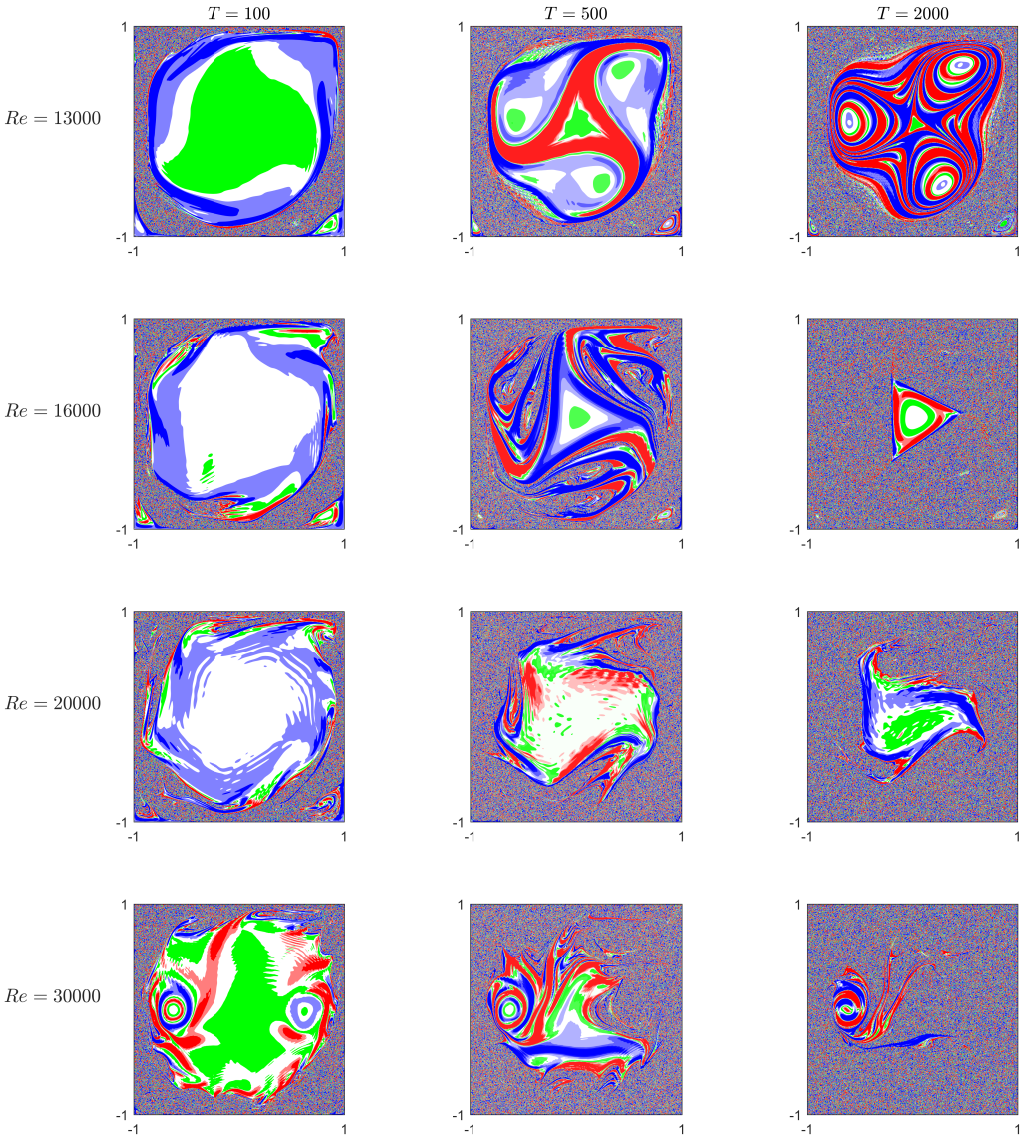

Figure 4.2: Hypergraphs of cavity flow for different Reynolds and over different time intervals.

periodic motion are formed in the state space. As a result, there will be an initial decline of mixing before the perturbation parameter passes a threshold over which there are no islands and full mixing is achieved.

Another outstanding feature of cavity flow is that the mixing in the center of the cavity is much slower than mixing in the areas next to the walls. In the next section, we connect this observation to the distribution of vorticity in the mean flow and analysis of periodically perturbed 2D dynamical systems.

4.4.1 Mixing in periodic flow and Prandtl-Batchelor theory

An important finding of all the previous studies on time-periodic bounded flows is that the time period of the flow is the most critical parameter that affects the mixing. The experiments by Ottino *et al.* on lid-driven cavity flow, for example, have shown that the period of the flow governs the existence and size of the periodic islands, and therefore determines whether partial or complete mixing is achieved [172, 173]. The work in [174] studied the influence of the flow period on the stability of periodic orbits of tracer motion and detected different ranges of flow period for which full mixing occurs. In some of those works, the relationship between flow period and the typical tracer circulation period in the steady flow was mentioned, and even exploited to enhance mixing. Another example is the numerical and experimental study of a 3D laminar vortex flow in [193], which showed that uniform mixing takes place when the flow period is close to the typical tracer circulation times. Another interesting example is the topological study of mixing in lid-driven cavity flow by [180]. The proposed periodic lid motion achieves topological chaos by making a delicate match between circulation period of certain tracers and the period of the lid motion.

Here, we use the relationship between the time period of the flow and circulation

period of tracers in the *mean flow* to show why mixing in the center of the cavity is poor. As suggested by the Koopman spectrum of fig. 2.3, the periodic flow can be considered as a mean flow (i.e. the first Koopman mode) which is perturbed by a low-energy time-periodic velocity field (i.e. sum of Koopman oscillatory modes). Therefore, we consider the circulation periods of the mean flow and study the effect of the time-periodic perturbation on the trajectory of the tracers. A critical feature of the mean flow, that is persistent over the considered range of Reynolds number, is the relatively-uniform distribution of vorticity in the central region (fig. 2.5). The occurrence of this so-called inviscid core in *steady* flows at high Reynolds numbers is anticipated by the Prandtl-Batchelor theory. This theory states that in regions of the flow with closed streamlines and small viscous forces, the vorticity will be constant [194, 195]. No analogue of this theory exists for general unsteady flows. Inspired by our numerical results, however, we have explored the applicability of this theory to periodic and quasi-periodic flows in the Appendix 4.6. Particularly, we show that the conclusion of the Prandtl-Batchelor theory holds for the mean vorticity field of time-periodic flows.

The constant vorticity in the core of the mean flow leads to a uniform distribution of circulation periods for tracers (blue curve in figure 4.3). In contrast, the circulation periods of the smaller vortices vary largely over smaller length scales (red, yellow and cyan curves). Given these observations, we can use the theory of perturbations for 2D Hamiltonian systems to predict the qualitative motion of tracers when the mean flow is subjected to a small-energy time-periodic perturbations. The classical techniques for such predictions, e.g., Melnikov method and Kolmogorv-Arnold-Moser (KAM) theory, are aimed to predict wether any chaotic trajectories appear as the perturbations are introduced to the Hamiltonian system [1]. The essence of these techniques is to detect the *resonances* between the circulating tracers of the mean flow and the perturbing flow field, which leads to chaos, e.g., through formation of homoclinic tangles. Contrasting the

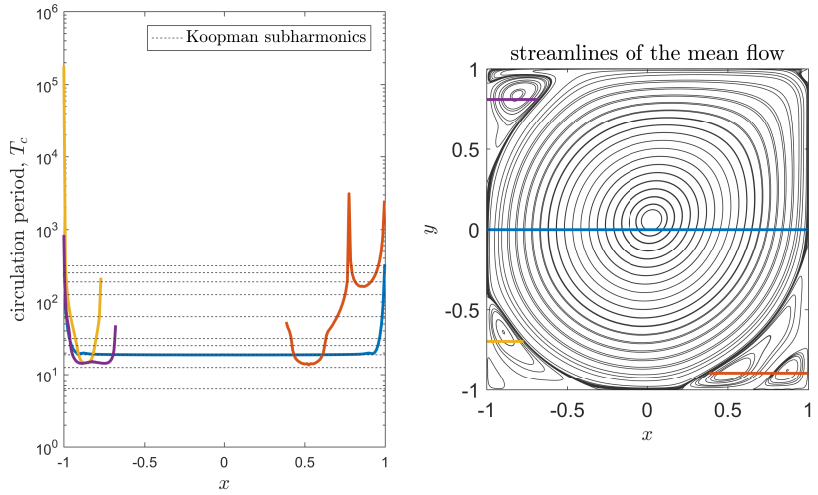

Figure 4.3: Resonance analysis for mixing at $Re = 13000$: Time period of tracer circulation in different zones of the mean flow (left); blue curve corresponds to a set of tracers released on the blue line in the center vortex (right) and so on. The dashed lines show multiples of the (Eulerian) flow time period .

circulation periods of the mean flow at $Re = 13000$ to the time period of the flow and its subharmonics (fig. 4.3 left) shows that the motion of tracers in secondary vortices more frequently resonates with the perturbing flow field, and hence, those regions contain a larger number of *chaotic* trajectories. The top row in fig. 4.2, indeed, suggests that regions of secondary corner are host the bulk of mixing. Those mixing regions are connected to each other through a mixing band adjacent to the cavity walls.

We note that the uniform distribution of mean vorticity holds for flows at higher Reynolds numbers as well, as evident by the first column of fig. 2.5. However, since the perturbations are not periodic, no resonance analysis can be directly performed. Nevertheless, we speculate that the uniform distribution of vorticity makes the central vortex less prone to develop chaotic trajectories and causes the slow mixing in the center that is observed at quasi-periodic and aperiodic flows.

4.4.2 Approximation of mixing using projection models

In this section, we consider approximation of mixing using the projection models defined in section 4.3. The projection models built using Koopman modes are in fact quasi-periodic approximations of the flow, and the advantage of using such models instead of an aperiodic flow, is that we can extend the dynamical-system techniques to such models. Similarly, low-dimensional projections based on POD might be used to construct effective diffusivity models using e.g. the techniques in [196].

Here is how we measure the error of mixing approximation by a projection model: We advect a blob of material (e.g. a black dye), using the full flow and its projection models, and then measure the distance of the advected blob in the projection models with the full flow. We have chosen the rectanagular blob shown in fig. 4.4. By trial and error, we have found that this choice gives a generic representation of mixing in all the flow regimes. Let $c(\mathbf{x}, t)$ denote the distribution of the black dye at time t. In absence of diffusion, c evolves in time due to the advection by the velocity field,

$$\frac{\partial c}{\partial t} + \mathbf{u} \cdot \nabla c = 0. \tag{4.8}$$

We have solved this equation using the near optimal 5-th order *weighted essentially non-oscillatory* scheme for spatial discretization, and 3rd-order *total-variation-diminishing Runge-Kutta* for time stepping [197]. Figure 4.4 shows the advected blob in the flow at $Re = 20000$ and its projection models of various orders.

To quantify the error of projection models in approximation of mixing, we use the mix-norm introduced in [192]. This type of norm, which is a Sobolev norm of negative index, is proven to be the appropriate choice for evaluation of mixing in advection-dominated transport (see e.g. [198]). Let c' denote the difference of the advected distribution in the flow and a projection model. Assuming that c' is square-integrable, it can be represented

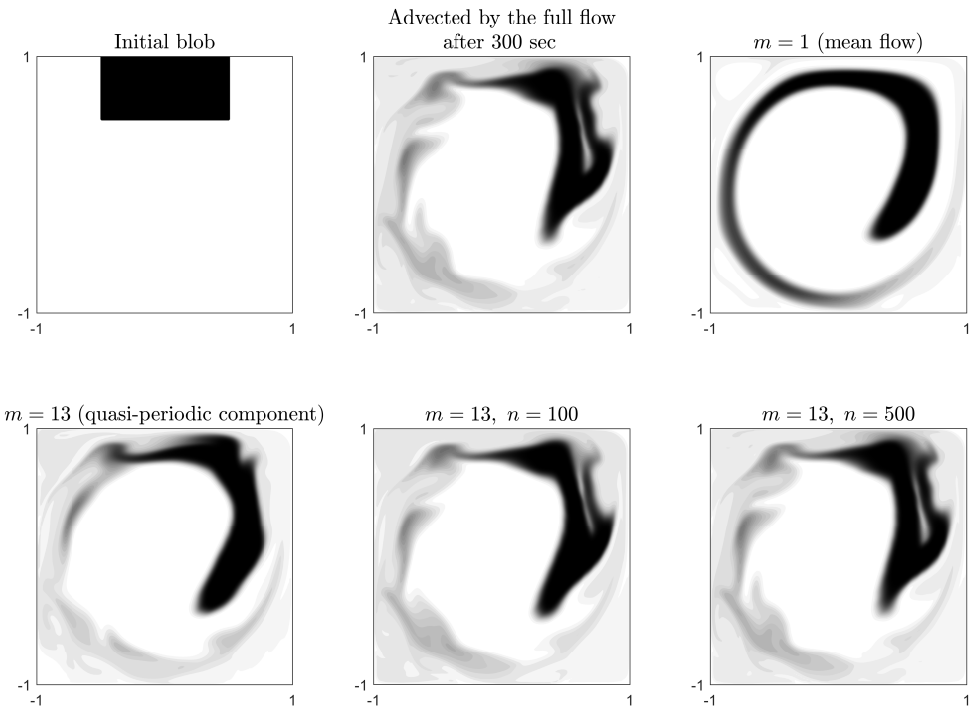

Figure 4.4: Approximating the mixing at $Re = 20000$ using the KMD+POD projection model defined in (4.7). m and n denote the number of Koopman and POD modes, respectively.

as

$$c'(\mathbf{x}) = \sum_{\mathbf{k}\in\mathbb{Z}^2} c_{\mathbf{k}} f_{\mathbf{k}}(\mathbf{x}), \tag{4.9}$$

where $f_{\mathbf{k}}$'s are the standard Fourier basis on the cavity domain, i.e.,

$$f_{\mathbf{k}}(\mathbf{x}) = e^{i\pi(k_1 x + k_2 y)}. \tag{4.10}$$

Then, the mix-norm of c' is defined as

$$\Phi(c') = \sum_{\mathbf{k}\in\mathbb{Z}^2} \frac{1}{\sqrt{1+\pi\|\mathbf{k}\|^2}} c_{\mathbf{k}}, \tag{4.11}$$

which is simply a weighted combination of Fourier coefficients. The main feature of this norm is that it is multiscale; it puts less weight on smaller spatial scales (i.e. Fourier coefficients associated with higher wave numbers). So two distributions would be close in the mix-norm if their large-scale features are similar. Use of mix-norm in studying advection-dominated transport is further justified by considering concepts from measurable dynamical systems theory, for example, if a dynamical system is "mixing", then the mix-norm of any centered measurable observable converges to zero. See the discussion in [192, 198] for further details.

Figure 4.5 shows the normalized error of mixing approximations,

$$\tilde{e}(t) = \frac{\Phi(c'(\mathbf{x},t))}{\Phi(c(\mathbf{x},0))} \tag{4.12}$$

for different flow regimes. The figure suggests that the number of modes required to describe the mixing increases proportionally with the complexity of the Eulerian flow dynamics. The mixing in the periodic flow is 2-dimensional, in the sense that, two Koopman modes (mean flow + the dominant oscillatory Koopman mode) are enough to

describe the advection of the blob within an accuracy of a few percents over long times. The number of modes required to achieve the same level of accuracy is raised to 40 for quasi-periodic flow, and $O(1000)$ for flows with mixed or purely continuous spectrum. This result shows that as the complexity of the flow grows, the process of mixing increases proportionally and tools of modal decomposition like POD and KMD are not suitable to obtain a low-dimensional mixing model of the flow.

4.5 Summary

We made three main observations in this chapter: Mixing in the central vortex of the cavity flow is slower than the areas adjacent to the walls. We explained this for periodic flows using a combination of Koopman mode analysis and the so-called *Prandtl-Batchelor theory* on vorticity distribution in high-Reynolds flows. Based on numerical observations, we conjectured that this theory holds for quasi-periodic flows, and explains the slow growth of mixing in the center compared to the areas adjacent to the walls.

We studied the efficiency of Koopman+POD projection models in approximation of mixing. It turns out that the complexity of the mixing process by advection grows proportional to the complexity of the Eulerian flow dynamics, and no low-order quasi-periodic model (based on data decomposition) can explain the mixing of aperiodic flows accurately.

Another interesting observation was that mixing of cavity flow grows non-monotonically with Reynolds number in the transition regime. This is due to the transfer of kinetic energy to small-scale motion which leads to formation of larger coherent islands. This phenomenon had already been noted in the study of 2D volume-preserving discrete-time maps in dynamical systems theory.

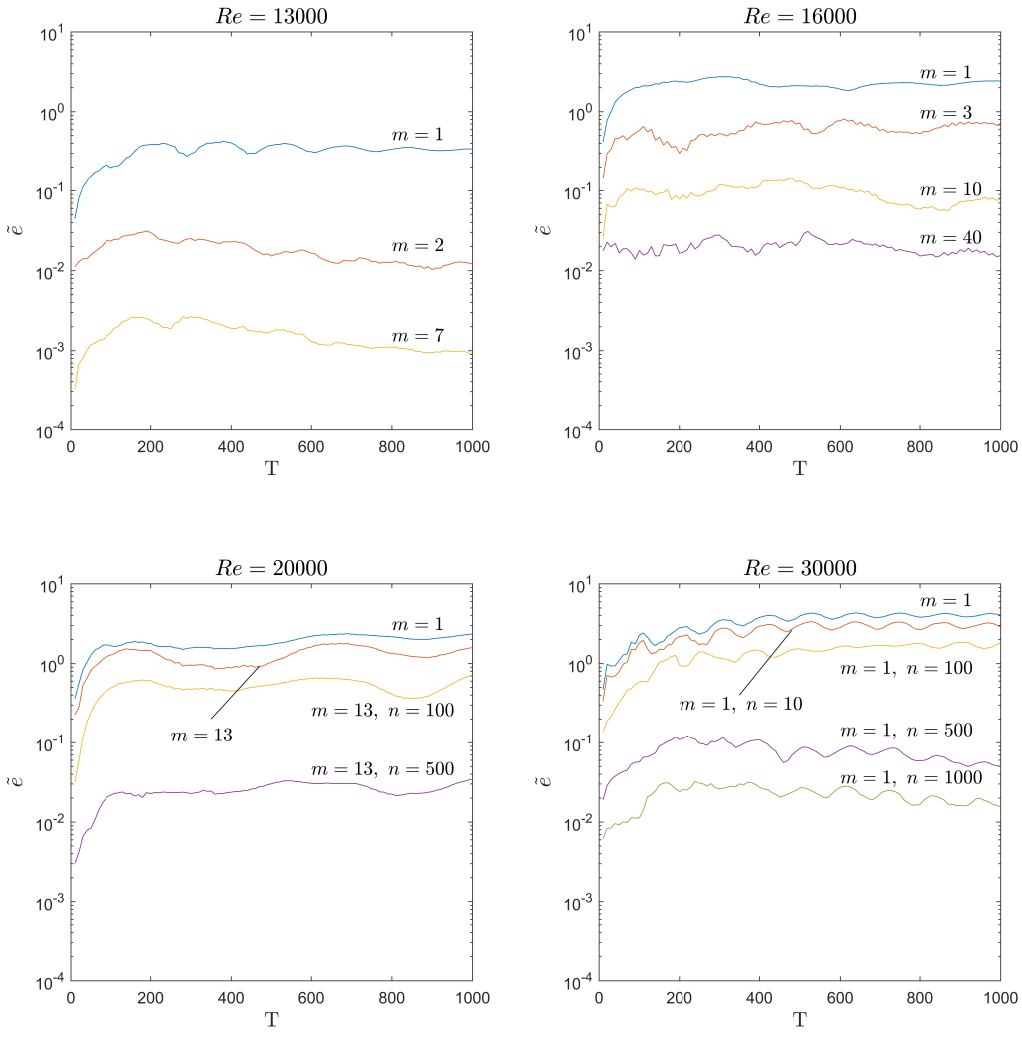

Figure 4.5: Mix-norm error of mixing approximation using projection models defined in (4.7). m and n denote the number of Koopman modes and POD modes used, respectively.

4.6 Appendix: Prandtl-Batchelor theory

4.6.1 The Prandtl-Batchelor theory for steady flows

The Prandtl-Batchelor theory, as stated by [195], maintains that in the regions of steady 2D flow where viscous forces are small and streamlines are closed, the vorticity is constant. The first step in proving this argument is to note that when viscous forces are small, the transport of vorticity in a 2D flow is dominated by advection (i.e. vorticity diffusion is negligible), and therefore vorticity is constant along the streamlines, i.e.,

$$\omega = \omega(\psi) \tag{4.13}$$

where ψ denotes the stream function. Now consider the Navier-Stokes equation written as

$$\frac{\partial \mathbf{u}}{\partial t} + \boldsymbol{\omega} \times \mathbf{u} + \nabla(\frac{u^2}{2}) = -\nabla(\frac{p}{\rho}) + \nu \nabla^2 \mathbf{u}. \tag{4.14}$$

By integrating this equation along a closed streamline, we get

$$\oint \frac{\partial \mathbf{u}}{\partial t} \cdot \mathbf{ds} + \oint \boldsymbol{\omega} \times \mathbf{u} \cdot \mathbf{ds} + \oint \nabla(\frac{u^2}{2} + \frac{p}{\rho}) \cdot \mathbf{ds} = \oint \nu \nabla^2 \mathbf{u} \cdot \mathbf{ds}. \tag{4.15}$$

In steady flows the leftmost term vanishes identically. Moreover, $\mathbf{ds}$ is parallel to the velocity field and perpendicular to $\boldsymbol{\omega} \times \mathbf{u}$ at every point on the streamline, so the second term vanishes as well. And finally, the last term on left-hand-side is zero because it describes the change of a potential function over a closed curve. This leads to the conclusion that sum of the shear forces along the closed streamline is zero, i.e.,

$$\oint \nabla^2 \mathbf{u} \cdot \mathbf{ds} = \oint \nabla \times \boldsymbol{\omega} \cdot \mathbf{ds} = 0. \tag{4.16}$$

Now consider the curvilinear coordinate (s, n) with s and n denoting the increments along and normal to the streamline respectively. In this coordinate system, we have $\mathbf{u} = (q, 0)$ with $q = |\mathbf{u}|$ and $\partial/\partial n = q\partial/\partial\psi$. Using this, (4.16) becomes

$$\oint \nabla \times \boldsymbol{\omega} \cdot \mathbf{ds} = \oint (-\frac{\partial \omega}{\partial n}, \frac{\partial \omega}{\partial s}).(ds, 0) = \oint -\frac{\partial \omega}{\partial n} ds = \oint -\frac{d\omega}{d\psi} q ds = -\frac{d\omega}{d\psi} \oint q ds = 0, \tag{4.17}$$

which implies $d\omega/d\psi = 0$. As a result, the vorticity does not change as we move from one closed streamline to another,

$$\omega(\psi) = \omega_0 \; const. \tag{4.18}$$

4.6.2 Extension to periodic and quasi-periodic flows

A general feature of unsteady cavity flow that is persistent over the considered range of Reynolds number is the relatively uniform distribution of vorticity in the central region of the mean flow (the first Koopman mode). There are no theories that extend the above arguments to the case of unsteady flows. Inspired by the observations in this study, we draw a general condition on the distribution of vorticity in periodic and quasi-periodic flows which, to some extent, resembles the Prandtl-Batchelor theory. Our approach is based on the convergence of Lagrangian averages based on ergodic theory. Consider the evolution of the vorticity in a 2D incompressible flow, given by the Navier-Stokes equation,

$$\frac{D\omega(x,t)}{Dt} = \nu \nabla^2 \omega(x,t) \tag{4.19}$$

By taking the time average of this equation along an arbitrary trajectory starting at x_0 at time 0, we get

$$\frac{1}{T} \int_0^T \frac{D\omega(x,t)}{Dt} dt = \frac{1}{T} \int_0^T \nu \nabla^2 \omega(x,t) dt. \tag{4.20}$$

We take the limit of the above averages as $T \to \infty$,

$$\lim_{T\to\infty} \frac{1}{T} \int_0^T \frac{D\omega(x,t)}{Dt} dt = \lim_{T\to\infty} \frac{1}{T} \int_0^T \nu \nabla^2 \omega(x,t) dt. \tag{4.21}$$

We use $f^*(x_0, t_0)$ to denote the Lagrangian infinite-time average of function f on a trajectory starting at (x_0, t_0), for example,

$$\left(\frac{D\omega}{Dt}\right)^* (x_0, t_0) := \lim_{T\to\infty} \frac{1}{T} \int_0^T \frac{D\omega(x[t], t)}{Dt} dt \tag{4.22}$$

where $x[t]$ is the location of the trajectory at time t. When the velocity field has a periodic or quasi-periodic dependence on time, this average exists for almost every pair of (x_0, t) due to the Birkhoff's ergodic theorem [8]. Moreover, this average must be zero, otherwise the vorticity along the trajectory grows unboundedly. This implies that the right-hand side of (4.21) is zero as well, and the average of the shear forces that the trajectory endures over long times goes to zero. Combining this with the fact that time-averaging operation commutes with the spatial Laplacian operator, we arrive at

$$\begin{aligned} \lim_{T\to\infty} \frac{1}{T} \int_0^T \nu \nabla^2 \omega(x,t) dt &= \nu \nabla^2 \lim_{T\to\infty} \frac{1}{T} \int_0^T \omega(x,t) dt, \\ 0 &= \nabla^2 \omega^*(x_0, t). \end{aligned} \tag{4.23}$$

Furthermore, in a bounded flow with high Reynolds number, the viscous forces in regions far from the wall, e.g., the central region of cavity, are negligible and the vorticity is conserved along the trajectories confined to such regions. Therefore, the Eulerian time average of vorticity at the point x_0, denoted by $\overline{\omega}(x_0)$, could be obtained by tracking

back the vorticity along the trajectory that passes through x_0 at time 0,

$$\overline{\omega}(x_0,0) := \lim_{T\to\infty}\int_0^{\infty}\omega(x_0,t)dt = \lim_{T\to\infty}\int_0^{\infty}\omega(x[-t],-t)dt = \omega_-^*(x_0,0) \tag{4.24}$$

where $\omega_-^*(x_0,0)$ is the Lagrangian average of vorticity on the trajectory starting at $(x_0,0)$ and going backward in time. The previously mentioned ergodic theorem together with the periodic or quasi-periodic dependence of the flow field on time guarantees the existence of this Lagrangian average. Additionally, it must be equal to the forward-time Lagrangian average along the same trajectory. This leads to the conclusion that in the regions far from the wall, the Eulerian and Lagrangian time averages of the vorticity field coincide and

$$\nabla^2\overline{\omega}(x) = 0. \tag{4.25}$$

This Laplace equation governs the distribution of mean vorticity in periodic and quasi-periodic flow in the regions where viscous forces are small. To show that the mean vorticity distribution in the center of cavity is uniform, one only needs to supplement this equation with a constant Dirichlet boundary condition.

In the following, we show the existence of such boundary condition for periodic cavity flow. Let us define the *extended flow domain* as the Cartesian product of the 2D spatial domain with the time axis. In the case of periodic flow, the time axis can be replaced with a circle (given by $\theta \in [0, 2\pi)$) since the dependence of the flow on time is periodic. Now consider the trajectory of passive tracers in the extended flow domain and assume that viscous forces in the center of the cavity are negligible. Then the vorticity is conserved along the trajectories, and the level sets of vorticity form invariant surfaces of the motion in the extended domain. Moreover if the boundaries of the flow field are analytic, the level sets of vorticity form families of tori or invariant surfaces filled with closed orbits [199].

Intersections of such tori with the plane $\theta = 0$ yield families of closed level sets of vorticity. Trajectories starting on such a curve would have the same Lagrangian average for the vorticity and hence the same Eulerian average. Therefore such curve would provide a constant boundary condition for the Laplace equation and proves the uniformity of vorticity in the cavity core. For a quasi periodic flow, the extended domain has (at least) four dimensions and no general description of the invariant surfaces in the flow exists. Therefore, other means should be used to find the appropriate boundary condition for (4.25). For Euler flows with arbitrary time dependence, the Lagrangian averages defined above are not guaranteed to exist and no general conditions on distribution of mean vorticity could be obtained.

Chapter 5

A case study of mixing on the ocean surface: 2015 Refugio Oil Spill

[1] On May 19, 2015, an oil pipeline near Refugio State Park (located 16 miles north of UCSB) broke down, which led to spilling of 21000 gallons of crude oil into the Pacific Ocean. Soon after, a joint committee of federal and state agencies, along with the pipeline company started monitoring the nearby coastal area to detect and control the environmental damage caused by the oil spill. Our research group at UCSB also began a collaboration with Libe Washburn's research group at the Marine Science Institute to estimate the oil spill spread on the surface of the ocean. The short-term goal of this project was to provide the authorities with the information about the likely destinations of floating oil slicks, so that a better cleanup strategy could be devised.

The process of computing the oil spread consisted of two major steps: in the first step, performed in Washburn's Lab, the surface velocity maps for the Santa Barbara channel (i.e. the patch of Pacific Ocean between Santa Barbara coastline and Channel Islands)

[1]This chapter is a report on an ongoing project in collaboration with Libe Washburn's group in Marine Science Institute at UCSB, and Stefan Ivić's group in University of Rijeka, Croatia. I also want to thank Milan Korda for valuable discussions and guidance on the optimization problem.

was computed using the data from a number of High-Frequency (HF) radars located on several spots on the coastline. In the second step, we processed that data and rendered hypergraphs (introduced in section 4.2) of Santa Barbara channel to estimate the likely paths for the oil movement.

A major obstacle that we faced in the above project was that the velocity data computed by HF radars do not satisfy two physical conditions that are expected for incompressible flows: 1- the computed surface velocity had an artificially high divergence which prohibits using hypergraphs (or other techniques based on flow map analysis like LCS detection) for mixing analysis, and 2- the velocity is not zero on the grid points that represent the shoreline and therefore violates the no-slip and no-penetration boundary conditions. The novel aspect of our work was adding a post-processing step to eliminate these problems. Instead of using the velocity field given to us, we looked for the closest velocity field (in the kinetic energy sense) which is both divergence-free and zero-valued on the shoreline. This leads to an optimization problem which has a closed-form linear algebraic solution and can be easily implemented for large data sets. The post-processing step significantly improved the performance of hypergraphs in detecting the destinations of floating oil slicks.

In this chapter, we report on the above post-processing step and present some preliminary results of applying hypergraphs to the Santa Barbara channel. The completion of this project awaits the disclosure of field measurement data from the extent of oil spill by state and federal agencies. This chapter is organized as follows: in section 5.1, we review the oil spill incident. Section 5.2 gives a brief explanation of how HF radars work. Section 5.3 discusses correcting the velocity field to satisfy the appropriate boundary condition and divergence-free condition. In section 5.4, we present the hypergraphs and their utility in the case of Refugio oil spill.

5.1 The oil spill

[2] The oil and gas that is produced on the offshore platforms near Gaviota coast is transported through a subsea pipeline to an ExxonMobil onshore facility located 11 miles north of Goleta. In this facility, the crude oil is separated from gas and other products, and then sent through pipeline 901, which is 10-mile long and operated by Plains All American Pipeline (PAA), to a pump station near Gaviota. From there, the oil is sent to a gathering facility in north of L.A. and thereafter distributed to refineries throughout Southern California. [200, 201, 202].

On the morning of 19 May, 2015, pipeline 901 breached in a location east of the Refugio Beach State Park. The underground pipeline started leaking dozens of yards away from US Highway 101, and soon after, the crude oil started flowing onto a storm drainage under the highway, and found its way to the ocean by passing through the narrow strip of the park that separates the highway from the beach.

The Refugio beach park is one of the most diverse and well-studied marine biological environments on the west coast of US. As a result of the oil spill, hundreds of animals in this area, including dolphins, sea lions and different species of birds and land mammals were covered with crude oil and many of them died [203]. According to PAA, the cleanup operation in the first two months after the spill has cost about 92 million dollars [204], and as of July 2015, the company was expected to end up paying over 160 million dollars more for other damages and legal claims [205]. Besides the local damages, there were also numerous reports of tar balls washing up on other spots on the coast in Ventura as well as beaches in Los Angeles county [206, 207]. In some of those spots, the collected tar balls matched the chemical composition of Refugio oil, however, the comprehensive results of such tests are not officially released. We expect that more information will be

[2]Disclaimer: All the information in this section is gathered from online news sources, and recounted here, only to provide a complete narrative of the study.

disclosed on this subject during the legal trial of the responsible party, which is going to commence in on January 22, 2018.

5.2 HF radar and velocity maps

The operation of an HF radar is based on the backscattering of radio waves from the ocean surface. The radar emits a radio wave, in the range of 10-50 MHz, and then collects the scattered radio wave in the range of wave numbers that are commensurate with the wave numbers of typical ocean surface waves. Using techniques from signal processing, the radar extracts three pieces of information from each signal:

1. Target range: The HF radar emits a frequency modulated wave (i.e. the frequency increases linearly with time), and the traveling time of the signal is estimated by the large-scale frequency shift between the transmitted and received signal. This traveling time multiplied by the wave speed gives the distance of the scattering surface from the radar.

2. Target speed: The motion of the scattering surface causes an extra shift in the frequency of the return signal due to the Doppler effect. This small-scale shift is used to compute the radial component of the surface velocity (where the origin is the radar location). Simultaneous measurements from (at least) one more radar is used to resolve the full velocity vector at the target location.

3. Target bearing (direction): Each radar has multiple receiving antennas with different orientations. The measurements of each antenna depends on its orientation and the direction of the received wave. The latter can be estimated from the difference in the measurements of the antennas.

A more detailed description of HF radar operation can be found in e.g. [208, 209].

The HF radars are capable of measuring surface currents in large areas (up to $150km$ in diameter), and producing maps with high resolution both in space (a few hundred meters) and in time (10-15 minutes). This resolution is still unmatched by other means of collecting ocean surface data, such as in-situ measurements by floating buoys (which are too sparse in space) or satellite maps which have low spatial resolutions (around $30km$ and lower). This makes the data obtained by HF radars a unique resource for guidance of containment operations in case of hazardous material spills.

The data that was used to predict the motion of the oil slicks from the Refugio spill, was rendered using a network of six to seven HF radars on the southern California coast (see [210] for a description of the radar network in the Santa Barbara area). The farthest north radar is located on Point Sal (5 miles west of Santa Maria) and the southernmost was located in Manhattan beach. The data has a spatial and temporal resolution of 2 km and 1 hour, respectively. The top panel in fig. 5.1 shows a snapshot of data rendered by the HF radar network.

5.3 Correction of the velocity field data

As mentioned in the beginning of this chapter, the velocity fields generated from HF radar data suffer from two major inconsistencies: they are not divergence-free, and have non-zero velocity on the shorelines. Note that due to the upwelling process, the non-zero divergence is expected in some spots in the ocean, however, the data provided to us had an order of magnitude higher divergence which is attributed to measurement errors. These two problems have a large negative impact on the performance of the hypergraphs, and we devised a method to remove them. The method is simple: at each time step, we replace the velocity field with another velocity field that is divergence-free and zero on the shorelines, and it has minimum kinetic energy of difference with the original velocity

field. In the following, we formalize this problem and present the solution.

Let $\mathbf{x}$ denote the set of m grid points over which the velocity field data is given. The surface velocity field data at each time instant is $2m$-vector (the velocity has two components at each point), and the set of all such vectors forms the vector space $\mathbb{R}^{2m}$. We define an inner product on this space given by

$$< u, v >= u^* W v, \quad u, v \in \mathbb{R}^{2m}, \tag{5.1}$$

where W is a semi-definite positive matrix which reflects the weight of each grid point in the inner product. We choose W such that it reflects the kinetic energy of the flow field. For example, if $\mathbf{x}$ is a uniform grid, we have $W = \frac{1}{2} I_{2m \times 2m}$. Using this inner product, we can define a new notion of distance on $\mathbb{R}^{2m}$,

$$dist(u, v) = \|u - v\| = \sqrt{< u - v, u - v >} = \sqrt{(u - v)^* W (u - v)}. \tag{5.2}$$

In words, the distance between u and v is the kinetic energy of velocity field $u - v$.

Let D be the discretized divergence operator on $\mathbf{x}$. $\hat{u}$ is divergence-free (in the discrete sense) if $D\hat{u} = 0$. The set of all divergence-free velocity fields forms a subspace in $\mathbb{R}^{2m}$, called the null space of operator D, and denoted by $\mathcal{N}(D)$. We also define P as a linear transformation that maps the velocity field to its values on the shoreline. If there are s grid points on the shoreline, P is a $2s \times 2m$ matrix such that $P_{ii} = 1$ if $\mathbf{x}_i$ is on the shore and $P_{ij} = 0$ otherwise. The null space of P, denoted by $\mathcal{N}(P)$, is exactly the set of velocity fields that satisfy the no-slip boundary condition. As such, any velocity field that satisfies both no-slip and divergence-free condition lies in the subspace $\mathbf{N} = \mathcal{N}(D) \cap \mathcal{N}(P)$. Another way to represent this subspace is to define a new linear

transformation $E = [D \;\; P]^T$ and then

$$\mathbf{N} = \mathcal{N}(E) \tag{5.3}$$

We can recast our problem as follows: Given u, find $\hat{u}$ which is the closest point of $\mathbf{N}$ to u. Or, alternatively,

$$\min_{\hat{u}} dist(\hat{u} - u) \quad s.t. \quad E\hat{u} = 0. \tag{5.4}$$

Since $\mathbf{N}$ is a (closed) subspace, the solution to the above problem exists, and furthermore it is given by orthogonal projection of u onto this subspace [211]. Let A be a full-rank matrix whose columns form a basis of $\mathbf{N}$, then

$$\hat{u} = AA^{\dagger}u. \tag{5.5}$$

where $A^{\dagger}$ is matrix pseudo-inverse [124] with respect to the inner product in (5.1). There are two standard ways to compute a basis for the null space: most accurate and stable method is based on SVD of E which could be computationally intensive while the second method is based on the QR decomposition of E^T which is faster and less memory demanding. In any case, A needs to be computed once, and then it can be used for different snapshots of the velocity field.

In some studies on the ocean transport and mixing, the velocity on the shoreline is replaced with non-zero velocity like diffusive models or bounce-back velocity to stop the trajectories from running into the land. In that case, we would like the solution $\hat{u}$ to satisfy $P\hat{u} = b$ where b is the prescribed velocity field on the shoreline. We can revise the above formulation to solve for such $\hat{u}$ that is also divergence-free, and the closest possible choice to the original velocity field u. The revised form of the optimization problem for

this case becomes

$$\min_{\hat{u}} dist(\hat{u} - u) \quad s.t. \quad E\hat{u} = \begin{bmatrix} 0 \\ b \end{bmatrix}. \tag{5.6}$$

Let us assume for now that we have access to a velocity field v which satisfies the constraint of the above problem ($Ev = [0\ b^T]^T$) but is not necessarily the closest choice to u. We introduce the new optimization variable $w = \hat{u} - v$, and note that

$$Ew = E(\hat{u} - v) = E\hat{u} - Ev = \begin{bmatrix} 0 \\ b \end{bmatrix} - \begin{bmatrix} 0 \\ b \end{bmatrix} = 0 \tag{5.7}$$

Now we can rewrite (5.6) for w,

$$\min_{w} dist(w - (u - v)) \quad s.t. \quad Ew = 0. \tag{5.8}$$

This problem shares an identical form with (5.4) and can be solved similarly using orthogonal projection. Once optimal w is found, we can invert the above variable change and get the solution to (5.6),

$$\hat{u} = AA^{\dagger}(u - v) + v. \tag{5.9}$$

The question remains on how to find an initial v. This requires finding one solution to the undetermined linear system $Ev = [0\ b^T]^T$, and it can be solved either by direct methods (reduced QR for example) or iterative approaches.

Figure 5.1 shows the result of above optimization process (with $b = 0$) for a snapshot of velocity field obtained by HF radar.

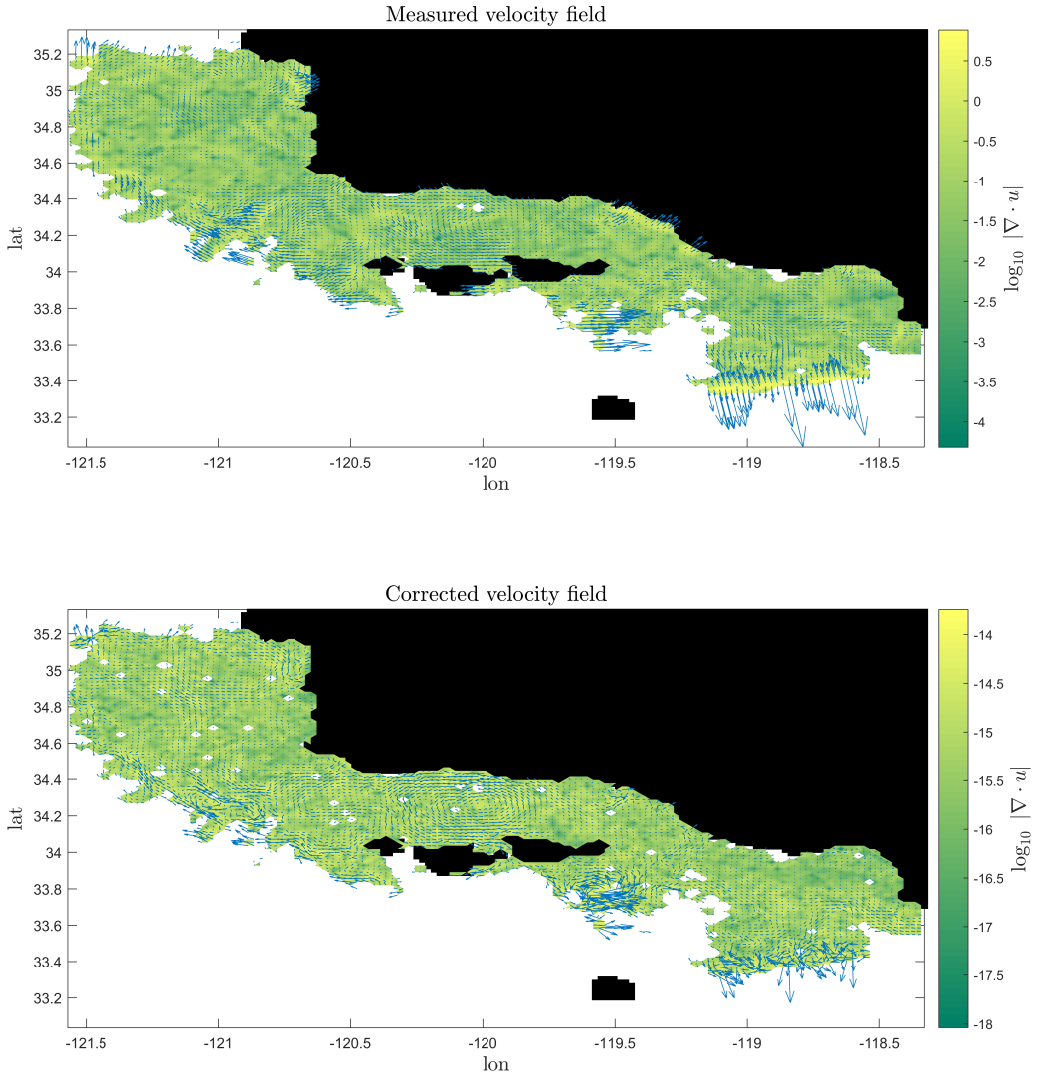

Figure 5.1: The velocity field produced by HF radars (top), and optimized velocity field with zero divergence and zero velocity on the shoreline (bottom). The divergence field unit is sec^{-1}.

5.4 Detecting the extension of the spill using hyperbolic graphs

Just a few days after the oil spill, reports of tar balls washing up on the shores in different areas appeared in the news. (Note that oil slicks usually break up into tar balls due to waves and wind). These shores include Ventura [212], Zuma beach in Malibu [213], and Manhattan Beach [214].

Recall from section 4.2, that the hypergraphs partition the flow domain based on the type of Lagrangian deformation that fluid elements experience. There are three types of Lagrangian behavior: meso-hyperbolic (colored blue in hypergraphs) which shows stretching, meso-elliptic (green) which shows rotational deformation, and meso-helical (red) which shows combination of rotational and stretching behavior. The key property of hypergraphs here is that they show the likely passages for finite-time advective transport in the form of hyperbolic or helical streaks (blue and red streaks). This property was first noted and utilized for oil spill path prediction in [170].

The hypergraphs of Santa Barbara channel in the days after the oil spill (fig. 5.2) reveal a few features of mixing that are important for the oil spreading. First, the surface current around the Refugio beach produces active mixing that moves the oil away from the spill spot. The immediate destination of the oil is the counter-clockwise rotating vortex north of Channel Islands (the vortex can be seen in velocity fields of fig. 5.1). However, the red and blue streaks that extend out of this vortex show that oil is likely to travel to the Santa Cruz Island (rightmost island in the figure) and the Ventura beach. The red and blue streaks also point to other spots farther south on the shore as likely destinations for the tar balls. These spots include the Zuma Beach and Manhattan Beach where tar balls were sighted.

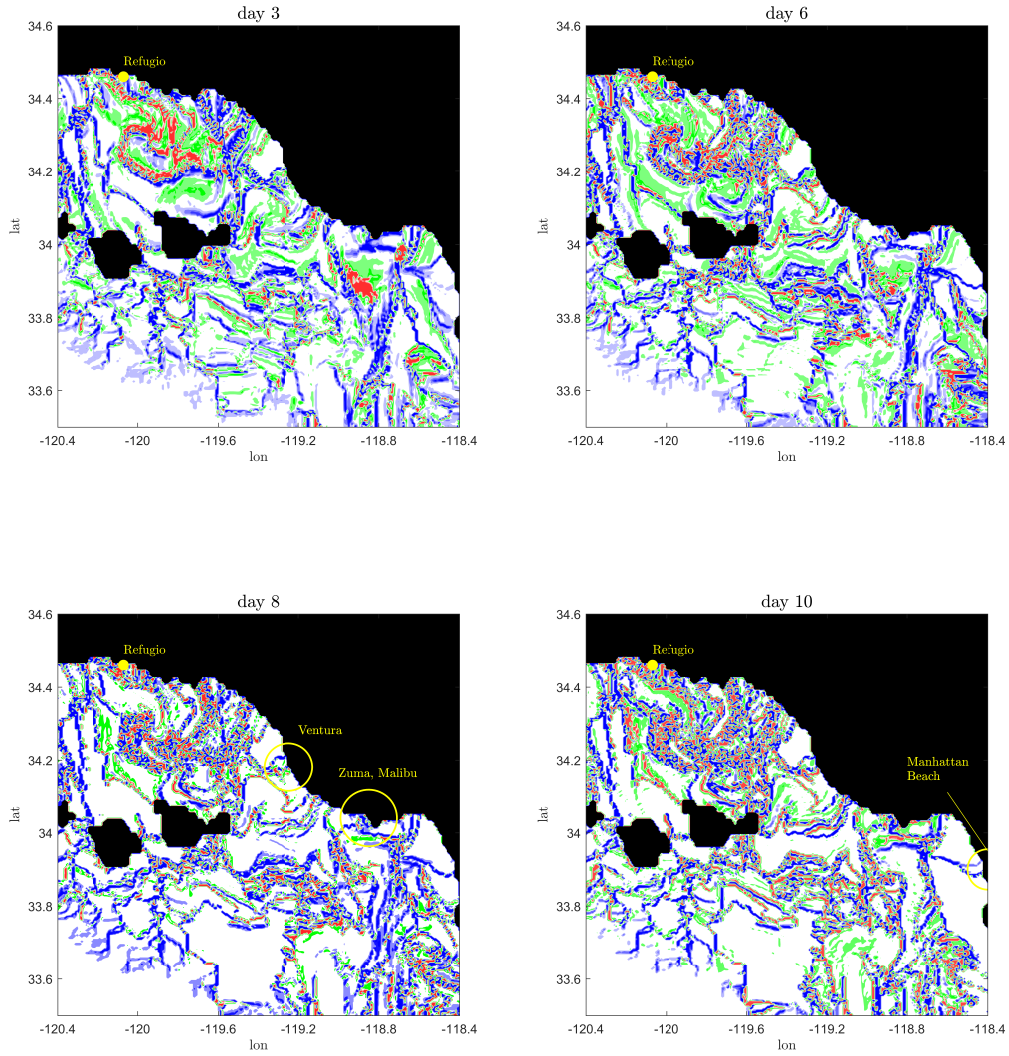

Figure 5.2: Hypergraphs of Santa Barbara channel over different time lapses from the start of the oil spill. The marked spots are some of the locations where tar balls were spotted.

5.5 Future work

In this chapter, we reported on using the real-time data generated by HF radars combined with hypergraphs, for prediction of oil pill extent on the ocean surface. In particular, we devised a post-processing scheme to correct the physical inconsistencies of the data which are detrimental to the performance of the hypergraphs. Application to the case of Refugio oil spill shows the promise of the this methodology (HF radar data + hypergraph analysis) for almost real-time detection of oil spill extent, which could lead to better cleanup or containment strategies. The next step would be to test the performance of hypergraphs against the observational data and creating a software platform to make this analysis more accessible for future applications.

Chapter 6

Conclusion

In this thesis, we studied a few topics at the intersection of fluid mechanics and modern dynamical systems theory. We demonstrated the promise of the Koopman operator framework for comprehensive analysis of post-transient flows, and discussed the use of classical signal processing techniques, as well as modern algorithms like DMD, in extraction of state space dynamics from data. We also investigated the mixing in a bounded shear-driven flow using a combination of tools from the Koopman operator framework, and other tools of dynamical systems like hypergraphs and mix-norm.

The most exciting direction in this line of research is to integrate control into the data-driven framework of the Koopman operator. The control of complex fluid flows have so far evaded general control startegies due to the high-dimensionality and extreme nonlinearity of the flows. The few promising works in the area of Koopman control framework, have dealt with low-dimensional systems, and the current challenge is to extend this analysis to high dimensional systems. This necessitates development of more efficient numerical algorithms for approximation of the Koopman operator, and more effective sampling techniques in high-dimensional spaces.

Our study on lid-driven cavity flow shows that the mixing may not uniformly improve

with the increase of Reynolds. This was attributed to the transfer of kinetic energy into small-scale structures in the velocity field, which leads to formation of large coherent islands in the flow. As such, it seems that a naive increasing of the power input to the flow is not the wisest choice to improve the performance of mixing devices. One strategy to enhance the mixing in these situations is to induce flow motions, for example through modulation of driving solid boundaries, that could break up the those islands based on the resonance phenomena. An ultimate framework for control and enhancement of mixing in general situations would be to formulate the problem as a coupling of the flow dynamics (i.e. Navier Stokes equations) and kinematics (i.e. passive advection equations) into a high-dimensional dynamical system and then apply control techniques. This problem has been studied in a limited capacity so far due to the nonlinearity and high-dimensionality, however, with the advent of data-driven controllers in the near futures, could be a promising area for research.

Finally, one of the most significant problems in the current forefront of science is the modeling of the earth climate. The central challenge lies in the uncertainty in characteristics of mixing process in the atmosphere and ocean. The models that we studied in this work are very simple compared to the climate models and neglect important factors like stratification and external forcing, however, they could be used to build insight for behavior of ultimately high Reynolds flows and development of mixing models using techniques like averaging and homogenization.

Bibliography

[1] J. Guckenheimer and P. Holmes, *Nonlinear oscillations, dynamical systems, and bifurcations of vector fields*, .

[2] S. Wiggins, *Introduction to applied nonlinear dynamical systems and chaos*, vol. 2. Springer Science & Business Media, 2003.

[3] R. Temam, *Infinite-Dimensional Dynamical Systems in Mechanics and Physics*. Springer-Verlag, New York, 1997.

[4] I. Mezić, *Koopman operator spectrum and data analysis*, *arXiv preprint arXiv:1702.07597* (2017).

[5] I. Mezić and A. Banaszuk, *Comparison of systems with complex behavior*, *Physica D: Nonlinear Phenomena* **197** (2004), no. 1 101–133.

[6] B. O. Koopman, *Hamiltonian systems and transformation in Hilbert space*, *Proceedings of the National Academy of Sciences of the United States of America* **17** (1931), no. 5 315.

[7] P. R. Halmos, *The legend of john von neumann*, *The American Mathematical Monthly* **80** (1973), no. 4 382–394.

[8] K. E. Petersen, *Ergodic theory*, vol. 2. Cambridge University Press, 1989.

[9] R. Mane, *Ergodic Theory and Differentiable Dynamics*. Springer-Verlag, New York, 1987.

[10] I. Mezić, *Spectral properties of dynamical systems, model reduction and decompositions*, *Nonlinear Dynamics* **41** (2005), no. 1-3 309–325.

[11] C. Rowley, I. Mezić, S. Bagheri, P. Schlatter, and D. Henningson, *Spectral analysis of nonlinear flows*, *Journal of Fluid Mechanics* **641** (2009), no. 1 115–127.

[12] P. J. Schmid, *Dynamic mode decomposition of numerical and experimental data*, *Journal of fluid mechanics* **656** (2010) 5–28.

[13] P. J. Schmid, *Dynamic mode decomposition of numerical and experimental data*, *Journal of Fluid Mechanics* **656** (2010) 5–28.

[14] P. J. Schmid, L. Li, M. Juniper, and O. Pust, *Applications of the dynamic mode decomposition*, *Theoretical and Computational Fluid Dynamics* **25** (2011), no. 1-4 249–259.

[15] C. Pan, D. Yu, and J. Wang, *Dynamical mode decomposition of gurney flap wake flow*, *Theoretical and Applied Mechanics Letters* **1** (2011), no. 1.

[16] A. Seena and H. J. Sung, *Dynamic mode decomposition of turbulent cavity flows for self-sustained oscillations*, *International Journal of Heat and Fluid Flow* **32** (2011), no. 6 1098–1110.

[17] T. W. Muld, G. Efraimsson, and D. S. Henningson, *Flow structures around a high-speed train extracted using proper orthogonal decomposition and dynamic mode decomposition*, *Computers & Fluids* **57** (2012) 87–97.

[18] J.-C. Hua, G. H. Gunaratne, D. G. Talley, J. R. Gord, and S. Roy, *Dynamic-mode decomposition based analysis of shear coaxial jets with and without transverse acoustic driving*, *Journal of Fluid Mechanics* **790** (2016) 5–32.

[19] S. Bagheri, *Koopman-mode decomposition of the cylinder wake*, *J. Fluid Mech* **726** (2013) 596–623.

[20] T. Sayadi, P. J. Schmid, J. W. Nichols, and P. Moin, *Reduced-order representation of near-wall structures in the late transitional boundary layer*, *Journal of Fluid Mechanics* **748** (2014) 278–301.

[21] P. K. Subbareddy, M. D. Bartkowicz, and G. V. Candler, *Direct numerical simulation of high-speed transition due to an isolated roughness element*, *Journal of Fluid Mechanics* **748** (2014) 848–878.

[22] I. Mezić, *Analysis of fluid flows via spectral properties of the koopman operator*, *Annual Review of Fluid Mechanics* **45** (2013) 357–378.

[23] M. Georgescu and I. Mezić, *Building energy modeling: A systematic approach to zoning and model reduction using koopman mode analysis*, *Energy and buildings* **86** (2015) 794–802.

[24] M. Georgescu, S. Loire, D. Kasper, and I. Mezic, *Whole-building fault detection: A scalable approach using spectral methods*, *arXiv preprint arXiv:1703.07048* (2017).

[25] Y. Susuki and I. Mezić, *Nonlinear koopman modes and coherency identification of coupled swing dynamics*, *IEEE Transactions on Power Systems* **26** (2011), no. 4 1894–1904.

[26] Y. Susuki and I. Mezić, *Nonlinear koopman modes and power system stability assessment without models*, *IEEE Transactions on Power Systems* **29** (2014), no. 2 899–907.

[27] B. W. Brunton, L. A. Johnson, J. G. Ojemann, and J. N. Kutz, *Extracting spatial–temporal coherent patterns in large-scale neural recordings using dynamic mode decomposition*, *Journal of neuroscience methods* **258** (2016) 1–15.

[28] J. N. Kutz, X. Fu, S. L. Brunton, and N. B. Erichson, *Multi-resolution dynamic mode decomposition for foreground/background separation and object tracking*, in *Computer Vision Workshop (ICCVW), 2015 IEEE International Conference on*, pp. 921–929, IEEE, 2015.

[29] N. B. Erichson, S. L. Brunton, and J. N. Kutz, *Compressed dynamic mode decomposition for background modeling*, *Journal of Real-Time Image Processing* (2016) 1–14.

[30] J. Mann and J. N. Kutz, *Dynamic mode decomposition for financial trading strategies*, *Quantitative Finance* (2016) 1–13.

[31] M. O. Williams, I. G. Kevrekidis, and C. W. Rowley, *A data–driven approximation of the koopman operator: Extending dynamic mode decomposition*, *Journal of Nonlinear Science* **25** (2015), no. 6 1307–1346.

[32] K. K. Chen, J. H. Tu, and C. W. Rowley, *Variants of dynamic mode decomposition: boundary condition, koopman, and fourier analyses*, *Journal of Nonlinear Science* **22** (2012), no. 6 887–915.

[33] J. H. Tu, C. W. Rowley, D. M. Luchtenburg, S. L. Brunton, and J. N. Kutz, *On dynamic mode decomposition: theory and applications*, *Journal of Computational Dynamics* (2014).

[34] J. N. Kutz, X. Fu, and S. L. Brunton, *Multiresolution dynamic mode decomposition*, *SIAM Journal on Applied Dynamical Systems* **15** (2016), no. 2 713–735.

[35] J. L. Proctor, S. L. Brunton, and J. N. Kutz, *Dynamic mode decomposition with control*, *SIAM Journal on Applied Dynamical Systems* **15** (2016), no. 1 142–161.

[36] M. S. Hemati, M. O. Williams, and C. W. Rowley, *Dynamic mode decomposition for large and streaming datasets*, *Physics of Fluids* **26** (2014), no. 11 111701.

[37] F. Guéniat, L. Mathelin, and L. R. Pastur, *A dynamic mode decomposition approach for large and arbitrarily sampled systems*, *Physics of Fluids* **27** (2015), no. 2 025113.

[38] S. L. Brunton, J. L. Proctor, and J. N. Kutz, *Compressive sampling and dynamic mode decomposition*, *arXiv preprint arXiv:1312.5186* (2013).

[39] S. T. Dawson, M. S. Hemati, M. O. Williams, and C. W. Rowley, *Characterizing and correcting for the effect of sensor noise in the dynamic mode decomposition*, *Experiments in Fluids* **57** (2016), no. 3 1–19.

[40] M. S. Hemati, C. W. Rowley, E. A. Deem, and L. N. Cattafesta, *De-biasing the dynamic mode decomposition for applied koopman spectral analysis of noisy datasets*, *Theoretical and Computational Fluid Dynamics* (2017) 1–20.

[41] H. Arbabi and I. Mezić, *Ergodic theory, dynamic mode decomposition and computation of spectral properties of the koopman operator*, *arXiv preprint arXiv:1611.06664* (2016).

[42] M. Korda and I. Mezić, *On convergence of extended dynamic mode decomposition to the koopman operator*, *arXiv preprint arXiv:1703.04680* (2017).

[43] S. L. Brunton, B. W. Brunton, J. L. Proctor, and J. N. Kutz, *Koopman invariant subspaces and finite linear representations of nonlinear dynamical systems for control*, *PloS one* **11** (2016), no. 2 e0150171.

[44] A. Surana, *Koopman operator based observer synthesis for control-affine nonlinear systems*, in *Decision and Control (CDC), 2016 IEEE 55th Conference on*, pp. 6492–6499, IEEE, 2016.

[45] A. Surana and A. Banaszuk, *Linear observer synthesis for nonlinear systems using koopman operator framework*, *IFAC-PapersOnLine* **49** (2016), no. 18 716–723.

[46] M. Korda and I. Mezić, *Linear predictors for nonlinear dynamical systems: Koopman operator meets model predictive control*, *arXiv preprint arXiv:1611.03537* (2016).

[47] E. Kaiser, J. N. Kutz, and S. L. Brunton, *Data-driven discovery of koopman eigenfunctions for control*, *arXiv preprint arXiv:1707.01146* (2017).

[48] H. L. Swinney and J. P. Gollub, *The transition to turbulence*, *Phys. Today* **31** (1978), no. 8.

[49] D. Farmer, J. Crutchfield, H. Froehling, N. Packard, and R. Shaw, *Power spectra and mixing properties of strange attractors*, *Annals of the New York Academy of Sciences* **357** (1980), no. 1 453–471.

[50] G. E. Karniadakis and G. S. Triantafyllou, *Three-dimensional dynamics and transition to turbulence in the wake of bluff objects*, *Journal of Fluid Mechanics* **238** (1992) 1–30.

[51] A. G. Tomboulides and S. A. Orszag, *Numerical investigation of transitional and weak turbulent flow past a sphere*, *Journal of Fluid Mechanics* **416** (2000) 45–73.

[52] Y.-F. Peng, Y.-H. Shiau, and R. R. Hwang, *Transition in a 2-d lid-driven cavity flow*, *Computers & Fluids* **32** (2003), no. 3 337–352.

[53] J. Basley, L. Pastur, F. Lusseyran, T. M. Faure, and N. Delprat, *Experimental investigation of global structures in an incompressible cavity flow using time-resolved piv*, *Experiments in Fluids* **50** (2011), no. 4 905–918.

[54] D. Giannakis, *Data-driven spectral decomposition and forecasting of ergodic dynamical systems*, *Applied and Computational Harmonic Analysis* (2017).

[55] K. Taira, S. L. Brunton, S. Dawson, C. W. Rowley, T. Colonius, B. J. McKeon, O. T. Schmidt, S. Gordeyev, V. Theofilis, and L. S. Ukeiley, *Modal analysis of fluid flows: An overview*, *arXiv preprint arXiv:1702.01453* (2017).

[56] J. Laskar, *The chaotic motion of the solar system: a numerical estimate of the size of the chaotic zones*, *Icarus* **88** (1990), no. 2 266–291.

[57] J. Laskar, C. Froeschlé, and A. Celletti, *The measure of chaos by the numerical analysis of the fundamental frequencies. application to the standard mapping*, *Physica D: Nonlinear Phenomena* **56** (1992), no. 2-3 253–269.

[58] P. Welch, *The use of fast fourier transform for the estimation of power spectra: a method based on time averaging over short, modified periodograms*, *IEEE Transactions on audio and electroacoustics* **15** (1967), no. 2 70–73.

[59] A. Wynn, D. Pearson, B. Ganapathisubramani, and P. Goulart, *Optimal mode decomposition for unsteady flows*, *Journal of Fluid Mechanics* **733** (2013) 473.

[60] M. R. Jovanović, P. J. Schmid, and J. W. Nichols, *Sparsity-promoting dynamic mode decomposition*, *Physics of Fluids (1994-present)* **26** (2014), no. 2 024103.

[61] G. Tissot, L. Cordier, N. Benard, and B. R. Noack, *Model reduction using dynamic mode decomposition*, *Comptes Rendus Mécanique* **342** (2014), no. 6 410–416.

[62] P. R. Halmos, *Lectures on ergodic theory*, vol. 142. American Mathematical Soc., 1956.

[63] B. MacCluer, *Elementary functional analysis*, vol. 253. Springer Science & Business Media, 2008.

[64] S. Luzzatto, I. Melbourne, and F. Paccaut, *The lorenz attractor is mixing*, *Communications in Mathematical Physics* **260** (2005), no. 2 393–401.

[65] J. L. Doob, *Stochastic processes*, vol. 7. Wiley New York, 1953.

[66] P. Z. Peebles, *Probability, random variables, and random signal principles*.

[67] N. Wiener and A. Wintner, *Harmonic analysis and ergodic theory*, *American Journal of Mathematics* **63** (1941), no. 2 415–426.

[68] U. Ghia, K. N. Ghia, and C. Shin, *High-re solutions for incompressible flow using the navier-stokes equations and a multigrid method*, *Journal of computational physics* **48** (1982), no. 3 387–411.

[69] M. Gharib and P. Derango, *A liquid film (soap film) tunnel to study two-dimensional laminar and turbulent shear flows*, *Physica D: Nonlinear Phenomena* **37** (1989), no. 1-3 406–416.

[70] Y. Tseng and J. H. Ferziger, *Mixing and available potential energy in stratified flows*, *Physics of Fluids* **13** (2001), no. 5 1281–1293.

[71] H. Gildor, E. Fredj, and A. Kostinski, *The gulf of eilat/aqaba: a natural driven cavity?*, *Geophysical and Astrophysical Fluid Dynamics* **104** (2010), no. 4 301–308.

[72] R. Chella and J. M. Ottino, *Fluid mechanics of mixing in a single-screw extruder*, *Industrial & engineering chemistry fundamentals* **24** (1985), no. 2 170–180.

[73] J. Shen, *Hopf bifurcation of the unsteady regularized driven cavity flow*, *Journal of Computational Physics* **245** (1991), no. 199 1 228–245.

[74] M. Poliashenko and C. K. Aidun, *A direct method for computation of simple bifurcations*, *Journal of Computational Physics* **121** (1995), no. 2 246–260.

[75] W. Cazemier, R. Verstappen, and A. Veldman, *Proper orthogonal decomposition and low-dimensional models for driven cavity flows*, *Physics of Fluids (1994-present)* **10** (1998), no. 7 1685–1699.

[76] F. Auteri, N. Parolini, and L. Quartapelle, *Numerical investigation on the stability of singular driven cavity flow*, *Journal of Computational Physics* **183** (2002), no. 1 1–25.

[77] M. J. Balajewicz, E. H. Dowell, and B. R. Noack, *Low-dimensional modelling of high-reynolds-number shear flows incorporating constraints from the navier–stokes equation*, *Journal of Fluid Mechanics* **729** (2013) 285–308.

[78] O. Botella, *On the solution of the navier-stokes equations using chebyshev projection schemes with third-order accuracy in time*, *Computers & Fluids* **26** (1997), no. 2 107–116.

[79] R. Temam, *Infinite-dimensional dynamical systems in mechanics and physics*, vol. 68. Springer-Verlag, 1988.

[80] L. N. Trefethen, *Spectral methods in MATLAB*, vol. 10. Siam, 2000.

[81] P. Stoica, R. L. Moses, *et. al.*, *Spectral analysis of signals*, vol. 452. Pearson Prentice Hall Upper Saddle River, NJ, 2005.

[82] M. Ghil, M. Allen, M. Dettinger, K. Ide, D. Kondrashov, M. Mann, A. W. Robertson, A. Saunders, Y. Tian, F. Varadi, *et. al.*, *Advanced spectral methods for climatic time series*, *Reviews of geophysics* **40** (2002), no. 1.

[83] J. Li and P. Stoica, *Efficient mixed-spectrum estimation with applications to target feature extraction*, *IEEE transactions on signal processing* **44** (1996), no. 2 281–295.

[84] P. Stoica, A. Jakobsson, and J. Li, *Cisoid parameter estimation in the colored noise case: asymptotic cramer-rao bound, maximum likelihood, and nonlinear least-squares*, *IEEE Transactions on Signal Processing* **45** (1997), no. 8 2048–2059.

[85] I. Mezić and F. Sotiropoulos, *Ergodic theory and experimental visualization of invariant sets in chaotically advected flows*, *Physics of Fluids (1994-present)* **14** (2002), no. 7 2235–2243.

[86] U. Krengel and A. Brunel, *Ergodic theorems*, vol. 59. Cambridge Univ Press, 1985.

[87] S. R. Oppenheim, AV and J. Buck, *Discrete-time signal processing*. Prentice-Hall, NJ, 1999.

[88] V. K. Jain, W. L. Collins, and D. C. Davis, *High-accuracy analog measurements via interpolated fft*, *IEEE Transactions on Instrumentation and Measurement* **28** (1979), no. 2 113–122.

[89] G. Andria, M. Savino, and A. Trotta, *Windows and interpolation algorithms to improve electrical measurement accuracy*, *IEEE Transactions on Instrumentation and Measurement* **38** (1989), no. 4 856–863.

[90] D. Agrez, *Weighted multipoint interpolated dft to improve amplitude estimation of multifrequency signal*, *IEEE Transactions on Instrumentation and Measurement* **51** (2002), no. 2 287–292.

[91] B. G. R. De Prony, *Essai éxperimental et analytique: sur les lois de la dilatabilité de fluides élastique et sur celles de la force expansive de la vapeur de lalkool,a différentes températures*, *Journal de lécole polytechnique* **1** (1795), no. 22 24–76.

[92] Y. Susuki and I. Mezić, *A prony approximation of koopman mode decomposition*, in *Decision and Control (CDC), 2015 IEEE 54th Annual Conference on*, pp. 7022–7027, IEEE, 2015.

[93] R. Schmidt, *Multiple emitter location and signal parameter estimation*, *IEEE transactions on antennas and propagation* **34** (1986), no. 3 276–280.

[94] R. Roy and T. Kailath, *Esprit-estimation of signal parameters via rotational invariance techniques*, *IEEE Transactions on acoustics, speech, and signal processing* **37** (1989), no. 7 984–995.

[95] E. J. Candès and C. Fernandez-Granda, *Towards a mathematical theory of super-resolution*, *Communications on Pure and Applied Mathematics* **67** (2014), no. 6 906–956.

[96] C. Fernandez-Granda, *Super-resolution of point sources via convex programming*, *Information and Inference: A Journal of the IMA* **5** (2016), no. 3 251–303.

[97] J. A. Tropp and A. C. Gilbert, *Signal recovery from random measurements via orthogonal matching pursuit*, *IEEE Transactions on information theory* **53** (2007), no. 12 4655–4666.

[98] S. G. Mallat and Z. Zhang, *Matching pursuits with time-frequency dictionaries*, *IEEE Transactions on signal processing* **41** (1993), no. 12 3397–3415.

[99] Y. Wang, *Seismic time-frequency spectral decomposition by matching pursuit*, *Geophysics* **72** (2006), no. 1 V13–V20.

[100] A. Fannjiang and W. Liao, *Coherence pattern–guided compressive sensing with unresolved grids*, *SIAM Journal on Imaging Sciences* **5** (2012), no. 1 179–202.

[101] B. Mamandipoor, D. Ramasamy, and U. Madhow, *Newtonized orthogonal matching pursuit: Frequency estimation over the continuum.*, *IEEE Trans. Signal Processing* **64** (2016), no. 19 5066–5081.

[102] P. Stoica and A. Nehorai, *Statistical analysis of two nonlinear least-squares estimators of sine-wave parameters in the colored-noise case*, *Circuits, Systems and Signal Processing* **8** (1989), no. 1 3–15.

[103] M. S. Bartlett, *Periodogram analysis and continuous spectra*, *Biometrika* **37** (1950), no. 1/2 1–16.

[104] R. B. Blackman and J. W. Tukey, *The measurement of power spectra from the point of view of communications engineeringpart i*, *Bell Labs Technical Journal* **37** (1958), no. 1 185–282.

[105] N. Govindarajan, R. Mohr, S. Chandrasekaran, and I. Mezić, *A convergent numerical method for computing koopman spectra of volume-preserving maps on the d-torus*, *preprint* (2017).

[106] M. Korda, M. Putinar, and I. Mezić, *Data-driven spectral analysis of the koopman operator*, *arXiv preprint arXiv:1710.06532* (2017).

[107] H. Broer and F. Takens, *Mixed spectra and rotational symmetry*, *Archive for rational mechanics and analysis* **124** (1993), no. 1 13–42.

[108] D. Ruelle and F. Takens, *On the nature of turbulence*, *Commun. math. phys* **20** (1971), no. 3 167–192.

[109] F. Takens, *Detecting strange attractors in turbulence*, in *Dynamical systems and turbulence, Warwick 1980*, pp. 366–381. Springer, 1981.

[110] N. Mukolobwiez, A. Chiffaudel, and F. Daviaud, *Supercritical eckhaus instability for surface-tension-driven hydrothermal waves*, *Physical review letters* **80** (1998), no. 21 4661.

[111] N. Garnier, A. Chiffaudel, F. Daviaud, and A. Prigent, *Nonlinear dynamics of waves and modulated waves in 1d thermocapillary flows. i. general presentation and periodic solutions*, *Physica D: Nonlinear Phenomena* **174** (2003), no. 1 1–29.

[112] M. J. Mercier, N. B. Garnier, and T. Dauxois, *Reflection and diffraction of internal waves analyzed with the hilbert transform*, *Physics of Fluids* **20** (2008), no. 8 086601.

[113] B. R. Noack, K. Afanasiev, M. Morzynski, G. Tadmor, and F. Thiele, *A hierarchy of low-dimensional models for the transient and post-transient cylinder wake*, *Journal of Fluid Mechanics* **497** (2003) 335–363.

[114] G. Berkooz, P. Holmes, and J. L. Lumley, *The proper orthogonal decomposition in the analysis of turbulent flows*, *Annual review of fluid mechanics* **25** (1993), no. 1 539–575.

[115] J. Lopez and F. Marques, *Dynamics of three-tori in a periodically forced navier-stokes flow*, *Physical review letters* **85** (2000), no. 5 972.

[116] Y. Takeda, *Quasi-periodic state and transition to turbulence in a rotating couette system*, *Journal of Fluid Mechanics* **389** (1999) 81–99.

[117] A. Guzmán and C. Amon, *Transition to chaos in converging–diverging channel flows: Ruelle–takens–newhouse scenario*, *Physics of Fluids* **6** (1994), no. 6 1994–2002.

[118] T. Sauer, J. A. Yorke, and M. Casdagli, *Embedology*, *Journal of statistical Physics* **65** (1991), no. 3 579–616.

[119] J.-N. Juang and R. S. Pappa, *An eigensystem realization algorithm for modal parameter identification and model reduction*, *Journal of guidance, control, and dynamics* **8** (1985), no. 5 620–627.

[120] P. Van Overschee and B. De Moor, *Subspace identification for linear systems: TheoryImplementationApplications*. Springer Science & Business Media, 2012.

[121] S. L. Brunton, B. W. Brunton, J. L. Proctor, E. Kaiser, and J. N. Kutz, *Chaos as an intermittently forced linear system*, *arXiv preprint arXiv:1608.05306* (2016).

[122] D. Giannakis, *Data-driven spectral decomposition and forecasting of ergodic dynamical systems*, *arXiv preprint arXiv:1507.02338* (2015).

[123] S. Klus, P. Koltai, and C. Schütte, *On the numerical approximation of the perron-frobenius and koopman operator*, *arXiv preprint arXiv:1512.05997* (2015).

[124] L. N. Trefethen and D. Bau III, *Numerical linear algebra*, vol. 50. Siam, 1997.

[125] K. Petersen, *Ergodic Theory*. Cambridge University Press, Cambridge, 1995.

[126] Y. Saad, *Numerical Methods for Large Eigenvalue Problems: Revised Edition*. SIAM, 2011.

[127] J.-P. Eckmann and D. Ruelle, *Ergodic theory of chaos and strange attractors*, *Reviews of modern physics* **57** (1985), no. 3 617.

[128] L. Young, *What are SRB measures, and which dynamical systems have them?*, *Journal of Statistical Physics* **108** (2002), no. 5 733–754.

[129] P. Holmes, J. L. Lumley, G. Berkooz, and C. W. Rowley, *Turbulence, coherent structures, dynamical systems and symmetry*. Cambridge university press, 2012.

[130] L. Sirovich, *Turbulence and the dynamics of coherent structures part i: coherent structures*, *Quarterly of applied mathematics* **45** (1987), no. 3 561–571.

[131] E. N. Lorenz, *Deterministic nonperiodic flow*, *Journal of the atmospheric sciences* **20** (1963), no. 2 130–141.

[132] U. Krengel and A. Brunel, *Ergodic theorems*, vol. 59. Cambridge Univ Press, 1985.

[133] A. Mauroy and I. Mezić, *On the use of fourier averages to compute the global isochrons of (quasi) periodic dynamics*, *Chaos: An Interdisciplinary Journal of Nonlinear Science* **22** (2012), no. 3 033112.

[134] S. R. Taylor, R. Gunawan, L. R. Petzold, and F. J. Doyle III, *Sensitivity measures for oscillating systems: Application to mammalian circadian gene network*, *IEEE transactions on automatic control* **53** (2008), no. Special Issue 177–188.

[135] P. Danzl, J. Hespanha, and J. Moehlis, *Event-based minimum-time control of oscillatory neuron models*, *Biological cybernetics* **101** (2009), no. 5 387–399.

[136] W. G. Large, J. C. McWilliams, and S. C. Doney, *Oceanic vertical mixing: A review and a model with a nonlocal boundary layer parameterization*, *Reviews of Geophysics* **32** (1994), no. 4 363–403.

[137] S. C. Sherwood, S. Bony, and J.-L. Dufresne, *Spread in model climate sensitivity traced to atmospheric convective mixing*, *Nature* **505** (2014), no. 7481 37–42.

[138] C. Coulliette, F. Lekien, J. D. Paduan, G. Haller, and J. E. Marsden, *Optimal pollution mitigation in monterey bay based on coastal radar data and nonlinear dynamics*, *Environmental science & technology* **41** (2007), no. 18 6562–6572.

[139] S. Ferrachat and Y. Ricard, *Mixing properties in the earth's mantle: effects of the viscosity stratification and of oceanic crust segregation*, *Geochemistry, Geophysics, Geosystems* **2** (2001), no. 4.

[140] S. C. Shadden and C. A. Taylor, *Characterization of coherent structures in the cardiovascular system*, *Annals of biomedical engineering* **36** (2008), no. 7 1152–1162.

[141] D. L. Valentine, I. Mezić, S. Maćevsić, N. vCrnjarić-vZic, S. Ivić, P. J. Hogan, V. A. Fonoberov, and S. Loire, *Dynamic autoinoculation and the microbial ecology of a deep water hydrocarbon irruption*, *Proceedings of the National Academy of Sciences* **109** (2012), no. 50 20286–20291.

[142] D. Khakhar, J. Franjione, and J. Ottino, *A case study of chaotic mixing in deterministic flows: the partitioned-pipe mixer*, *Chemical Engineering Science* **42** (1987), no. 12 2909–2926.

[143] A. D. Stroock, S. K. Dertinger, A. Ajdari, I. Mezić, H. A. Stone, and G. M. Whitesides, *Chaotic mixer for microchannels*, *Science* **295** (2002), no. 5555 647–651.

[144] H. Aref, *Stirring by chaotic advection*, *Journal of fluid mechanics* **143** (1984) 1–21.

[145] J. M. Ottino, *The kinematics of mixing: stretching, chaos, and transport*, vol. 3. Cambridge university press, 1989.

[146] V. Rom-Kedar, A. Leonard, and S. Wiggins, *An analytical study of transport, mixing and chaos in an unsteady vortical flow*, *Journal of Fluid Mechanics* **214** (1990) 347–394.

[147] S. Wiggins, *Chaotic transport in dynamical systems*, vol. 2. Springer-Verlag, 1991.

[148] H. Aref, J. R. Blake, M. Budisić, S. S. S. Cardoso, J. H. E. Cartwright, H. J. H. Clercx, K. El Omari, U. Feudel, R. Golestanian, E. Gouillart, G. F. van Heijst, T. S. Krasnopolskaya, Y. Le Guer, R. S. MacKay, V. V. Meleshko, G. Metcalfe, I. Mezić, A. P. S. de Moura, O. Piro, M. F. M. Speetjens, R. Sturman, J.-L. Thiffeault, and I. Tuval, *Frontiers of chaotic advection*, *Rev. Mod. Phys.* **89** (Jun, 2017) 025007.

[149] G. Haller, *Lagrangian coherent structures*, *Annual Review of Fluid Mechanics* **47** (2015) 137–162.

[150] G. Haller and G. Yuan, *Lagrangian coherent structures and mixing in two-dimensional turbulence*, *Physica D: Nonlinear Phenomena* **147** (2000), no. 3 352–370.

[151] D. Blazevski and G. Haller, *Hyperbolic and elliptic transport barriers in three-dimensional unsteady flows*, *Physica D: Nonlinear Phenomena* **273** (2014) 46–62.

[152] S. C. Shadden, F. Lekien, and J. E. Marsden, *Definition and properties of lagrangian coherent structures from finite-time lyapunov exponents in two-dimensional aperiodic flows*, *Physica D: Nonlinear Phenomena* **212** (2005), no. 3 271–304.

[153] M. Farazmand and G. Haller, *Computing Lagrangian coherent structures from their variational theory.*, *Chaos (Woodbury, N.Y.)* **22** (Mar., 2012) 013128.

[154] P. L. Boyland, H. Aref, and M. A. Stremler, *Topological fluid mechanics of stirring*, *Journal of Fluid Mechanics* **403** (2000) 277–304.

[155] J.-L. Thiffeault and M. D. Finn, *Topology, braids and mixing in fluids*, *Philosophical Transactions of the Royal Society of London A: Mathematical, Physical and Engineering Sciences* **364** (2006), no. 1849 3251–3266.

[156] E. Gouillart, J.-L. Thiffeault, and M. D. Finn, *Topological mixing with ghost rods*, *Physical Review E* **73** (2006), no. 3 036311.

[157] M. R. Allshouse and J.-L. Thiffeault, *Detecting coherent structures using braids*, *Physica D: Nonlinear Phenomena* **241** (2012), no. 2 95–105.

[158] M. Budisić and J.-L. Thiffeault, *Finite-time braiding exponents*, *Chaos: An Interdisciplinary Journal of Nonlinear Science* **25** (2015), no. 8 087407.

[159] M. Dellnitz and O. Junge, *Almost invariant sets in chua's circuit*, *International Journal of Bifurcation and Chaos* **7** (1997), no. 11 2475–2485.

[160] M. Dellnitz and O. Junge, *On the approximation of complicated dynamical behavior*, *SIAM Journal on Numerical Analysis* **36** (1999), no. 2 491–515.

[161] G. Froyland, S. Lloyd, and N. Santitissadeekorn, *Coherent sets for nonautonomous dynamical systems*, *Physica D: Nonlinear Phenomena* **239** (2010), no. 16 1527–1541.

[162] G. Froyland, N. Santitissadeekorn, and A. Monahan, *Transport in time-dependent dynamical systems: Finite-time coherent sets*, *Chaos: An Interdisciplinary Journal of Nonlinear Science* **20** (2010), no. 4 043116.

[163] G. Froyland, *Dynamic isoperimetry and the geometry of lagrangian coherent structures*, *Nonlinearity* **28** (2015), no. 10 3587.

[164] I. Mezic, *On the geometrical and statistical properties of dynamical systems: theory and applications*. PhD thesis, California Institute of Technology, 1994.

[165] I. Mezić and S. Wiggins, *A method for visualization of invariant sets of dynamical systems based on the ergodic partition*, *Chaos: An Interdisciplinary Journal of Nonlinear Science* **9** (1999), no. 1 213–218.

[166] F. Sotiropoulos, D. R. Webster, and T. C. Lackey, *Experiments on lagrangian transport in steady vortex-breakdown bubbles in a confined swirling flow*, *Journal of Fluid Mechanics* **466** (2002) 215–248.

[167] M. Budisić and I. Mezić, *Geometry of the ergodic quotient reveals coherent structures in flows*, *Physica D: Nonlinear Phenomena* **241** (2012), no. 15 1255–1269.

[168] A. C. Poje, G. Haller, and I. Mezić, *The geometry and statistics of mixing in aperiodic flows*, *Physics of Fluids (1994-present)* **11** (1999), no. 10 2963–2968.

[169] A. Fabregat, I. Mezic, and A. C. Poje, *Finite-time partitions for lagrangian structure identification in gulf stream eddy transport*, *arXiv preprint arXiv:1606.07382* (2016).

[170] I. Mezić, S. Loire, V. A. Fonoberov, and P. Hogan, *A new mixing diagnostic and gulf oil spill movement*, *Science* **330** (2010), no. 6003 486–489.

[171] M. Budisić, S. Siegmund, D. T. Son, and I. Mezić, *Mesochronic classification of trajectories in incompressible 3D vector fields over finite times*, *Discrete and Continuous Dynamical Systems - Series S* **9** (Aug., 2016) 923–958.

[172] W. Chien, H. Rising, and J. Ottino, *Laminar mixing and chaotic mixing in several cavity flows*, *Journal of Fluid Mechanics* **170** (1986), no. 1 355–377.

[173] C. Leong and J. Ottino, *Experiments on mixing due to chaotic advection in a cavity*, *Journal of Fluid Mechanics* **209** (1989) 463–499.

[174] F. Ling and G. Schmidt, *Mixing windows in discontinuous cavity flows*, *Physics Letters A* **165** (1992), no. 3 221–230.

[175] F. Ling, *The effect of mixing protocol on mixing in discontinuous cavity flows*, *Physics Letters A* **177** (1993), no. 4-5 331–337.

[176] S. C. Jana, G. Metcalfe, and J. Ottino, *Experimental and computational studies of mixing in complex stokes flows: the vortex mixing flow and multicellular cavity flows*, *Journal of Fluid Mechanics* **269** (1994) 199–246.

[177] V. Meleshko and G. Peters, *Periodic points for two-dimensional stokes flow in a rectangular cavity*, *Physics Letters A* **216** (1996), no. 1 87–96.

[178] P. Anderson, O. Galaktionov, G. Peters, F. Van de Vosse, and H. Meijer, *Analysis of mixing in three-dimensional time-periodic cavity flows*, *Journal of Fluid Mechanics* **386** (1999) 149–166.

[179] P. D. Anderson, O. S. Galaktionov, G. W. Peters, F. N. van de Vosse, and H. E. Meijer, *Chaotic fluid mixing in non-quasi-static time-periodic cavity flows*, *International journal of heat and fluid flow* **21** (2000), no. 2 176–185.

[180] M. A. Stremler and J. Chen, *Generating topological chaos in lid-driven cavity flow*, *Physics of Fluids (1994-present)* **19** (2007), no. 10 103602.

[181] J. G. Franjione, C.-W. Leong, and J. M. Ottino, *Symmetries within chaos: a route to effective mixing*, *Physics of Fluids A: Fluid Dynamics (1989-1993)* **1** (1989), no. 11 1772–1783.

[182] J. Ottino, F. Muzzio, M. Tjahjadi, J. Franjione, S. Jana, and H. Kusch, *Chaos, symmetry, and self-similarity- exploiting order and disorder in mixing processes*, *Science* **257** (1992), no. 5071 754–760.

[183] M. Liu, F. Muzzio, and R. Peskin, *Quantification of mixing in aperiodic chaotic flows*, *Chaos, Solitons & Fractals* **4** (1994), no. 6 869–893.

[184] S. C. Jana, M. Tjahjadi, and J. Ottino, *Chaotic mixing of viscous fluids by periodic changes in geometry: baffled cavity flow*, *AIChE journal* **40** (1994), no. 11 1769–1781.

[185] C. Migeon, A. Texier, and G. Pineau, *Effects of lid-driven cavity shape on the flow establishment phase*, *Journal of Fluids and Structures* **14** (2000), no. 4 469–488.

[186] V. Chakravarthy and J. Ottino, *Mixing of two viscous fluids in a rectangular cavity*, *Chemical engineering science* **51** (1996), no. 14 3613–3622.

[187] R. Chella and J. Viñals, *Mixing of a two-phase fluid by cavity flow*, *Physical Review E* **53** (1996), no. 4 3832.

[188] A. Vikhansky, *Chaotic advection of finite-size bodies in a cavity flow*, *physics of fluids* **15** (2003), no. 7 1830–1836.

[189] W. R. Hwang, P. D. Anderson, and M. A. Hulsen, *Chaotic advection in a cavity flow with rigid particles*, *Physics of fluids* **17** (2005), no. 4 043602.

[190] S. Pai, P. Prakash, and B. Patnaik, *Numerical simulation of chaotic mixing in lid driven cavity: effect of passive plug*, *Engineering Applications of Computational Fluid Mechanics* **7** (2013), no. 3 406–418.

[191] D. Anosov and V. Arnold, *Dynamical System I, Ordinary Differential Equations and Smooth Dynamical Systems*. Springer Verlag, 1994.

[192] G. Mathew, I. Mezić, and L. Petzold, *A multiscale measure for mixing*, *Physica D: Nonlinear Phenomena* **211** (2005), no. 1 23–46.

[193] T. Solomon and I. Mezić, *Uniform resonant chaotic mixing in fluid flows*, *Nature* **425** (2003), no. 6956 376–380.

[194] L. Prandtl, *Uber flussigkeits bewegung bei sehr kleiner reibung*, *Verhaldlg III Int. Math. Kong* (1904) 484–491.

[195] G. K. Batchelor, *On steady laminar flow with closed streamlines at large reynolds number*, *Journal of Fluid Mechanics* **1** (1956), no. 02 177–190.

[196] G. A. Pavliotis and A. Stuart, *Multiscale methods: averaging and homogenization*. Springer Science & Business Media, 2008.

[197] S. Osher and R. Fedkiw, *Level set methods and dynamic implicit surfaces*, .

[198] J.-L. Thiffeault, *Using multiscale norms to quantify mixing and transport*, *Nonlinearity* **25** (2012), no. 2 R1.

[199] V. I. Arnold, *Mathematical methods of classical mechanics*, vol. 60. Springer, 1989.

[200] L. A. Times, *Santa barbara county official rejects plan to move crude oil by truck*, 2015. URL: http://www.latimes.com/local/lanow/la-me-ln-oil-trucks-rejected-20150609-story.html.

[201] S. B. C. A. P. District, *Exxonmobil production company santa ynez unit project*, 2017. URL: https://www.ourair.org/santa-ynez-unit/.

[202] S. B. C. A. P. District, *Fast facts: Refugio state beach oil spill, and response from plains all-american pipelines rerepsentatives*, 2015. URL: http://www.keyt.com/news/santa-barbara-s-county/fast-facts-refugio-state-beach-oil-spill-/65407047.

[203] NOAA-DARRP, *Damage asessment for refugio oil spill*, 2016. URL: https://casedocuments.darrp.noaa.gov/southwest/refugio-beach/admin.html.

[204] P. C. B. Times, *Refugio oil spill cleanup costs near $100 million*, 2015. URL: https://www.pacbiztimes.com/2015/06/27/refugio-oil-spill-cleanup-costs-near-100-million/.

[205] L. A. Times, *Refugio oil spill may have been costlier, bigger than projected*, 2015. URL: http://www.latimes.com/local/lanow/la-me-ln-refugio-oil-spill-projected-company-says-20150805-story.html.

[206] CNN, *Tar balls wash up on california's manhattan beach; officials investigate*, 2015. URL: http://www.cnn.com/2015/05/28/us/california-manhattan-beach-tar-balls/index.html.

[207] L. A. Times, *Santa barbara spill is prime suspect in l.a.-area tar balls*, 2015. URL: http://www.latimes.com/local/california/la-me-tar-balls-20150605-story.html.

[208] D. E. Barrick, J. M. Headrick, R. W. Bogle, and D. Crombie, *Sea backscatter at hf: Interpretation and utilization of the echo*, *Proceedings of the IEEE* **62** (1974), no. 6 673–680.

[209] L. K. Shay, H. C. Graber, D. B. Ross, and R. D. Chapman, *Mesoscale ocean surface current structure detected by high-frequency radar*, *Journal of Atmospheric and Oceanic Technology* **12** (1995), no. 4 881–900.

[210] B. M. Emery, L. Washburn, and J. A. Harlan, *Evaluating radial current measurements from codar high-frequency radars with moored current meters*, *Journal of Atmospheric and Oceanic Technology* **21** (2004), no. 8 1259–1271.

[211] D. G. Luenberger, *Optimization by vector space methods*. John Wiley & Sons, 1997.

[212] L. A. Times, *Oil spill cleanup extends to ventura county*, 2015. URL: http://www.latimes.com/local/lanow/la-me-ln-oil-spill-cleanup-extends-to-ventura-county-20150529-story.html.

[213] NBC, *Tar globs wash ashore on zuma beach*, 2015. URL: https://www.nbclosangeles.com/news/local/Oil-Clumps-Turn-Up-at-Zuma-Beach-in-Malibu-305929081.html.

[214] L. A. Times, *Some tarballs on l.a. county beaches came from santa barbara oil spill*, 2015. URL: http://www.latimes.com/local/lanow/la-me-ln-tarballs-santa-barbara-spill-20150622-story.html.